

Smoothed particle hydrodynamics simulations of
freely moving solid objects in a free-surface flow
with applications to river ice dynamics

Daniel Robb
Department of Civil Engineering and Applied Mechanics
McGill University, Montreal

November 2012

A thesis submitted to McGill University in partial fulfillment of the requirements
for the degree of Master of Engineering

© Daniel Robb 2012

Abstract

River ice jams can cause many problems including extreme flooding, damage to structures, interference with navigation, and restrictions on hydropower operations. Their annual cost to the Canadian economy has been estimated to be nearly one hundred million dollars. This thesis explores the application of smoothed particle hydrodynamics (SPH) to river ice flows. SPH is a meshless method used to solve fluid dynamics problems, whereby the fluid is replaced by a set of particles that move with the flow. This method is particularly well suited to modelling complex free-surfaces and moving solid boundaries. The main contributions of this study were the new developments made to an existing SPH code enabling the accurate simulation of freely moving solid objects in a free-surface flow subject to hydrodynamic and solid contact forces. An SPH Arbitrary Lagrangian-Eulerian (ALE) formalism was used to model the fluid flow and the hydrodynamic forces exerted on solid objects. This study involved coupling the existing SPH-ALE model with the discrete element method (DEM) used to model solid interactions with other solids and with boundaries. The solid interactions were implemented as both a hard-sphere model based on instantaneous, inelastic collisions, and a soft-sphere linear spring and dashpot model based on force-displacement relationships. Application and validation test cases of freely moving solid objects were simulated and compared with analytical solutions, laboratory experiments, and other computational results. These new capabilities were then applied to river ice dynamics problems. The methods used in this study are suited to smaller scale river ice processes where the dynamic effects may not be captured with traditional depth-averaged modelling techniques. Computational results showing the stability of a floating ice block approaching a stationary cover and ice accumulation upstream of an obstruction are encouraging and they show promise to serve as a useful quantitative engineering tool in the future.

Résumé

Les embâcles de glace peuvent causer de nombreux problèmes, y compris des inondations, des dommages aux structures, interférence avec la navigation et des restrictions sur les opérations hydroélectriques. Leur coût annuel pour l'économie canadienne est estimé à presque 100 millions de dollars. Cette thèse étudie l'application de la méthode de simulation numérique, *smoothed particle hydrodynamics* (SPH) pour les problèmes de glace en rivière. SPH est une méthode utilisée pour résoudre les problèmes de dynamique des fluides, dans laquelle le liquide est modélisé par un ensemble de particules. Cette méthode est particulièrement bien adaptée pour modéliser les écoulements à surfaces libres. Les principales contributions de cette étude sont les nouveaux développements apportés à un code SPH existant, permettant la simulation d'objets solides qui sont emportés avec l'écoulement à surface libre. Un formalisme SPH Arbitrary Lagrangian-Eulerian (ALE) a été utilisé pour modéliser l'écoulement du fluide et les forces hydrodynamiques sur les objets solides. Cette étude porte sur le couplage du modèle existant SPH-ALE avec la *discrete element method* (DEM) utilisée pour modéliser les interactions solides entre eux et avec des parois. Les interactions solides ont été implémentées comme un modèle de *hard-sphere*, basé sur les collisions inélastiques instantanées, ainsi qu'un modèle *soft-sphere* basé sur les relations entre les forces et les déplacements. Des cas-test de validation et application ont été simulés et évalués pour vérification avec des solutions analytiques, des expériences de laboratoire, et d'autres résultats de calcul. Ces nouvelles fonctionnalités ont ensuite été appliquées aux problèmes dynamiques de glace en rivière. Les résultats numériques montrent la stabilité d'un bloc de glace flottant qui s'approche un bloc fixe et l'accumulation de glace en amont d'une obstruction. Ces résultats prometteurs permettent de valider cette technique pour l'évaluation quantitative future en ingénierie.

Acknowledgements

I would like to express my sincerest gratitude to my supervisor, Professor Susan Gaskin. It has been an absolute privilege and pleasure to work with her over the past two years. Her advice and encouragement have made this experience all the more enjoyable and enriching. I am very grateful for the support and expertise from two collaborators: Etienne Parkinson of Andritz Hydro (Vevey, Switzerland) and Marc Villeneuve of LaSalle Consulting Group. This research would not have been possible without Jean-Christophe Marongiu of Andritz Hydro. His wealth of knowledge on the SPH method, high performance computing, and computational fluid dynamics was instrumental in this work and my sincerest appreciation goes to him for the generous support and advice that he provided. Many thanks to Martin Rentschler and Magdalena Neuhauser of Andritz Hydro for sharing their expertise on the SPH method, computer programming, and mathematics and thank you to Magdalena for reading and commenting on parts of this thesis. I thank Jean-Philippe Saucet and Wael Taha of LaSalle Consulting Group for the discussions on river ice modelling. Thank you to my fellow graduate students Yulia Akutina, Alejandro Perez, and Claire Murray for their helpful discussions throughout this research. I feel very fortunate to have such a wonderful support network of friends and family, and I thank them for their encouragement. I would especially like to thank my parents and my sister for their love, support, and confidence in me.

Table of Contents

Abstract	i
Acknowledgements	iii
List of Figures	vii
List of Tables	viii
List of Symbols	x
1 Introduction	1
2 Background and literature review	5
2.1 Smoothed particle hydrodynamics	5
2.2 Discrete element method	9
2.2.1 Granular material	9
2.2.2 Discrete element method	11
2.3 Ice Jams	14
2.3.1 Physical description of river ice processes	14
2.3.2 Analytical methods	17
2.3.3 Ice jam mechanics	20
2.3.4 Computer simulations of river ice processes	26
3 Smoothed particle hydrodynamics	30
3.1 Interpolation	32
3.2 Interpolation of derivatives	36
3.3 Kernels	38
3.4 Application to fluid dynamics	39
3.5 Time integration	45
3.6 Boundary Conditions	47
3.7 Artificial viscosity	50
3.8 Riemann solvers	51
3.9 SPH-ALE	58
3.10 Summary	65
4 Discrete element method	66
4.1 Position and rotation of a rigid body	69
4.2 Coordinate systems	69
4.3 Rotation matrices	69
4.4 Moments of inertia	71
4.5 Equations of motion	72
4.6 Hard-sphere model	73
4.7 Soft-sphere model	76
4.8 Summary	81

5	Ice Jams	82
5.1	Floating block stability	82
5.2	Steady state and equilibrium ice jams	85
5.3	Summary	88
6	Application and validation of simulations with freely moving objects	89
6.1	Hard-sphere model	90
6.1.1	Central collision between two solids	90
6.1.2	Solid dropping onto a level surface	92
6.2	Soft-sphere method	94
6.2.1	Collapse of a granular column onto a horizontal plane	94
6.2.2	Granular collapse in two dimensions	96
6.2.3	Granular collapse in three dimensions	99
6.2.4	Granular collapse of dilated circular discs in three dimensions .	100
6.3	SPH simulations with freely moving solid objects	101
6.3.1	Wedge entry	102
6.3.2	Falling solids with different densities	105
6.3.3	Solids driven by a water stream	106
6.4	Summary	109
7	Ice jam simulations	110
7.1	Floating block stability	110
7.2	Dynamic pressure on a partially submerged stationary block	112
7.3	Ice accumulation at an obstruction	117
7.4	Summary	119
8	Conclusions and future work	120
References		124

List of Figures

2.1	Description of different granular flow regimes.	10
2.2	Bead jam initiation in a straight flume	21
2.3	Floating block stability: definition sketch	22
2.4	Floating block stability: modes of submergence	23
2.5	Profile of an ice jam with an equilibrium reach	26
3.1	Kernel support inside the problem domain	35
3.2	Kernel support truncated by the problem domain	35
3.3	Comparison of three different kernel functions for a one-dimensional problem.	39
3.4	The Wendland kernel function for a two-dimensional problem.	39
3.5	Boundary conditions for impermeable surfaces.	49
3.6	Riemann problem between neighbouring particles	55
3.7	Riemann solution structure	55
3.8	An example of a Riemann solution	56
3.9	Possible wave patterns in the solution of the Riemann problem	57
3.10	Lagrangian, Eulerian, and ALE descriptions in one dimension	60
4.1	Coordinate system in the world frame and the body frame.	69
4.2	Soft-sphere model nomenclature.	77
4.3	Soft-sphere model with spring and dashpot system.	77
6.1	Central collision between two solids: numerical setup	91
6.2	Central collision between two solids: computational results	92
6.3	Solid dropping onto a level surface: numerical setup	93
6.4	Solid dropping onto a level surface: computational results	93
6.5	Geometry of the initial column and the final pile in a granular collapse.	95
6.6	Granular collapse in two dimensions: computational results	97
6.7	Granular collapse in two dimensions: vertical and horizontal forces	97
6.8	Granular collapse in three dimensions: computational results	100
6.9	Granular collapse of dilated circular discs in three dimensions: computational results.	101
6.10	Wedge entry: numerical setup.	103
6.11	Wedge entry: computational results.	104
6.12	Wedge entry: vertical force time history.	105
6.13	Falling solids with different densities: numerical setup	106
6.14	Falling solids with different densities: computational results.	107
6.15	Solids driven by a water stream: numerical setup.	107
6.16	Solids driven by a water stream: computational results.	108
7.1	Floating block stability: numerical setup	111
7.2	Floating block stability times series	112

7.3	Floating block stability: comparison of SPH results with theory and experiments	113
7.4	Dynamic pressure on a partially submerged stationary block: numerical setup	113
7.5	Dynamic pressure on a partially submerged stationary block: computational results	116
7.6	Ice accumulation at an obstruction: numerical setup	117
7.7	Ice accumulation at an obstruction: time series	118

List of Tables

3.1	Conditions on the kernel function.	34
4.1	Comparison of hard- and soft-sphere models.	67
6.1	Central collision between two solids	91
6.2	Granular collapse: comparison of scaling laws	95
6.3	Granular collapse in two dimensions: simulation parameters	96
6.4	Granular collapse in two dimensions: comparison with theory	98
6.5	Granular collapse in three dimensions: simulation parameters	99
6.6	Granular collapse of dilated circular discs in three dimensions : simulation parameters	101
7.1	Floating block stability: simulation parameters	111
7.2	Dynamic pressure on a partially submerged stationary block: simulation parameters	114
7.3	Ice accumulation at an obstruction: simulation parameters	117

List of Symbols

Scalar quantities (Roman symbols):

a	Aspect ratio of the initial height to the initial radius of a granular column ($= \frac{h_0}{r_0}$)
B	Channel width
b	Width of a floating block
c_0	Speed of sound
D	Kernel support (region over which the interpolation occurs)
F_D	Densimetric Froude number
Fr	Froude number
g	Gravitational acceleration
h	Smoothing length
h_t	Distance from the centre of the kernel to the edge of its support
$h_{0,\infty}$	Initial height (0) and the height of the final deposit of a granular column (∞)
j	Magnitude of impulse
k	Spring stiffness
$k_{0,1,2}$	Coefficient of lateral thrust (0), friction (1), and passive earth pressure (2)
L	Length of floating block
m	Mass
Ma	Mach number
P	Pressure
$r_{0,\infty}$	Initial radius (0) and final run-out distance of a granular column (∞)
Re	Reynolds number
T	Streamwise force per unit width of channel
t	Time
t_i	Thickness of floating block or ice cover
t_s	Thickness of solid below the free-surface (submerged)
V	Upstream depth-averaged water velocity in the streamwise direction
W	Kernel function
S	Channel slope

Scalar quantities (Greek symbols):

δt	Time-step
Δx	Discretization size
δ	Overlap between two solids
ϵ	Coefficient of restitution
η	Damping coefficient
λ	Eigenvalue
μ	Dynamic viscosity
μ_f	Coefficient of friction
ν	Kinematic viscosity
Ω	Problem domain
ω	Particle weight (units of volume in three dimensions and area in two dimensions)
$\partial\Omega$	Problem domain boundary

ϕ	Internal angle of friction
ρ	Density (ρ_0 is a reference density and ρ_s is a solid density)
σ_x	Stress on the ice jam in the streamwise direction
τ	Shear
ζ	Bulk viscosity

Vector and tensor quantities:

ω	Angular velocity
Φ	Vector of conserved quantities $(\phi_1, \phi_2, \dots, \phi_n)^T$
τ	Torque
θ	Vector with components $(\gamma, \beta, \alpha)^T$ representing angles rotated about the x, y, and z axis
L	Angular momentum
P	Linear momentum
v	Linear velocity of a rigid body's centre of mass
f_e	Net external body force per unit mass
F	Force
I	Inertia tensor
J	Impulse
n, t	Unit vectors pointing normal (n) and tangent (t) to a surface
p	Position vector on the surface of a rigid body
R	Rotation matrix
u	Velocity vector with components $(u, v, w)^T$
x	Position vector

Superscripts:

*	Solution to the Riemann problem
-,+	Pre (-) and post (+) collision values
.	Time derivative
∂	Value of a quantity on a boundary element
T	Transpose of a vector

Subscripts:

a, b	Value at the particle of interest (a) and at a particle in its neighbourhood (b)
i, j, k	Coordinates of the cartesian coordinate system. The Einstein summation convention is adopted for repeated cartesian indices.
i, w	Quantities related to ice (i) and water (w)
L, R	Left and right states of a Riemann problem
n, t	Normal (n) and tangential (t) directions
u	Under the floating block or ice jam

Notes:

- The symbols most frequently used in the text are given above.
- Any other notation will be defined the first time it is introduced.
- Vector and tensor quantities are written in bold typeface.

Chapter 1

Introduction

River ice jams can cause problems including extreme flooding, damage to structures, interference with navigation, and restrictions on hydropower operations. As a result, ice jams are responsible for major social, economic, and ecological impacts. The most common concern with ice jams is flooding. In contrast to open water floods, which can often be predicted days or weeks in advance, ice jam flooding is abrupt, leaving little time for evacuation of nearby residents or protection of property. Their annual cost to the Canadian economy has been estimated to be nearly one hundred million dollars. Just as important are the ecological impacts of river ice on the surrounding ecosystem. The behaviour of migratory fish is known to be closely linked to the timing of freeze-up and breakup. Also, bank erosion from ice jams can cause large suspended sediment discharges that can threaten certain fish species and their spawning grounds. The ecological effects of ice jamming are not always negative; the subsequent flooding in the spring corresponds to the highest rates of nutrient fluxes that serve to replenish nutrient-poor areas downstream. Despite the major social, economic, and ecological impacts that Canada and other high-latitude regions face, many river ice processes are poorly understood.

River ice flows depend on complex relationships between hydrodynamic, mechanical, and thermal processes. Current mathematical models incorporate concepts native to fluid mechanics, soil mechanics, solid mechanics, rheology, thermodynamics, and meteorology. Depending on the length and time scales of the problem of interest, one can simplify the complex interactions between various processes. For example, given a relatively small river reach over a short period of time, thermal effects may play an insignificant role in the river ice behaviour over the area of interest. Through various conscientious simplifications, mathematical models can be developed that describe specific river ice processes.

River flows belong to a broader category of flows called free-surface flows. Dam breaks, wave run-up, tidal bores, sloshing in fuel tanks, and tsunamis are all examples of free-surface flows. An important feature of this type of flow is that the fluid is unbounded in space. That is, the location of the fluid boundary along the free-surface is an unknown in the problem to be solved. This feature presents a significant challenge to those seeking analytical or numerical solutions to free-surface flow problems. Given their prevalence in nature and industry, methods to accurately model free-surface flows are of great socioeconomic and environmental interest.

The Navier-Stokes equations describe the motion of a fluid. They consist of equations for conservation of mass, momentum, and energy. They have no general analytical solution; therefore, approximations are commonly made through scale analysis for a specific application. Even after making simplifying assumptions, the resulting approximate equations are often too complicated to solve analytically. In this case, many scientists and engineers seek numerical solutions using computers.

Due to the complexity of many physical problems, scale models are constructed in laboratories to run controlled experiments to analyze the given physical system. Laboratory experiments, however, are expensive and have interpretation problems such as scale effects, for example, scaling quantities such as viscosity or surface tension. The rapid increase in computational power in recent years has made computer simulations an attractive option for helping solve many engineering problems. The scale and complexity of some problems can make them impractical or prohibitively expensive to model in the laboratory. A computer simulation could potentially serve as an alternative. A more rigorous approach would be to use computer simulations in conjunction with laboratory experiments. In the context of engineering design, computer simulations can be very useful in the early stages to help establish key dimensions and other important parameters. These early iterations in the design process can potentially result in considerable savings later on.

Traditionally, most numerical methods, such as finite difference or finite element methods, discretize the given problem in space onto a computational grid made up of interconnected calculation points. The values of the parameters of interest, such as velocity and pressure, are calculated at each grid point. These calculations are carried out at specific time intervals so that the original governing equations are discretized both spatially and temporally. In this manner, a set of partial differential equations containing both space and time derivatives is reduced to a set of algebraic equations that can be easily solved at discrete points in space and time. Methods such as these are called grid-based methods.

There are two descriptions that are widely used to observe and analyze fluid flow. The first is the Eulerian representation, in which fluid properties are observed at fixed positions. The second is the Lagrangian representation, in which fluid properties are observed following trajectories of specific fluid parcels. Grid-based methods can be cast in either an Eulerian or a Lagrangian representation. In an Eulerian representation, the calculation points do not move relative to the fluid and the computational grid is fixed in space. In a Lagrangian representation, the calculation points move with the fluid and the computational grid changes shape accordingly.

Grid-based methods have enjoyed much success in recent years. They are used in most commercial software packages and serve as a standard tool in both research and industry to solve a myriad of computational fluid dynamics problems as well as problems in other fields. Grid-based methods, however, are not without shortcomings. If the grid is fixed in space relative to the fluid in an Eulerian way, it is challenging and computationally demanding to accurately track free-surfaces and moving boundaries. If the grid moves with the fluid in a Lagrangian manner, large deformations require computationally expensive re-meshing techniques; otherwise, the mesh can become entangled leading to numerical error.

Meshless methods offer an alternative approach to grid-based techniques and they are particularly well suited to model free-surface flow problems. As the name implies, the calculation points in a meshless method have no prescribed connectivity. This makes it easier to model large deformations without having to use complicated and time consuming re-meshing strategies. One particular meshless method of interest is called smoothed particle hydrodynamics (SPH). In this method, the fluid is replaced by a set of particles that moves with the flow. Consequently, free-surfaces and moving boundaries are automatically tracked by the SPH particles without special treatments.

This thesis explores the application of SPH to river ice flows. The overall goal is to model a free-surface river or channel flow containing discrete solids representing ice fragments. This approach has the potential to shed light on many dynamic ice processes including jam initiation, jam release, ice runs, pile-up, and under-turning. The fluid is composed of SPH particles and the ice fragments are freely moving solid bodies that move according to the hydraulic forces from the fluid and any contact forces exerted on them from other ice fragments or obstructions.

To work towards this goal, part of the present study is to make new developments to an existing SPH code originally used to model flow through a Pelton turbine. This existing numerical model has had success simulating the dynamic free-surface flows and complex geometries characteristic of the turbomachinery industry (Marongiu et al., 2010). The novel boundary treatment in this model has allowed the accurate calculation of hydraulic forces on solid boundaries and the specific type of SPH method used, called SPH-ALE (Arbitrary Lagrangian-Eulerian), is particularly suited to model flows containing moving solid boundaries. Admittedly, turbomachinery and river ice flows are not very similar. However, the capability to accurately treat moving solid boundaries and complex geometries in a free-surface flow is something that could be highly desired in a river ice model.

In terms of new developments to the numerical model, there are two main goals.

The first is to enable the accurate simulation of freely moving solid objects subject to hydraulic forces and gravity. Prior to the new developments, the motion of a solid object had to be prescribed by the user before commencing a simulation. The second goal is to implement the accurate simulation of collisions and contact forces between freely moving solids in a free-surface flow. Two different discrete element approaches are taken. The first allows instantaneous collisions between arbitrarily shaped objects and is suitable for low concentrations of solids that do not stay in contact for extended periods. The second is more suitable for solids at high concentrations where they stay in contact for extended durations and develop contact force networks between large groups of solids. The second approach can accommodate solids shaped as spheres and three-dimensional circular discs of finite thickness.

The remainder of this thesis is structured in the following way. Chapter 2 introduces the numerical methods used in this thesis to model river ice flows. Also, a qualitative description of river ice processes is provided along with an overview of analytic methods used to describe these processes. Finally, various existing river ice models are described. Chapters 3, 4, and 5 present the theory and mathematical framework related to the topics introduced in chapter 2. Chapter 3 describes the SPH method with a focus on the specific formulation used to calculate the numerical results in this thesis. Chapter 4 describes the two different discrete element approaches used in this work: the hard-sphere model and the soft-sphere model. Chapter 5 reviews theory used for analyzing river ice processes with a focus on the processes that are simulated as part of this thesis. Chapter 6 presents application and validation test cases related to freely moving solid objects. Chapter 7 presents simulation results specific to ice jam processes. Finally, chapter 8 provides some concluding remarks, summarizes the main contributions, and proposes some future extensions of this work.

Chapter 2

Background and literature review

2.1 Smoothed particle hydrodynamics

Smoothed particle hydrodynamics (SPH) is a numerical method for solving fluid dynamics problems, whereby the fluid is replaced by a set of particles. Each particle is assigned a mass and moves with the fluid velocity. A particle can be thought of as a fluid parcel having the same volume of fluid over time, or equivalently as an interpolation point over which fluid variables, such as velocity, density, and pressure, are calculated. The fluid variables associated with a particle move with it and change with time according to the equations governing the fluid dynamics problem, i.e. continuity and momentum. These fluid variables are interpolated over the values at neighbouring particles using a kernel function.

SPH is a Lagrangian method, since the evolution of the system is described by fluid parcels that move with the flow. As a Lagrangian method, SPH has several advantages over Eulerian methods, where the evolution of the system is monitored from fixed points in space. In SPH, advection is exact, since the particles, which can be thought of as fluid parcels, carry their properties with them. Conversely, Eulerian methods can suffer from numerical error caused by the non-linear effects of advecting fluid properties between fixed points. Another advantage is that SPH can easily model problems with more than one material by assigning a different set of particles to each one. The particle motion automatically defines the interface between each material. Eulerian descriptions have trouble accurately tracking material interfaces because the calculation points are fixed in space and the true material interface could be located somewhere in between two calculation points.

While grid-based methods have calculation points joined on a computational grid, SPH is a meshless method, since its particles have no specified connectivity. Without a mesh to generate, the pre-processing time is reduced and complicated re-meshing techniques to avoid mesh entanglement are no longer needed. Consequently, SPH can accommodate large deformations more easily than a Lagrangian grid-based method. Complex geometries, moving geometries, brittle fracture, and fragmentation are all areas where meshless methods, such as SPH, are often preferred.

The advantages that the Lagrangian, meshless nature of SPH provide do not come without a cost. Since there is no connectivity between SPH particles, they may become disordered, or in other words, irregularly spaced, which reduces the simulation accu-

racy. It is difficult to quantify this inaccuracy since the particle arrangement is case specific. For example, in a highly dynamic simulation, the particles may become quite disordered; whereas, in static equilibrium, the particle arrangement could approach a regular lattice. In all cases, the governing equations tend to move the particles in a roughly evenly spaced manner. Therefore, an error estimate based on equally spaced particles under predicts the true error and an estimate based on randomly distributed particles results in an over prediction.

Accurate boundary conditions are difficult to implement in SPH. Recall that the fluid variables associated with a particle are calculated by interpolating over neighbouring particles. If an SPH particle is near a solid boundary on the limit of the problem domain, there will be no neighbouring particles on the other side of this boundary. The interpolation will then be over fewer particles than if it were surrounded entirely by fluid. The interpolation will also occur over a region that is not symmetric about the particle whose fluid variables are being calculated. For these reasons, a special treatment is taken for calculations near solid boundaries. In the early developments of SPH, boundary treatments were ignored since the method was applied to problems without solid boundaries. Later on, several methods were proposed to address this shortcoming. These are discussed further in section 3.6. Although solid boundaries pose a challenge in SPH, free-surfaces are described approximately in a correct manner without any special boundary treatment. This is why SPH is often said to have a natural description of free-surfaces.

First published by Lucy (1977); Gingold and Monaghan (1977), SPH emerged from the astrophysics community, where it was used to study cosmological structure formations (Hernquist and Katz, 1989), binary stars (Gingold and Monaghan, 1978), and planetary collisions (Benz et al., 1986). Further astrophysical applications are described in Monaghan (1992) and more recent advances in Springel (2010). SPH became a popular tool in modelling astrophysical phenomena because it is easy to model free boundaries, to model clumping of matter, and to treat physics such as relativistic dynamics and magnetic fields. Since its conception in the late nineteen-seventies, SPH has branched out into terrestrial applications involving both fluid and solid mechanics.

Monaghan (1994) was the first to show that the success of SPH could be extended from astrophysical problems, based largely on gas dynamics, to simulations of incompressible fluids. The approach was based on the observation that fluids such as water are slightly compressible with a speed of sound generally much larger than the bulk fluid velocity. In this approach, the fluid is treated as slightly compressible with an

equation of state relating changes in pressure to small changes in density. This approach, called the quasi-compressible, or weakly compressible, formulation of SPH (WCSPH), is the most widely used to model incompressible fluids. Monaghan (1994) successfully modelled a dam break, the formation of a bore, and a waves propagating on an inclined slope. These simulations have since served as benchmarks for free-surface simulations using SPH. The SPH European Interest Committee (SPHERIC) provides additional validation tests on their website.

Also using weakly compressible SPH, Morris et al. (1997) accurately simulated low Reynolds number incompressible flows and compared the results to solutions of Poiseuille and Couette flow. Their results of flow past a cylinder also showed good agreement with finite element solutions. Morris et al. (1997) proposed a new method for implementing no-slip boundaries and also an alternative expression for molecular viscosity. Comparisons with Poiseuille and Couette flow are significant since they are two of relatively few exact solutions to the Navier-Stokes equations. The boundary treatment developed by Morris et al. (1997) is still used in many SPH codes.

Although most SPH codes use the weakly compressible formulation, there are some that treat the fluid as truly incompressible. Instead of solving for the pressure with an equation of state, truly incompressible schemes impose zero velocity divergence (Cummins and Rudman, 1999), zero change in density (Shao and Lo, 2003), or both (Hu and Adams, 2007). The pressure is then determined by solving the pressure Poisson equation. Truly incompressible SPH can reduce unphysical pressure fluctuations that can be observed in the weakly compressible formulation.

Its Lagrangian, meshless description makes SPH well suited for simulating complex free-surfaces and multiphase flows. One area where these are common is in marine and coastal zones. Breaking waves on a sloping beach (Dalrymple and Rogers, 2006), overtopping of a seawall (Shao et al., 2006), and caisson breakwater movement (Rogers et al., 2010) are all examples where SPH has had success modelling complex free-surfaces. Some examples of mutiphase flow include air entrainment in fluid-structure impact (Colagrossi and Landrini, 2003), oil containment by a boom (Violeau et al., 2007a), and gravity currents flowing into a stratified fluid (Monaghan et al., 1999). SPH has also been used to model hydraulic engineering and open-channel flows including fishways (Violeau et al., 2007b), sharp-crested weirs (Ferrari, 2010), and hydraulic jumps (Lopez et al., 2010).

Another area where SPH excels is in modelling deformation and fracture of solids. Libersky and Petschek (1991) extended the SPH formulation to include the full stress tensor. This advancement enabled SPH to be applied to problems where material

strength is important, which opened up the method to solid mechanics. Now, several commercial codes including Dyna3D and Autodyn have SPH packages for simulating impact fracture in solids (Monaghan, 2005). The pioneering work by Libersky and Petschek (1991) revealed one of the main shortcomings of SPH known as tensile instability, which causes clustering of SPH particles. Swegle et al. (1995) conducted the first comprehensive study on tensile instability. To correct for this problem, Randles and Libersky (1996) proposed adding dissipation terms, and Monaghan (2000) suggested adding anti-clumping forces between particles.

Problems with a wide range of length and time scales are difficult to model, especially using only one method. Several hybrid techniques have been developed to overcome this challenge. Narayanaswamy et al. (2010) used a coupled Boussinesq-SPH method to model far afield areas applying the Boussinesq approximation, and SPH to capture near shore features such as wave breaking. Similarly, Hilton and Cleary (2012) coupled the shallow water equations with SPH to simulate extreme geo-physical flows. These hybrid methods enable modelling larger areas without having prohibitively long computation times.

With the advancement of high performance computing, larger and more realistic simulations are becoming possible. In the past, complicated industrial flows often proved too computationally heavy; now simulating these applications is more feasible. For example, die-casting, extruding, and slurry flow have all been simulated with SPH. Cleary et al. (2007) provides a comprehensive review on simulating industrial flows with SPH.

SPH has also gained popularity in disciplines outside the scientific community. The film, television, and gaming industries have all profited from the SPH method. Oscar winning Next Limit Technologies shows both scientific and special-effects applications on their website. SPH has been used in such films as Superman Returns, Ice Age, and Lord of the Rings.

Two books have been published on SPH: first Liu and Liu (2003), and more recently, Violeau (2012). Early review articles include Benz (1990) and Monaghan (1992). More recent developments are presented in reviews by Monaghan (2005), Monaghan (2012), and Liu and Liu (2010). This section described the basic concepts, history, advantages and disadvantages, and some applications of the SPH method. The following section gives some background on the discrete element method which is used in this thesis to model freely moving solid objects including ice fragments. The last section provides information pertaining to ice jam processes and numerical models specific to ice jams, including ones using SPH. The following chapter outlines the theory of the SPH method

and presents the approach used to calculate the results presented in this thesis.

2.2 Discrete element method

The discrete element method (DEM) is a numerical technique for solving problems involving granular material. In this thesis, the DEM is used to simulate solid objects subject to collision and contact forces between other solids. For simulations involving a fluid phase, these solids are also subject to hydraulic forces determined following the SPH techniques introduced in section 2.1 and described in detail in chapter 3. Chapter 6 shows results of DEM simulations involving solids only, as well as ones with both solid and fluid phases, in which the fluid is modelled with SPH. These simulations are mainly validation test cases. Chapter 7 shows results of simulations specific to river ice flows. In many circumstances, river ice is modelled as a granular material (Beltaos, 1995). Before considering numerical methods to model granular material, it is worthwhile to review some of the physics behind granular material and granular flow. This section contains two parts: first, theory and concepts about granular material and granular flow are presented; and second, the DEM is introduced as a numerical method for modelling granular material.

2.2.1 Granular material

A granular material is a collection of a large number of discrete particles in contact or near contact with each other. The voids between the particles are generally filled with a fluid such as air or water. Granular material belongs to a broader class of two-phase systems. If the solids are closely packed or much denser than the interstitial fluid, it is the solid fraction alone that dominates the flow behaviour within the granular material. In this case, the granular flow is characterized by frequent collisions between particles, influenced by inter-particle forces, and friction. For solids that are spaced far apart, it is the fluid phase that plays the dominant role in the dynamics of the system. This two-phase system is considered a dilute suspension rather than a granular material. The focus of this section is on granular material and dilute suspensions are described further in Batchelor (1974). Depending on the stress conditions, a granular material may behave like a fluid or a solid. For example, the continuous discharge of sand down an inclined chute flows much the same way as a fluid. On the other hand, sand can form piles with sloped surfaces and support externally applied stresses in ways that a fluid cannot. This *dual identity* (Barker, 1994) has peaked the interest of many researchers. It also presents a challenge for developing unified theoretical models as well as computer simulations of granular flow.

Some examples of granular materials are sand, marbles, rice, pharmaceutical pills,

animal feed, coal, granular snow, and pack ice. Granular flows appear in many industrial applications such as slurry pipelines, fluidized beds, hoppers, and tailings piles. They also appear in many geophysical flows including mudslides, debris flows, dispersion of sand dunes, rock falls, drift of pack ice, and ice jams. Their ubiquity in nature and society is a key driving force behind their research.

Granular flows can be classified into flow regimes, each having distinct characteristics. Here, we will divide them into three broad categories: static, quasi-static, and grain-inertia. In the static regime, there is no strain rate and the granular material can support external loads because of the frictional bonds between the particles. If the strain rate is gradually increased, and enough frictional bonds are broken, the granular structure will fail and begin to flow. The particles will start to move in groups, undergoing sliding and rolling contact with each other. If the motion is slow enough, the particles will stay in contact with each other for extended periods during the bulk deformation of the material. This is the quasi-static regime, where stresses are transmitted through a network of contact forces and the effects of inertia are negligible. A further increase in strain rate causes the particle groups to break so that each particle moves freely and independently of its neighbours. This is the grain-inertia regime, where nearly instantaneous inelastic collisions between particles dominate the motion of the granular material, during which momentum is exchanged and energy is dissipated due to the inelasticity of the particles.

Between the quasi-static and the grain-inertia regime, there exists a transitional zone that is worth describing since the stresses in the respective regimes are generated by different mechanisms. It is instructive to consider a rapid granular flow where the shear rate is gradually decreased while the particle concentration is increased. Suppose it is a Couette flow that is generated between two parallel plates, the upper plate moving relative to the lower plate as shown in figure 2.1.

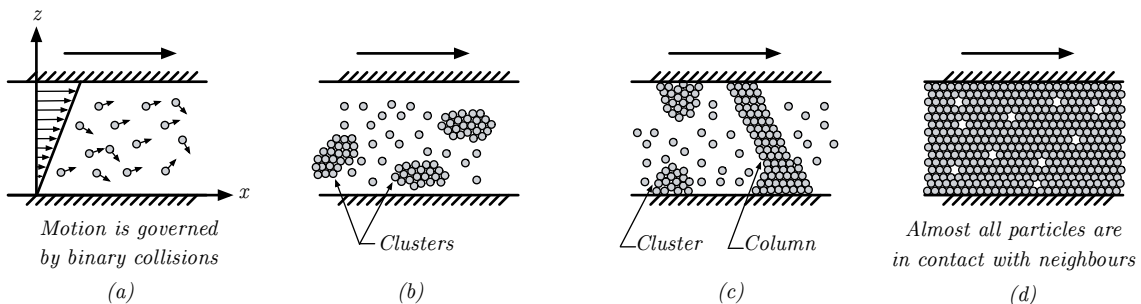


Figure 2.1 – Description of granular flow in (a) the rapidly flowing (grain-inertia), (b) and (c) the transitional, and (d) the quasi-static regimes for increasing solids fraction and decreasing shear rate from (a) to (d). Adapted from Sayed (1981).

Initially, the granular flow is in the grain-inertia regime where binary inelastic collisions between particles govern the motion. As the concentration increases, clusters of particles form where the particles are in rubbing contact. With a further increase in concentration, the clusters grow to span the width of the flow, forming columns between the two walls. These columns are isolated force networks of particles in contact with each other for extended durations. Since the force networks are isolated, there are elements of both grain-inertia and quasi-static granular flow. If the concentration is increased further still, each particle will be in contact with its neighbours, forming an extensive force network spanning the whole flow region. For a low enough shear rate, the inertia becomes negligible and the flow is in the quasi-static regime.

There are several applications where a granular material behaves both like a solid and a fluid. A typical example is flow of sand through a funnel. In the central core, the sand is rapidly flowing and against the funnel walls, the sand is static. In between the two, there exists some transition where the granular material changes its behaviour from a fluid to a solid. In this transition, the granular flow must change from rapidly flowing in the grain-inertia regime, to static, passing through the quasi-static regime.

Although a granular material is a large set of discrete particles, it is sometimes preferred to treat it as a continuum. Provided that the characteristic length scale of the flow is much larger than the mean free path of the particles, the granular material can be treated as a continuum. In this case, the equations of motion can be derived in much the same way as the Navier-Stokes equations. In fact, at a first glance, they have nearly identical forms. The fundamental difference is in the constitutive relationships defining how the stress is generated.

From the discussion in this section, we can identify two dynamic regimes for granular flow in terms of concentration and shear rate: (1) grain-inertia – for low concentration and high shear rate, particles move independently and the motion is governed by frequent nearly instantaneous inelastic collisions between particles; and (2) quasi-static – for high concentration and low shear rate, particles form force networks and endure lasting contacts between each other. In the next section, two types of computer simulations of granular material are presented. Their formulations show similarities to regime (1) and (2).

2.2.2 Discrete element method

The discrete element method (DEM) is a numerical technique for solving granular material problems, whereby the trajectories of each particle are calculated from the collisions and contacts with neighbouring particles. Computer simulations of this kind are important because literally everything is known about each particle at a given

time. For physical experiments with small and many particles, such measurements are nearly impossible.

The DEM can be divided into two types: hard-sphere and soft-sphere models. Hard-sphere models assume that the particles have infinite elastic moduli, so that particle collisions are instantaneous and that no penetration is considered. Soft-sphere models assume finite elastic properties so that collisions occur over finite durations and penetration is allowed at particle contacts.

For hard-sphere models, the motion of each particle can be described as piece-wise linear trajectories between instantaneous particle collisions. The governing equations take on the form of momentum exchanges, where the particle contact force is often not explicitly considered. In many cases, friction and tangential forces are ignored. When particles collide, energy is dissipated by plastic deformation and heat. The amount of energy dissipation, for a given flow, depends on the particle properties. For hard-sphere models, the particle properties are often described using a coefficient of restitution, which specifies the ratio of recoil velocity to approach velocity of colliding particles and thus quantifies the dissipation of energy in a collision.

The applications suited to hard-sphere models are those where the motion is dominated by particle collisions. This is the case in rapid granular flow, where particles follow complicated trajectories composed of inelastic collisions with other particles, characterized by low concentration and high strain rates. These flows are in the grain-inertia regime, described in more detail earlier in this section. In general, hard-sphere models are simpler and computationally faster than soft-sphere models. At high concentrations, however, particles tend to clump together and stay in contact for extended durations. Since the hard-sphere model is based on instantaneous collisions, it is no longer valid. Therefore, at higher concentrations and lower strain rates, granular flow is generally simulated using soft-sphere models.

The main idea behind the soft-sphere approach is to solve the contact force relationships governing the dynamic equilibrium between colliding or contacting particles over finite durations. This is different from the hard-sphere model that evaluates the momentum exchange or impulse between instantaneous collisions of particles. The term *soft*-sphere is misleading, since no deformation in particle shape is calculated. Particles are, however, allowed to overlap at their contact point. The normal component of the inter-particle force is calculated based on this overlap. The friction or tangential forces are calculated from the cumulative relative displacement at the contact points of the particles. Unlike hard-sphere models that only consider one collision per particle-pair at a time, the soft-sphere approach can treat multiple contacts on a

single particle, which is often the case in the quasi-static or static regimes.

The most commonly used soft-sphere model is the distinct element method first published by Cundall and Strack (1979). Its popularity has made the terms discrete element method and distinct element method essentially interchangeable. Technically, the distinct element method falls into a broader group of discrete element methods described in this section. The distinct element method calculates the inter-particle forces based on the overlap between particles in contact. For a given flow or particle arrangement, the amount of overlap between particles is a function of their material properties, which are often described in terms of stiffness and internal angle of friction. Given the material properties, a compatibility equation can be formulated relating the overlap of particles to contact forces through relationships such as Hooke's law or Hertzian contact stresses (O'Sullivan, 2011).

In the interest of computational efficiency, hard-sphere models are preferred since the instantaneous collisions take place over a single time-step. In soft-sphere models, the contact force relationships must be evaluated over 40 to 50 time-steps to produce accurate results (Walton, 1993). This requirement can make the time-step for soft-sphere models prohibitively small.

Most DEM simulations idealize the particle shape as a perfect sphere in three dimensions or a circular disc in two dimensions, which greatly simplifies the analysis. Contacts can be easily detected since particles are necessarily touching if their centres of mass are closer than the sum of their radii. For non-spherical particles, the contact detection is more complicated because their orientation changes as they move. For many particles such as sand, it is often valid to approximate the particle shape as a perfect sphere (Campbell, 1990). Particles with high aspect ratios, such as rice, pharmaceutical pills, or ice floes may have preferential orientations in a flow, which cannot be represented using spheres. More recent DEM simulations have used two-dimensional ellipses (Ting et al., 1993), three-dimensional ellipsoids (Ng and Lin, 1995), three-dimensional dilated circular discs (Hopkins et al., 1996), and assemblies of several spheres (Walton, 1993) to simulate granular flows of particles with non-spherical shapes.

For an arbitrarily shaped solid, it is not only the contact detection that is challenging, but also the lasting contact interaction and the calculation of overlap. The latter two are avoided by using a hard-sphere model. The hard-sphere model can be extended to treat arbitrarily shaped objects by considering solid collisions with instantaneous exchanges of momentum and applying the principles of rigid body dynamics. For consistency, the method will be called hard-sphere throughout the thesis even for

arbitrarily shaped solids.

Review articles on the mechanics of granular flow include Savage (1984), Campbell (1990), and Goldhirsch (2003). Early reviews on computer simulations of granular flow include Campbell (1990), Walton (1993), and Barker (1994). More recent developments are outlined in Bicanic (2004), Van der Hoef et al. (2006), and O’Sullivan (2011).

In the next section, the background on ice jams is presented. Similarities are drawn between granular flows and many ice jam phenomena. It will also be shown that both hard- and soft-sphere models may prove useful for computer simulations of ice jam processes.

2.3 Ice Jams

An ice jam is a stationary accumulation of fragmented ice that restricts the flow in a river or channel. Jams can extend many kilometres long and reach several metres thick. The underside of an ice jam increases the hydraulic resistance of the affected river reach and causes the river to rise. The increase in water level can result in flooding, even for discharges that are well under that required for an open-water flood (Beltaos, 1995).

2.3.1 Physical description of river ice processes

Ice jams occur at both freeze-up and breakup, marking the beginning and end of the ice cover season. Freeze-up generally takes place near the beginning of winter when cold weather decreases the river temperature to produce slush and ice pans. Breakup occurs in the spring when warm weather and increased runoff result in the fracture of the winter ice cover. In more temperate climates, ice jams can also develop in mid-winter during stints of warmer weather called mid-winter thaws.

River ice processes depend on complex relationships between hydrodynamic, mechanical, and thermal processes. While calm water and stratification can promote ice growth at the water surface in a similar way to lakes, ice formation in rivers is strongly influenced by turbulent flow (Beltaos, 1995). Velocities and turbulent intensities in a river vary both in the streamwise direction between pools and rapids and the lateral direction, where velocities are lowest near the banks and highest in the deepest section of the river.

As the temperature drops at the beginning of winter, the ambient air cools the river surface to the freezing point. With further heat loss, supercooling occurs and ice crystals form. The first ice usually appears near the riverbanks, where the velocity and turbulence intensity is low. Depending on the flow conditions, this so-called border

ice can grow from the banks some distance toward the centreline of the river. The extent of the growth depends largely on the flow characteristics, with low turbulence intensity favouring border ice growth. Border ice reduces the surface width of the river; therefore, its growth can greatly influence the initiation of a freeze-up jam caused by bridging or arching of ice floes across the surface width.

At low velocities and low surface turbulence, ice sheets can grow without attachment to the riverbanks. This type of ice formation, commonly known as skim ice, has been observed with lateral dimensions of several hundred metres to over one kilometre upstream of the Lachine Rapids on the St. Lawrence River (Marcotte, 1984). After these large sheets of skim ice are blocked, they can rapidly form a complete ice cover spanning the whole river width.

Away from the banks, where velocity and turbulent intensity is higher, the river can be well mixed in the vertical direction, eliminating temperature stratification. In this case, it is not possible for the ambient air to cool a thin layer of water at the surface to freezing because the surface water is continually mixed with water at depth. As the water is cooled to slightly below 0°C , small ice particles start to appear. These particles are commonly known as frazil. Their formation in a river promotes the growth of ice crystals and further production of frazil. Frazil particles can agglomerate to form larger floes. As the floes grow in size, their buoyancy increases and can overcome the vertical mixing to form a layer of ice or slush on the river's free-surface. In turn, this surface ice can grow in size from accumulation of frazil ice from suspension. It can also accumulate along the existing border ice and add to its lateral growth.

As more and more ice forms on the river surface, the downstream transport can lead to bridging or arching of surface ice across the entire river width. Some river conditions allow border ice to grow across the entire river width before bridging can occur. In both cases, the incoming frazil from upstream can approach the leading edge of an ice cover spanning the entire channel width. Depending mainly on ice thickness, flow depth, and river velocity, the incoming ice will either accumulate at the leading edge of the stationary ice cover or pass underneath it being entrained by the flow. Once an ice cover is initiated, it may propagate upstream from the accumulation of incoming ice. This evolution of the ice cover depends on the flow, channel conditions, and internal strength of the approaching ice.

On slow moving rivers, ice can accumulate upstream of a jam in a single layer and form a thin, loose cover that eventually solidifies from the freezing of the interstitial surface water. This type of single layer jam is commonly known as a surface jam. They generally form at freeze-up and pose little risk of potential damage.

When incoming ice floes submerge at the leading edge of an ice cover, but are not transported a significant distance downstream, the jam thickens. Its thickness is governed by the hydraulic conditions at the leading edge. The cover will attain a certain thickness and as more ice approaches, the jam will advance in the upstream direction. The driving forces applied to the jam in the streamwise direction consist mainly of the flow shear on the underside of the ice cover and the downslope component of the jam's weight. Bank resistance and the internal strength of the ice accumulation oppose these applied forces. As the jam lengthens, the increased applied forces from the cover's weight and flow shear can exceed the opposing forces causing the jam to collapse. This process is called shoving and is followed by a thickening of the ice cover to increase the jam's strength. A jam of this type is called a thickened jam. For an ice jam of a given length, the applied forces due to flow shear and weight depend on the river width. The resisting forces of internal strength and bank resistance depend on jam thickness and do not vary with river width. If all other parameters are equal, a jam in a wide river is more likely to shove than one in a narrow river. This concept is the basis of the early pioneering work by Pariset et al. (1966), describing jams formed by internal collapse (wide-channel jams) or by hydraulic processes (narrow-channel jams), discussed later in this section.

At the beginning of spring or during a mid-winter warm spell, the ice cover begins to decay. There are two main processes responsible for the decay of the ice cover and subsequent breakup. First, the snowmelt runoff increases the discharge, velocity, and water levels in the river. Second, the heat exchanges, primarily from solar radiation, result in melt of the ice cover, decreasing its thickness and mechanical strength (Beltaos, 1995). The combination of the two processes dictates how the breakup takes place.

Breakup conditions can be divided into two types: overmature, and premature breakups. Overmature breakups are dominated by thermal exchanges. They are characterized by small spring discharges and low winter snow accumulation. The heat exchanges are such that the ice sheet can slowly melt and disintegrate. Premature breakups are dominated by strong spring discharges resulting from a large and rapid snowmelt. The ice cover in this case is competent and strongly attached to the banks. The rise in discharge causes an increase in flow shear on the underside of the ice cover. From the rise in open-water level, the flow under the ice cover must be under pressure leading to an upward loading which can result in cracking near the banks. From the increase in flow shear, decrease in strength from cracking, and the uplift force, the driving forces may become sufficiently large to break or dislodge the ice cover pushing

it downstream.

Once the ice cover is free to move, it will experience large scale fracturing from changes in channel geometry. Eventually, successive collision between ice fragments lead to further breaking into smaller ice pieces. This type of breakup is common on flat rivers of medium size. On large or steep rivers, the breakup can be very abrupt, producing a potentially violent and destructive event. In this case, the original ice cover is often fractured in place, before freeing itself from the banks.

Recall that an ice cover increases the hydraulic resistance of the affected river reach, which can cause a backwater effect upstream of the head of the jam. In the spring or during a mid-winter thaw, when the driving forces on the jam exceed its resisting forces, the jam will fail and the stored water behind the ice cover is released, forming a surge or a flood wave. This surge is capable of significant flooding, damage to infrastructure, bank erosion, and bed scour. An ice run, made up of rubble from the released jam, follows the surge and may form subsequent ice jams downstream as it encounters intact ice covers or other obstructions. A breaking front occurs when rapidly fragmented ice “ploughs” through an intact ice cover downstream. Breaking fronts often have celerities in excess of 5 m/s and can ultimately result in a jam (Beltaos, 1995).

2.3.2 Analytical methods

While there have been quantitative data collected from field observations of ice jams since the nineteen-twenties, the first theoretical analysis of jamming on rivers is usually attributed to Kennedy (1958) on evaluating forces on booms from logjams. Kennedy based his analysis on “*the analogy between pulpwood in a river and granular material contained between two parallel walls*” (Beltaos, 1983). The analysis takes into account the shear on the underside of the cover opposed by the bank resistance, but neglects the downslope component of the jam’s weight and assumes that the jam thickness does not vary in the streamwise direction. Pariset et al. (1966) extended the analysis described above to include the downslope component of the jam’s weight. Their analysis still neglected any change in jam thickness along the river reach.

Uzuner and Kennedy (1976) formulated a time dependent relationship describing the force equilibrium within a jam. While the differential equation describing this phenomenon has no complete closed form solution, it was shown that after some time, the jam reaches a quasi-steady state. This state describes the steady advance of the head of the jam governed by the flux of the incoming ice floes. An observer moving with the head of the jam, which is propagating upstream, sees a steady state condition. Starting at the head of the jam, the thickness increases in the downstream direction

until it reaches an equilibrium value after which it remains constant. This is called the equilibrium thickness. Downstream of the equilibrium reach, there exists a transitional zone where the water surface profile steepens to meet the lower water level at the toe of the jam. Beltaos (1983) expands on the analysis by Uzuner and Kennedy (1976) to develop closed form solutions for thickness and water depth in equilibrium jams.

Early research focused on equilibrium jams; that is, ice jams that no longer evolve in time. These ice jam theories, however, cannot predict when, whether, nor where ice jams occur. Furthermore, the momentum effects of ice and water on the ice jam evolution and jam thickness are not considered.

Shen et al. (1990) developed an analytical framework for the dynamic transport of river ice. The analysis aims to describe the evolution process of surface ice jams, including the transport of surface ice, jam initiation, and the progression and collapse of ice jams. The ice mass is treated as a granular material described as a continuum. The continuum approach is valid for problems where the ice particles are much smaller than the river width, described further in Tsai et al. (1988). All the previous studies on equilibrium ice jams, including Pariset et al. (1966); Uzuner and Kennedy (1976) also treat the ice mass as a continuum. This approach enables developing equations of motion, e.g. conservation of mass and momentum, describing the continuum. Shen et al. (1990) formulated a set of three one-dimensional partial differential equations for the dynamic transport of river ice. They describe the changes of momentum, mass, and concentration of ice in the streamwise direction and in time. The set of equations also depends on the constitutive relationships for the internal ice stress and the bank resistance.

Recall in section 2.2 that one of the main challenges in describing granular flow is developing appropriate constitutive relationships to describe how the stress is generated. All the available constitutive relationships have a limited range of applicability, depending on particle velocity, concentration, and shear rate, among other parameters. There is no exception in the case of the dynamic transport equations of river ice, for example, the ones developed by Shen et al. (1990). To overcome this challenge, their study classifies the behaviour of the river ice into two regimes: rapid- and slow-flow, each with its own constitutive relationships. They base the classification on the interaction between ice particles, which depend on ice concentration, flow conditions, and ice properties.

As described in Shen et al. (1990), at lower concentrations, particle interactions between ice particles are mainly due to momentum exchanges by binary collisions, characteristic of the rapid flow regime. At higher concentrations, the internal resistance

is governed by prolonged inter-particle contact forces, which constitutes the slow flow regime. The description in this paragraph echoes the classification of granular flow regimes presented in section 2.2. Here, the rapid flow regime parallels the grain-inertia regime, and the slow flow regime is similar to the quasi-static and the static regimes.

For the rapid flow regime, Shen et al. (1990) uses a viscous-plastic constitutive relationship proposed by Hibler (1979). The relationship considers ice velocity, coefficient of restitution, internal friction angle, particle diameter, and particle concentration. In the slow flow regime, the stresses are calculated in a similar way to the static ice jam theory by Pariset et al. (1966), depending on jam thickness, ice concentration, internal angle of friction, coefficient of lateral thrust, and coefficient of passive earth pressure, described further in chapter 5.

The viscous-plastic approach proposed by Hibler (1979) is commonly used to model the rheological behaviours of ice when it is modelled as a continuum. This method provides constitutive relationships for internal stress and bank resistance so that the governing equations for dynamic ice transport can be solved. The nonlinear viscous-plastic constitutive law relates the internal ice stress to the strain rate of the ice flow. The ice is modelled as a viscous fluid for small strain rates and for large strain rates, the ice is assumed to flow in a plastic manner. During the ice stoppage and jamming process, ice floes behave more like a solid and its stress becomes independent of the strain rate. The viscous-plastic law approximates the rigid behaviour of a stationary ice mass by a state of very slow flow. This is one shortfall of the viscous-plastic model (Shen et al., 1997).

So far, all the analytical approaches presented herein have been one-dimensional. One-dimensional approaches have limited applicability since ice jam evolution depends on many two-dimensional characteristics including irregular channel geometry and non-uniform water currents. There are even some features in river ice dynamics that are inherently three-dimensional, or two-dimensional in the vertical-streamwise plane, including rafting, pile-up, and under-turning of ice floes. Hydrodynamic effects at the leading edge, and toe of an ice jam can also be three-dimensional.

Shen et al. (1993) developed a two-dimensional numerical model for dynamic surface ice transport. The unsteady shallow water equations were modified to account for effects of ice including additional hydraulic resistance from the surface ice, and flow through the surface ice layer. The hydrodynamics are solved using an Eulerian finite element method. The movement of ice is modelled using a Lagrangian particle method treating the ice mass as a continuous viscous-plastic fluid. The two models are coupled through mass and momentum exchanges at the ice-water interface. Computer

simulations of ice jam phenomena are described later in this section.

2.3.3 Ice jam mechanics

A physical description of river ice processes, from freeze-up to breakup, has been described earlier in this section. It should be highlighted that ice jams occur at both freeze-up and breakup. While there are differences between freeze-up and breakup jams, many of the processes are common to both. A river ice jam can be divided into three phases: initiation, evolution, and release. The phases are described below with emphasis on ice jam phenomena that are simulated in chapter 7.

Initiation - At freeze-up, colder weather causes an increased concentration of frazil slush and ice pans on the river surface. At breakup, warmer temperature results in fracture of the ice cover. In both cases, ice floes are transported downstream on the water surface. If the transport capacity decreases, or if the ice floes are arrested for any reason, an ice jam may form. There are several mechanisms in which this can occur. Three of them are discussed below: congestion, surface blockage, and the arrest of a breaking front.

Congestion occurs when the supply of surface ice exceeds the local transport capacity. At low ice concentrations, it is primarily the surface water velocity that determines the motion of an ice floe. With an increase in concentration, the effects of bank resistance and inter particle friction reduce the transport capacity of the affected river reach. These resisting forces slow the movement of surface ice and a jam may initiate. For low enough river velocities, incoming ice floes will not submerge and the congestion will result in a surface jam. Congestion is a common mechanism for jam initiation at freeze-up, since water discharge is low. Areas of reduced speed, natural constrictions, constrictions from border ice growth, or other obstructions all increase the likelihood of jam initiation by congestion.

While constrictions, obstructions, or speed reductions can promote congestion, Ettema (1990) showed that congestion could occur even without these characteristics. Before this study, the ice jam literature suggested that ice jams are initiated only with the presence of some type of obstruction. Simple laboratory experiments involving beads in a straight flume shed light on the process of jam initiation by congestion. It was observed that the wall resistance first decelerated the beads near the walls. As these beads decelerated, they experienced collisions with faster moving beads located farther from the wall, which in turn decelerated those beads due to the impact. The process continued until the entire channel width was covered in a contiguous layer of beads. The layer continued downstream as a shear flow on top of a faster moving fluid. The relative velocity between the fluid and the bead layer increased until beads at the

upstream edge started submerging, causing the bead layer to thicken. Eventually, the jam thickened enough so that its wall resistance and internal strength balanced the forces exerted by the water flow, at which point the jam became stationary. The study concluded that jams can be initiated in unobstructed channels, but given the long lengths of channel needed for the jam to initiate from bank resistance alone absent of obstructions, jams are more likely to initiate at obstructions which occur in most natural rivers.

Figure 2.2 is adapted from the original paper by Ettema (1990) showing how the congestion of beads progresses in the downstream direction. It is interesting to note the similarities between this schematic and the one in figure 2.1, showing the different granular flow regimes. The obvious difference is that the granular material in figure 2.1 is experiencing a Couette flow and the flow in figure 2.2, prior to bead submergence, is more akin to a planar Poiseuille flow. Nevertheless, the two exhibit a transition between flow regimes as the particle concentration increases. As the concentration of particles increases in figure 2.1, they eventually cluster and form columns spanning the entire width between the parallel plates. With a further increase in concentration, particles remain in contact with their neighbours, forming a contiguous layer across the flow width. With a sufficient increase in particle concentration, both flows form contiguous layers where extensive force networks between contacting solids develop. These similarities have prompted the writer to treat the ice phase as a granular material in the analysis and developments as part of this thesis.

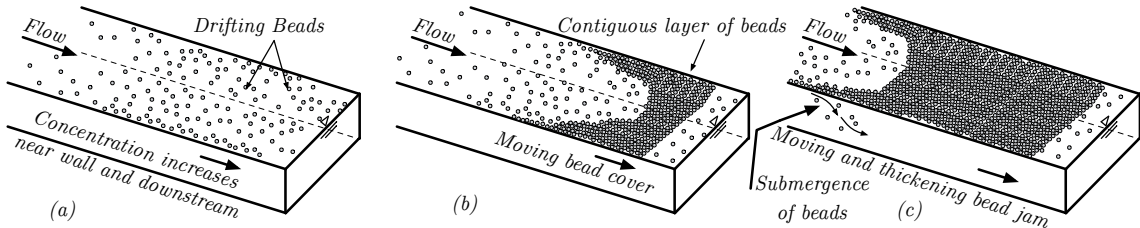


Figure 2.2 – Bead jam initiation in a straight flume. Adapted from Ettema (1990).

The following description pertains to surface blockage and ice block submergence. When ice floes approach a stationary ice cover, they either accumulate at the leading edge or they are entrained underneath the cover by the flow. To understand the mechanisms behind ice floe accumulation, it would be useful to determine under what flow conditions ice floes accumulate and under what conditions they submerge. If the approaching ice floes do not submerge, a surface jam will form, propagating upstream in a single layer. The interstitial water between the ice floes eventually freezes, and a continuous ice sheet will form. When ice floes submerge, there are several possibil-

ties: (1) for short jams, the ice floes may pass entirely under the jam, emerging on the downstream side into open water; (2) the ice floes may be deposited a distance downstream underneath the cover, hence, thickening the jam; (3) the ice floes may be large enough relative to the flow depth to lodge themselves between the stationary ice cover and the channel bed.

The following paragraph describes the submergence of an idealized, solid rectangular block of thickness t_i and length L approaching a stationary cover of equal thickness in a steady flow with an upstream velocity V . The problem is taken to be two-dimensional in the streamwise-vertical plane and a definition sketch is shown in figure 2.3. As the approaching ice block is arrested at the upstream face of the stationary cover, the flow accelerates as it passes underneath the block. The increase in velocity gives rise to a reduction in pressure, which causes the water level to drop slightly along the block. The pressure on the ice-water interface, however, must support the weight of the floating ice block; therefore, the reduction in pressure causes the block to sink. The flow around the bottom upstream corner of the floating block undergoes rapid vertical and horizontal accelerations, higher than those further along the block's length. These heightened accelerations result in a localized downward force near the upstream face, which can cause the block to rotate about its downstream end. This type of force results in what is commonly known as an under-turning moment. Flow separation may occur on the underside of the floating block, leading potentially to an additional downward force and under-turning moment. The buoyancy of the ice floe resists the downward forces and under-turning moments. Depending on the ice block's shape, it may submerge by under-turning or by vertical submergence without rotation, both shown in figure 2.4.

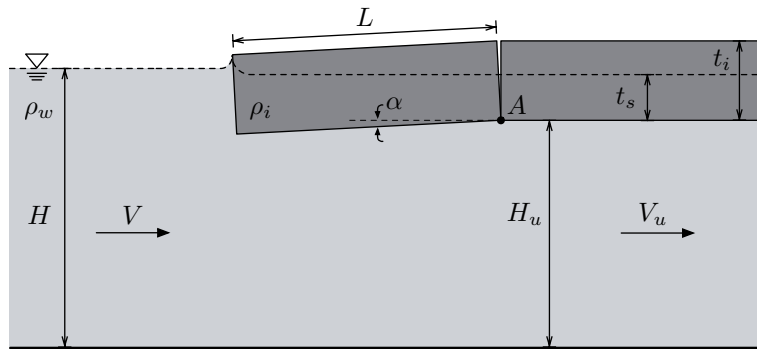


Figure 2.3 – Floating block stability: definition sketch.

Early studies focused on defining a critical velocity or densimetric Froude number based on approach velocity and block thickness for which an ice block approaching

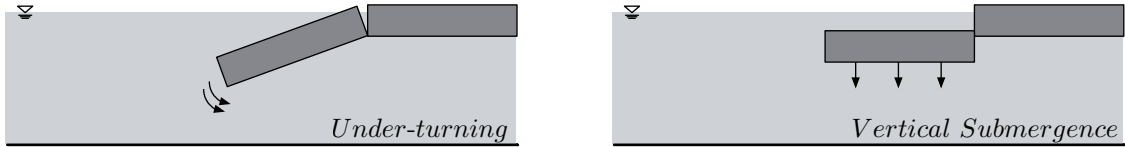


Figure 2.4 – Floating block stability: modes of submergence.

an intact ice cover would submerge (Pariset and Hausser, 1961; Uzuner and Kennedy, 1972; Ashton, 1974; Larsen, 1975). More detailed studies followed where a force-moment analysis was done considering a non-uniform pressure distribution underneath the floating ice block (Coutermash and McGilvary, 1993; Dow Ambtman et al., 2011a).

Pariset and Hausser (1961) introduced the concept of the “no spill” condition suggesting that the point of insipient motion is reached when the top upstream corner of a floating block is submerged. They proposed that this condition would be satisfied when the upstream velocity head exceeded the floating block’s freeboard. Uzuner and Kennedy (1972) conducted experiments in a flume to determine the critical Froude number for under-turning as a function of t_i/H , t_i/L , and ρ_i/ρ_w . They analyzed the stability through a one-dimensional moment analysis and found an empirical moment coefficient, which they thought to depend on t_i/L and ρ_i/ρ_w , remaining insensitive to changes in t_i/H . They considered instability to follow the “no spill” condition described by Pariset and Hausser (1961). Ashton (1974) developed a densimetric Froude number criterion, based on block thickness and density, for the limit of stability. A moment analysis was carried out and compared with experimental data from Uzuner and Kennedy (1972). Ashton found that stability depended on t_i/H and was relatively insensitive to changes in t_i/L .

Daly and Axelson (1990) analyzed the rotational stability of floating and submerged rectangular blocks using existing laboratory data. They considered the limit of stability to be reached when the under-turning moment acting on the block is equal to the maximum hydrostatic righting moment. The under-turning moment was calculated by defining a moment coefficient that relates the stability of a floating block to the dynamic pressure of the flow beneath it. Unlike Uzuner and Kennedy (1972), Daly and Axelson (1990) considered the moment coefficient to be sensitive to all of t_i/H , t_i/L , and ρ_i/ρ_w . The maximum hydrostatic righting moment was calculated as the sum of the moments about the point of rotation. Daly and Axelson (1990) also showed that the maximum hydrostatic righting moment occurs at an angle larger than the “no spill” condition. The forces on the upstream face of the floating block were not considered. They published a semi-empirical relationship defining a critical

densimetric Froude number in terms of the force moment analysis and two empirical regression coefficients.

Coutermash and McGilvary (1993) measured the dynamic pressure caused by fluid acceleration under a floating parallelepiped block for various velocities, block angles of attack, and block thickness-to-depth ratios. Investigators up to this point had assumed a constant pressure distribution under the block. Coutermash and McGilvary (1993) found that some of the pressures tended to stabilize the block while others tended to overturn it. The measured pressures were used to calculate an overturning moment, which could then be compared to the block's hydrostatic righting moment. From this, a densimetric Froude criterion was developed. Dynamic pressures associated with block rotation, such as rotational inertia and fluid added mass were not considered.

Dow Ambtman et al. (2011a,b) extended the works of Daly and Axelson (1990) and Coutermash and McGilvary (1993) by measuring the pressure distribution under a floating block and analyzing the block stability through a force-moment analysis. Depending on the block length, the dynamic pressure was characterized as either leading edge or Venturi effects dominated. For short blocks, the effects of the leading edge on the pressure distribution are more pronounced. For longer blocks, the dynamic pressure is relatively constant and equal to the reduction in pressure due to the increase in velocity under the ice cover. The effects of block rotation on the pressure distribution were examined. Pressures were only measured on the underside of the block; therefore, any forces acting on the upstream face of the block were ignored. The authors suggest that future work could consider the pressure distribution on all block faces as the block becomes entrained.

In chapter 7, numerical simulations are presented where a floating block approaches a stationary cover in an open-channel flow. The results are compared with some of the studies described above. In these simulations, the pressure is calculated on all the block faces and effects such as rotational inertia and fluid added mass are accounted for.

As alluded earlier in this section, ice rubble has been observed to “plough” its way through intact ice covers during breakup (Beltaos, 1995). For an ice cover of sufficient length and strength, the incoming ice rubble may stop mid-way through the cover and form a jam. The rubble may pile up and reach a considerable thickness, which poses a high risk of flooding. Jam initiation from the arrest of a breaking front is a common cause of ice jams during breakup.

Evolution - After a jam has been initiated, it will propagate upstream. Depend-

ing on the flow conditions in the channel and the internal strength of the ice, the accumulation will form either a surface jam or a thickened jam as described earlier in this section. Pariset et al. (1966) classified thickened jams into two types: (1) narrow channel jams, where its thickness is governed by the hydraulic conditions at the jam's leading edge; and (2) wide channel jams, where its thickness depends on the flow shear, channel width and slope, and the internal strength of the ice. Narrow channel jams form as a simple frontal progression of the head upstream without any shoving. That is, the highest thrust on the jam is experienced at the leading edge; therefore, the jam will not experience internal collapse. Wide channel jams form as a sequence of frontal progressions, followed by collapse, followed by additional thickening. The additional thickening is a consequence of the leading edge moving downstream due to the internal failure of the jam. This series of events is commonly referred to as telescoping. The additional thickening characteristic of a wide channel jam can result in considerably larger thicknesses relative to a narrow channel jam and thus poses a greater risk of flood events. Beltaos (1983) shows that narrow channel jams should be a rare occurrence on natural rivers, due to their high width-to-depth ratios.

While natural rivers never experience truly steady state conditions, oftentimes the temporal changes over which key parameters vary are small enough to assume a steady state. One of the most fundamental concepts in the analysis of ice jams is the idea of the equilibrium jam. Under steady state conditions including a steady supply of ice, equilibrium conditions can be established. Three zones can be identified along the equilibrium jam: (1) the upstream transition, (2) the equilibrium reach, and (3) the downstream transition, as shown in figure 2.5.

In the upstream transition, the jam gradually increases in thickness until it reaches a maximum at the start of the equilibrium reach. The increase in thickness in this zone reflects the series of frontal progression – collapse – thickening processes, which occurs near the head of the jam. In the equilibrium reach, the flow under the jam is more or less uniform and the water surface slope is equal to the bed slope, similar to open-water uniform flow conditions. With a sustained supply of ice, the equilibrium reach lengthens without changing the maximum water depth or the lengths of the transition zones. In the downstream transition, the water surface profile steepens to meet the lower stage at the toe of the jam. The shape of the downstream transition depends largely on the mechanism of jam initiation and the local hydraulic conditions. In general, what happens at the toe of the jam is not well understood, which presents a great challenge for assigning boundary conditions to model jam evolution (Beltaos, 1983).

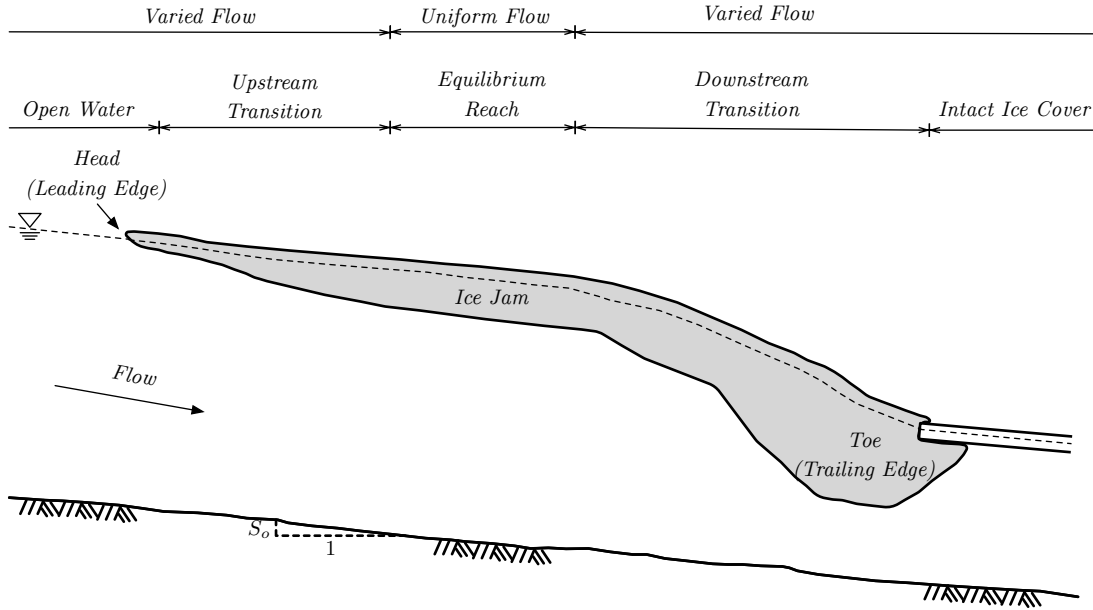


Figure 2.5 – Profile of an ice jam with an equilibrium reach.

Release - The cold temperatures and small river discharge make ice jam release during freeze-up rare (Beltaos, 1995). On the other hand, most ice jams at breakup release, given enough time. Most ice jam releases are sudden, giving rise to highly dynamic and potentially dangerous events. Upon release, flood waves travel both up and downstream. The wave propagating downstream can be metres high and can travel at speeds far above those during extreme open-water floods. Early research described this key mechanism in the mechanical breakup of river ice as the propagation of “surge” waves. Since these waves are not as steep as true surges, the term has been recast as “jam release waves” (Beltaos, 2007). Since large volumes of water stored behind a jam are let go upon release of an ice jam, many researchers have noted that this phenomenon is qualitatively similar to a dam break, although not as pronounced (Henderson and Gerard, 1981; Beltaos and Krishnappan, 1982; Wong et al., 1985; Jasek, 2003; Beltaos, 2007). These unsteady, highly dynamic events involve high stages, ice rubble and often fracturing ice. These complexities make modelling ice jam releases particularly challenging.

2.3.4 Computer simulations of river ice processes

Computer simulations play an important role in the analysis of ice jams by supporting field observations, laboratory experiments, and analytical methods. Because of the safety concerns and logistical issues surrounding field measurements, especially for dynamic ice processes, the analysis at times relies largely on laboratory experi-

ments, computer simulations, and qualitative observations. Numerical models of ice jams can be divided into two types: (1) static, and (2) dynamic ice jam models. Both are discussed below. Recent review articles addressing numerical models of ice jams include Carson et al. (2011), Shen (2010), and Beltaos (2008).

Most of the early numerical models assume steady-state conditions and apply the static ice jam theory by Pariset et al. 1966; Uzuner and Kennedy 1976; Beltaos 1983. The river stage is generally calculated using a backwater water analysis approach with Manning's equation or similar to calculate the water surface slope. Several steady one-dimensional non-equilibrium ice jam models have been developed including ICEJAM (Flato and Gerard, 1986), RIVJAM (Beltaos, 1993), and the ice-cover/ice-jam routine in HEC-RAS. A more comprehensive account of these models are described, compared, and assessed in Carson et al. (2011).

While the static ice jam models have had success estimating ice jam thickness and water levels, since dynamic effects are not considered, these models cannot predict whether, when, or where an ice jam will form. Furthermore, the effects of momentum from an unsteady flow can be significant. As mentioned earlier, non-uniform water currents, irregular channel geometry, and bank friction make many ice jam processes two-dimensional. For these reasons, dynamic and two-dimensional ice jam models have been developed.

DynaRICE by Shen et al. (2000) is a two-dimensional unsteady model for river ice dynamics. The river flow is calculated from the unsteady shallow water equations, which are modified to account for ice effects including increased hydraulic resistance from the underside of the ice cover and the flow through the ice surface layer. A finite element method is used to calculate the hydrodynamic part of this model. The surface ice is treated as a continuum and modelled in a similar manner to that of sea ice dynamics by Hibler (1979) and lake ice dynamics by Wake and Rumer Jr (1983). River ice dynamics, however, have considerably smaller spatial and temporal scales than sea or lake ice dynamics. As a result, river ice dynamics have much larger convective terms and larger variations in velocity and concentration (Shen, 2010). Most existing numerical models for sea and lake ice use traditional finite difference or finite element methods, which can introduce a large amount of numerical diffusion into the calculation. For this reason, DynaRICE is cast in a Lagrangian description using SPH (Shen et al., 2000).

Recall that in a Lagrangian approach, the continuum is made up of material points that move with the calculation points throughout the whole motion of the continuum. As a result, the material derivative reduces to a simple time derivative, eliminating

any numerical diffusion due to the convective terms. The Lagrangian description has also been shown to be more convenient in incorporating certain empirical criteria, for example, the entrainment of surface ice at the leading edge of the ice cover (Shen, 2010). DynaRice is now part of a more comprehensive river ice model called CRISSP (Comprehensive river ice simulation system) (Shen, 2002; Liu et al., 2006). The new model includes thermal effects as well as options for one- and two-dimensional analysis. DynaRice is not the only example of SPH being used to model ice jams.

Gutfraind and Savage (1997) studied broken-ice fields floating on the water surface and moving under the effects of wind. The ice was treated as a continuum and its rheological behaviour was described using the viscous-plastic model by Hibler (1979). SPH was also used in Gutfraind and Savage (1998) to study the unsteady flow of fractured ice through wedge-shaped channels. Similar to the previous paper, the motion of the ice was governed by the wind and water drag forces modelled with linear drag coefficients, and the internal stress in the ice modelled with a viscous-plastic relationship.

More recently, Nolin et al. (2009) studied the formation and release of river ice jams using a hybrid model. The hydrodynamics were calculated using a one-dimensional finite volume method solving the shallow water equations. The river ice dynamics were calculated using a two-dimensional SPH model. The SPH implementation was based on Shen et al. (2000) with a few modifications such as variable friction angle, and different treatment of bank friction. Application to an idealized test case and to an actual event show good results.

Tartakovsky et al. (2012) used a three-dimensional SPH model to study ice sheet and ice shelf dynamics. An accumulation of ice was simulated as it fell under the force of gravity down a slope into an initially still body of seawater. Since the ice is less dense than water, it detaches from the bedrock at some point and forms a shelf on the water surface. This point of detachment is called the grounding line. The simulated position of the grounding line was in good agreement with laboratory experiments for a broad range of bedrock slopes. Both the water and the ice were modelled using SPH, solving the full conservation of mass and momentum equations in a fully three-dimensional flow field.

All the numerical models presented thus far have treated the ice as a continuum. An alternative approach is to consider the forces applied on each ice floe from the water, riverbanks, and surrounding ice. This approach can be achieved using the DEM. By considering the motion and eventual arrest of each individual ice floe, new insight can be gathered about the formation, evolution, and release of an ice jam.

Furthermore, the DEM has been used for calculating forces on ice booms and other hydraulic structures (Hopkins and Tuhkuri, 1999; Daly and Hopkins, 2001; Hopkins and Tuthill, 2002; Hopkins and Daly, 2003; Sun and Shen, 2012).

In addition to studying broken ice fields using SPH, Gutfraind and Savage (1997, 1998) presented numerical results of the same problem using the DEM and compared the results with those obtained using SPH. Despite the two methods being drastically different, the numerical results shown are very similar. This result suggests that the complicated constitutive relationships required in the continuum mechanics approach can, in some circumstances, be accurately reproduced with relatively simple contact force schemes used in the DEM.

Most early DEM ice models were coupled with one-dimensional river flow models. More recently, Stockstill et al. (2009) have coupled their DEM model with a two-dimensional finite element river flow solver. In the earlier studies, the discrete elements were generally represented as two-dimensional circular floes in the streamwise – cross-stream plane (Babic et al., 1990; Hopkins et al., 1991; Loset, 1994; Sayed and Morse, 1999). In these models the ice floes are restricted to a single layer in the vertical; therefore, three-dimensional effects such as of ridging, pile-up, and overturning cannot be modelled. Pressure ridge formation of ice floes was studied using a two-dimensional DEM model in the vertical plane (Hopkins et al., 1991). Ice jam formation, however, depends on both vertical thickening and on lateral boundaries, which can require a three-dimensional model.

Hopkins et al. (1996); Hopkins and Tuhkuri (1999) developed a three-dimensional DEM model where the ice floes were represented as dilated circular discs with finite thicknesses. In the dilation process, an arbitrary shape is dilated by placing a sphere at every point inside the original shape. For example, if a single point is dilated, the resulting shape is a sphere. If a line segment is dilated, the resulting shape is a cylinder with hemispherical ends. In the case of a circular disc, the dilation process results in a three-dimensional circular disc with round edges along its circumference and a flat top and bottom. In many studies, this shape has served as an idealized geometry for an ice floe (Hopkins et al., 1996; Hopkins and Tuhkuri, 1999; Daly and Hopkins, 2001; Sun and Shen, 2012).

To quote Beltaos (2007) in a recent review on river ice breakup processes, “*DEM has a vast potential for dealing with complex ice-water interactions, which can be increasingly realized as computing power grows.*” This thesis attempts to show some of this vast potential by simulating ice fragments using the DEM and the fluid flow with SPH.

Chapter 3

Smoothed particle hydrodynamics

This chapter describes the fundamentals of the SPH method and its application to fluid dynamics. The mathematical framework is presented, followed by the SPH representation of the equations governing fluid flow. Numerical aspects including time integration, boundary conditions, and artificial viscosity are discussed. The chapter finishes with a slightly different SPH formulation that was used for the numerical simulations presented in this thesis.

From a mathematical point of view, the SPH method is based on the idea that the value of a function at a point can be approximated by interpolating over known values on a set of disordered points in its neighbourhood. This is achieved by representing the function as a convolution product with a smoothing kernel. The spatial derivatives of a function can be represented in a similar manner. One of the major novelties of the SPH method is the ability to represent derivatives without using finite differences or a computational mesh.

The kernel is one of the most important elements of the SPH method because it affects the efficiency and the accuracy of the calculation. It is a function that is centred on a particle of interest and extends outwards decreasing to zero. This non-zero region defines the area of influence, also called the kernel support. Only the SPH particles inside the kernel support are included in the interpolation. For the calculation to be valid, there are several conditions the kernel must satisfy. For example, it must be normalized, symmetric, and monotonically decreasing. The shape of a kernel generally resembles a Gaussian function except its tails go to zero over a compact region instead of extending to infinity. As a result, the interpolation is over a small set of neighbouring points, which decreases the computational demand.

SPH has been applied first to astrophysics, then to a range of fluid and solid mechanics problems. This thesis focuses on fluid mechanics problems. They are governed by the Navier-Stokes equations, which are a set of non-linear partial differential equations with no full analytical solution. They describe the flow of fluids by conservation of mass, momentum, and energy equations. Since there is no full analytical solution to the Navier-Stokes equations, simplifications are often made to them, and numerical solutions are frequently sought. For flows at high Reynolds numbers, the Navier-Stokes equations can be simplified by ignoring viscous effects. The resulting set of equations is called the Euler equations. This approximation is reasonable at high Reynolds numbers for the bulk of the flow outside the boundary layer. The results in this thesis

are calculated by numerically solving the Euler equations. SPH is one method used to calculate numerical solutions to partial differential equations including the Navier-Stokes equations and the Euler equations. The SPH formulation reduces these sets of non-linear partial differential equations to sets of ordinary differential equations, which are easier to solve.

Partial differential equations have more than one independent variable. In the case of the Navier-Stokes equations and the Euler equations, the dependant variables rely on both space and time, i.e. the independent variables. Therefore, to calculate a numerical solution, the problem is discretized both spatially and temporally. Classically, the problem is divided spatially onto a computational mesh defining the problem domain where the solution is sought. In the case of SPH, the fluid is discretized spatially onto a set of particles but there is no computational mesh that extends to the boundaries of the problem domain. Boundary conditions are imposed on the extremities of the problem domain so that features such as solid walls and open boundaries can be represented correctly. The initial conditions define the value of the fluid variables at the start of the calculation. The calculation is then advanced in time discretely by small increments called time-steps. If the time-step is too large, the solution will produce incorrect results. On the other hand, small time-steps lead to long computation times. Computational fluid dynamics problems are most often limited by available computing power; therefore, the choice of a suitable time-step is very important.

Solid boundaries are difficult to implement in SPH because the particles near the boundary have kernel supports that extend past the boundary into a region where the problem is not defined. Since the early developments of SPH were applied to astrophysical problems absent of solid boundaries, the method evolved without addressing this shortcoming for quite some time. More recently, there have been several ways proposed to mitigate this problem. They include adding layers of boundary particles outside the problem domain, so that SPH particles no longer have truncated supports. Another approach is to have a single layer of boundary particles located along the solid boundary exerting repulsive forces on the SPH particles, similar to forces used to model interactions between pairs of molecules. Regardless of the method used, it is crucial that boundary conditions are imposed accurately. If not, the error introduced from the boundary can affect the fluid, not only near the boundary, but eventually in the whole problem domain.

For many computational fluid dynamics applications where strong gradients such as shocks are present, the numerical scheme can become unstable. From a mathematical point of view, a shock is represented by a discontinuity. This can cause difficulty for

computer simulations because the problem domain is spatially discretized into finite intervals and the discontinuity may be located in between the intervals. In reality, a shock wave has a thin, finite thickness of only a few molecular mean free paths. For most practical applications, this distance is much smaller than the discretization size in the simulation. A dissipative term called artificial viscosity is added to stabilize the numerical scheme and allow for the simulation of shocks. Artificial viscosity smears sharp gradients and thickens the shock transition zone so that the shock can be resolved computationally. Artificial viscosity is not something exclusive to SPH, it appears in finite difference methods as well.

For numerical solutions to the Euler equations, another way to stabilize the scheme is to use a Riemann solver. This is also commonly used in finite volume methods. This approach exploits the fact that information travels through the fluid along particular directions called characteristics, which take on the form of shock, rarefaction, and contact waves. The Euler equations are then solved numerically as the superposition of local discontinuous solutions made up of a combination of these waves. This method avoids having to use artificial viscosity and generally performs better at reproducing shock phenomena.

The differences between Lagrangian and Eulerian methods were briefly described in section 2.1 and the advantages and disadvantages of each one were also highlighted. One variation of the SPH method is called SPH-ALE (Arbitrary Lagrangian-Eulerian), whereby the SPH particles can move in a Lagrangian, Eulerian, or an arbitrary frame of reference. The method attempts to capitalize on the advantages of both the Lagrangian and the Eulerian descriptions while minimizing their shortcomings. The SPH-ALE formalism, allows for a new boundary treatment that generally outperforms methods used in standard SPH. The ALE description enables a boundary to move with a velocity independent of the fluid velocity. The force on the boundary is calculated by integrating the pressure on each boundary surface element, determined by the solution of a partial Riemann problem.

Each topic in this chapter has been briefly introduced. They will be further developed and more formally addressed in the sections that follow.

3.1 Interpolation

SPH is based on the idea that a fluid can be represented as a discrete set of particles, each assigned with a set of fluid variables such as velocity, density, and pressure. These variables change over time according to the equations of continuity and momentum, governing the fluid flow. The fluid variables associated with a given particle can be interpolated from the known values at neighbouring particles. This is achieved by

kernel interpolation.

It is instructive to first look at the following case: consider a function f depending on a position vector \mathbf{x} on a problem domain Ω with a boundary $\partial\Omega$; f can be written as a convolution product with the Dirac delta function δ :

$$f(\mathbf{x}) = \int_{\Omega} f(\mathbf{x}') \delta(\mathbf{x} - \mathbf{x}') d\mathbf{x}', \quad (3.1)$$

where δ has the following properties:

$$\delta(x) = \begin{cases} 0 & \text{if } x \neq 0 \\ \infty & \text{if } x = 0 \end{cases}, \quad \int_{-\infty}^{\infty} \delta(x) dx = 1, \quad \int_{a-\epsilon}^{a+\epsilon} \delta(x-a) dx = 1 \quad \text{for } \epsilon > 0. \quad (3.2)$$

Equation (3.1) is exact, but since δ is a non-physical function with a singularity, it is more practical to replace it with a more regular function that approaches δ in its limit. This function is called a kernel W , which depends on a smoothing length h , defining its area of influence. The value of $f(\mathbf{x})$ can then be approximated by what is known as the *integral interpolant*:

$$f(\mathbf{x}) \approx \langle f(\mathbf{x}) \rangle = \int_D f(\mathbf{x}') W(\mathbf{x} - \mathbf{x}', h) d\mathbf{x}'. \quad (3.3)$$

Note that the kernel may not extend to the boundaries of the problem domain. Therefore, the interpolation may be over a localized region centred about the point having position vector \mathbf{x} . This region over which the interpolation occurs is called the *kernel support* $D(\mathbf{x})$. The distance h_t from the centre of the kernel to the edge of its support is proportional to smoothing length, i.e. $h_t = kh$, where k is a constant. If the kernel support includes only a subset of the points in the problem domain, the support is called *compact*. For practical applications, a compact support is appealing because there are fewer particles in each support; therefore, the calculation is less computationally demanding. For calculations near the boundary of the problem domain, the kernel support may extend past the boundary into a region where the problem is not defined. In this case, the kernel support is *truncated*. Truncated supports often present a challenge for imposing certain boundary conditions and they generally introduce error into the calculation.

Given that the value at a point with position vector \mathbf{x} is approximated from the values at its neighbouring points \mathbf{x}' , one expects that the closer the neighbouring

point is, the more influence it has on the value at \mathbf{x} . One would also expect that neighbouring points of equal distance would have equal influence on the value at \mathbf{x} . The kernel function should be chosen to satisfy these conditions; hence, it should be monotonically decreasing and symmetric. Table 3.1 presents a list of conditions that the kernel function should have.

Table 3.1 – Conditions on the kernel function.

Condition	Description
1. Normalized	$\int_D W(x - x', h) dx' = 1$
2. Approaches δ	$\lim_{h \rightarrow 0} W(x - x', h) = \delta(x - x')$
3. Positive on its support	$W(x - x', h) > 0 \text{ on } D$
4. Monotonically decreasing	$\nabla W(x - x', h) < 0 \text{ on } D$
5. Symmetric	$W(-(x - x'), h) = W(x - x', h)$
6. Compact support	$W(x - x', h) = 0 \text{ for } x - x' > kh$

The integral interpolant converges if the kernel satisfies conditions 1 and 2 (Fang et al., 2009). These two conditions are directly related to the definition of δ . Conditions 3 to 6 follow from the discussion above and are often required for the calculation to be valid.

Equation (3.3) can be rewritten in discrete form as a sum over a set of particles. The fluid variables are usually calculated at the position of each particle in the domain. For a particle a located at \mathbf{x}_a ,

$$\langle f(\mathbf{x}_a) \rangle \approx \sum_{b \in D_a} \frac{m_b}{\rho_b} f(\mathbf{x}_b) W(\mathbf{x}_a - \mathbf{x}_b, h), \quad (3.4)$$

where $b = 1, 2, \dots, N$ and N is the number of particles in the support of particle a denoted by D_a ; m_b , ρ_b , and \mathbf{x}_b are the mass, density, and position of particle b , respectively. The volume associated with particle b is $\frac{m_b}{\rho_b}$ which replaces the volume element $d\mathbf{x}'$. Equation (3.4) is called the *summation interpolant*. Figure 3.1 shows a general representation of a problem domain Ω discretized into a set of fluid particles. The fluid variables are interpolated at the point of interest, particle a marked in red, with a kernel support D_a containing particles b marked in blue. The support extends from particle a to its edge, a length h_t to the support boundary ∂D_a . The particles in light grey are beyond the support of particle a and do not influence its fluid variables and therefore do not take part in the interpolation. Figure 3.2 shows a different particle of interest that is located closer to the problem domain boundary $\partial\Omega$. The kernel support extends past $\partial\Omega$ into a region where the problem is not defined. The

kernel support in figure 3.2 is truncated and consequently has fewer particles than the support in figure 3.1. This particle deficiency can introduce error.

Monaghan (2005) uses a Taylor expansion to show that the integral interpolant of $f(\mathbf{x})$ is second-order accurate for interior regions where the support lies completely inside the problem domain. Near the boundary, where the support is truncated, the integral interpolant does not have second-order accuracy. It is much more difficult to estimate the error of the summation interpolant since the distribution of SPH particles changes with time. Particles that are originally distributed on a regular grid become disordered during the fluid motion. An error estimate based on uniformly distributed SPH particles would then under predict the true error. SPH particles, however, are not randomly distributed. The governing equations and the properties of the kernel determine their positions. These dependencies keep SPH particles in a nearly ordered structure. Therefore, an error estimate based on a random array of particles would over predict the true error.

It should be noted that figures 3.1 and 3.2 are schematic and that in practical applications, the kernel support is much smaller than the problem domain. Therefore, only particles on or near the boundary have truncated supports. Typical smoothing lengths are between 1.2 and 1.5 times the particle spacing (Oger et al., 2007). In two dimensions, a kernel with a smoothing length of 1.2 has about 20 interpolation points in its support.

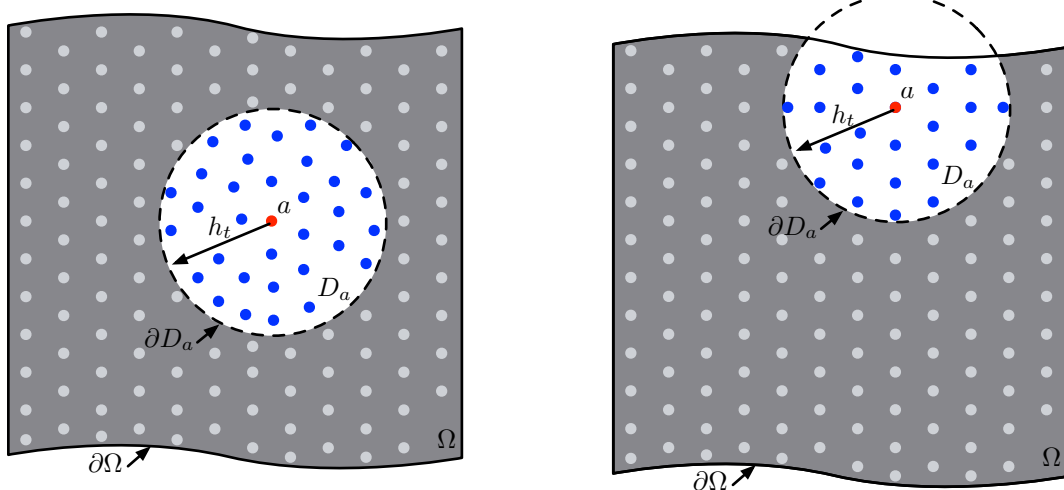


Figure 3.1 – Kernel support inside the problem domain that is discretized into a set of particles.

Figure 3.2 – Kernel support truncated by the problem domain that is discretized into a set of particles.

3.2 Interpolation of derivatives

Replacing $f(\mathbf{x})$ in (3.3) by its spatial derivative $\frac{\partial f(\mathbf{x})}{\partial \mathbf{x}}$ gives

$$\left\langle \frac{\partial f(\mathbf{x})}{\partial \mathbf{x}} \right\rangle = \int_D \left(\frac{\partial f(\mathbf{x}')}{\partial \mathbf{x}'} \right) W(\mathbf{x} - \mathbf{x}', h) d\mathbf{x}', \quad (3.5)$$

and using the product rule,

$$\left\langle \frac{\partial f(\mathbf{x})}{\partial \mathbf{x}} \right\rangle = \frac{\partial}{\partial \mathbf{x}'} \left(\int_D f(\mathbf{x}') W(\mathbf{x} - \mathbf{x}', h) d\mathbf{x}' \right) - \int_D f(\mathbf{x}') \frac{\partial W(\mathbf{x} - \mathbf{x}', h)}{\partial \mathbf{x}'} d\mathbf{x}'. \quad (3.6)$$

Applying the divergence theorem to the first term on the right-hand side of (3.6) yields

$$\left\langle \frac{\partial f(\mathbf{x})}{\partial \mathbf{x}} \right\rangle = \int_{\partial D} f(x') W(x - x', h) \cdot \mathbf{n} dS - \int_D f(\mathbf{x}') \frac{\partial W(\mathbf{x} - \mathbf{x}', h)}{\partial \mathbf{x}'} d\mathbf{x}'. \quad (3.7)$$

The first term on the right-hand side of (3.7) is a surface integral along the boundary of the kernel support. The value of the kernel along its boundary is zero. Therefore, this surface integral is zero if the kernel support is located entirely within the problem domain, i.e. if it is not truncated. Most classical SPH formalisms neglect this term. In doing so, the approximation for the spatial derivative of $f(\mathbf{x})$ simplifies to the second term on the right-hand side of (3.7). It should be noted that if the kernel support is truncated, the surface integral in (3.7) is normally not zero. There are two main approaches to mitigate this problem. One is to include this surface integral in the calculations to estimate the effect of the given boundary on the fluid. The other approach is more widely used and is to ignore the surface integral and use various techniques such as ghost particles or repulsive forces (Morris et al., 1997; Randles and Libersky, 1996; Monaghan, 1994) to impose the desired boundary condition.

In discrete form, as a sum over particles b in the support domain of particle a , the spatial derivative can be approximated by

$$\left\langle \frac{\partial f(\mathbf{x}_a)}{\partial \mathbf{x}_a} \right\rangle \approx - \sum_{b \in D_a} \frac{m_b}{\rho_b} f(\mathbf{x}_b) \frac{\partial W(\mathbf{x}_a - \mathbf{x}_b, h)}{\partial \mathbf{x}_b}. \quad (3.8)$$

Since the kernel function depends on the distance $r = |\mathbf{x}_a - \mathbf{x}_b|$ between particles and since W is symmetric,

$$\frac{\partial W(\mathbf{x}_a - \mathbf{x}_b, h)}{\partial \mathbf{x}_a} = \frac{(\mathbf{x}_a - \mathbf{x}_b)}{r} \frac{\partial W(\mathbf{x}_a - \mathbf{x}_b, h)}{\partial r}, \quad (3.9)$$

therefore,

$$\frac{\partial W(\mathbf{x}_a - \mathbf{x}_b, h)}{\partial \mathbf{x}_a} = -\frac{\partial W(\mathbf{x}_a - \mathbf{x}_b, h)}{\partial \mathbf{x}_b}, \quad (3.10)$$

and (3.8) can be rewritten as

$$\left\langle \frac{\partial f(\mathbf{x}_a)}{\partial \mathbf{x}_a} \right\rangle \approx \sum_{b \in D_a} \frac{m_b}{\rho_b} f(\mathbf{x}_b) \frac{\partial W(\mathbf{x}_a - \mathbf{x}_b, h)}{\partial \mathbf{x}_a}. \quad (3.11)$$

The SPH representation for a function and its derivative has been formulated. They can be written in condensed form as

$$f_a = \sum_{b \in D_a} \frac{m_b}{\rho_b} f_b W_{ab}, \quad (3.12)$$

and

$$\left(\frac{\partial f}{\partial \mathbf{x}} \right)_a = \sum_{b \in D_a} \frac{m_b}{\rho_b} f_b \frac{\partial W_{ab}}{\partial \mathbf{x}_a}, \quad (3.13)$$

where $W_{ab} = W(\mathbf{x}_a - \mathbf{x}_b, h)$. In this form, however, the representation of the derivative in (3.13) does not vanish if f is a constant function. This problem is solved by using the symmetric form of the derivative as in Monaghan (2005):

$$\frac{\partial f}{\partial x} = \frac{1}{\Phi} \left(\frac{\partial(\Phi f)}{\partial x} - f \frac{\partial \Phi}{\partial x} \right), \quad (3.14)$$

where Φ is any differentiable function. Equation (3.14) is nothing more than the product rule between f and Φ rearranged in terms of the derivative of f . For $\Phi = 1$, (3.13) becomes

$$\left(\frac{\partial f}{\partial \mathbf{x}} \right)_a = \sum_{b \in D_a} \frac{m_b}{\rho_b} (f_b - f_a) \frac{\partial W_{ab}}{\partial \mathbf{x}_a}, \quad (3.15)$$

and for $\Phi = \rho$

$$\left(\frac{\partial f}{\partial \mathbf{x}} \right)_a = \frac{1}{\rho_a} \sum_{b \in D_a} m_b (f_b - f_a) \frac{\partial W_{ab}}{\partial \mathbf{x}_a}. \quad (3.16)$$

The SPH expressions for a function and its derivative were derived with very little knowledge of the form of the kernel. Table 3.1 summarizes some general conditions

on the kernel for convergence and validity but it does not identify specific functions. The following section elaborates on the description of a few commonly used kernels.

3.3 Kernels

The kernel function is one of the most important components of the SPH method. It dictates how the fluid variables are interpolated. Consequently, its choice affects the accuracy, efficiency, and stability of the calculation. Given the conditions in table 3.1, it is not surprising that Gaussian-like kernels are commonly used. A true Gaussian has tails that extend to infinity; therefore, it lacks a compact support. Nevertheless, it is still used for some theoretical purposes because it can simplify the analysis. For practical applications, a Gaussian can be modified to have a compact support. A Gaussian kernel in one dimension is

$$W(r) = \frac{1}{\sqrt{\pi}} \exp(-r^2). \quad (3.17)$$

Spline-based kernels are commonly used. This family of functions by Schoenberg (1946) is of the form

$$W(r, h) = \frac{C}{h^d} f\left(\frac{r}{h}\right), \quad (3.18)$$

where C is a constant enforcing that the kernel is normalized and the exponent d is either 1, 2, or 3 for kernels in one, two, or three dimensions, respectively. The most popular of the spline-based kernels is the Cubic Spline defined as

$$W(q) = \frac{C}{h^d} \begin{cases} (2-q)^3 - 4(1-q)^3 & \text{for } 0 \leq q < 1 \\ (2-q)^3 & \text{for } 1 \leq q < 2 \\ 0 & \text{for } 2 \geq q \end{cases} \quad (3.19)$$

where $q = r/h$, and C is $1/6$, $5/14\pi$, or $1/4\pi$ for one, two, or three dimensions, respectively. For a Cubic Spline, the distance from the particle of interest to the edge of the support is $h_t = 2h$. Higher-order splines such as the Quartic or Quintic Splines, can be used to increase stability (Morris et al., 1997). The disadvantage is that the kernel support size increases, so more particles are included in each interpolation.

The Wendland kernel has some advantages over the Gaussian and the Cubic Spline (Macia et al., 2011). It has been shown, in some cases, to reduce particle clumping (Capone et al., 2007) and numerical dissipation (Robinson, 2009). The results in chapters 6 and 7 are from SPH simulations where the Wendland kernel was used. It is defined as

$$W(q) = \frac{C}{h^d} \begin{cases} (2-q)^4(1+2q) & \text{for } 0 \leq q < 2 \\ 0 & \text{for } 2 \geq q \end{cases} \quad (3.20)$$

where $C = 7/64\pi$ in two dimensions. Figure 3.3 compares the Gaussian, Cubic Spline, and Wendland kernels in one dimension. The Gaussian kernel has an infinite support, whereas the Cubic Spline and the Wendland kernels have compact supports and are zero for $q \geq 2$. The kernels are normalized so the area under each of them is equal to unity. Consequently, it is not surprising that the kernels with compact support have higher maxima than the Gaussian. Figure 3.4 shows the Wendland kernel in two dimensions. The kernel support is projected on the xy -plane as the circular colour-filled region. Inside the support lies the particle of interest a and the neighbouring particles b . The vertical axis represents the value of the kernel function for a given point on the xy -plane. This value can be thought of as the level of influence that the value at b has on the value at a .

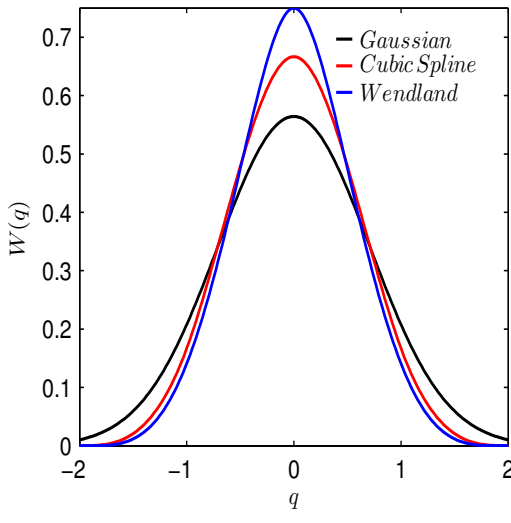


Figure 3.3 – Comparison of three different kernel functions for a one-dimensional problem.

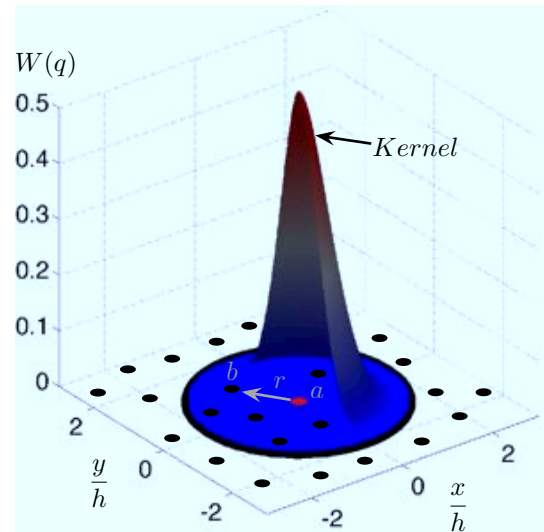


Figure 3.4 – The Wendland kernel function for a two-dimensional problem.

3.4 Application to fluid dynamics

In this section, it is demonstrated how the SPH method is used to solve fluid dynamics problems. The starting point will be the Navier-Stokes equations. Through scale analysis, simplifications will be made, leading to the Euler equations describing flow of an inviscid fluid. Finally, the Euler equations will be put into a discrete form

using the SPH representation of a function and its derivatives described in sections 3.1 and 3.2.

The results in chapters 6 and 7 present numerical simulations of fluid dynamics problems where water is the simulated fluid. In most circumstances, water can be considered as incompressible. In reality, water is slightly compressible where large changes in pressure result in very small changes in density. For example, the density of water increases by 0.5% when the pressure is increased from one to 100 atmospheres (Batchelor, 1967). For a slightly compressible fluid at constant temperature, the relevant Navier-Stokes equations governing the flow are

$$\begin{cases} \frac{\partial \rho}{\partial t} + (\mathbf{u} \cdot \nabla) \rho = -\rho(\nabla \cdot \mathbf{u}) \\ \rho \left(\frac{\partial \mathbf{u}}{\partial t} + (\mathbf{u} \cdot \nabla) \mathbf{u} \right) = -\nabla P + \mu (\nabla^2 \mathbf{u}) + \left(\zeta + \frac{1}{3}\mu \right) \nabla(\nabla \cdot \mathbf{u}) + \mathbf{f}_e, \end{cases} \quad (3.21)$$

where ρ is density, \mathbf{u} is velocity, P is pressure, μ is dynamic viscosity, ζ is the bulk viscosity, t is time, \mathbf{f}_e is the net external body force per unit mass, and ∇ represents the spatial derivative $\frac{\partial}{\partial \mathbf{x}}$. The first equation is conservation of mass, or continuity, and the second is conservation of momentum. Normally a third equation, conservation of energy, accompanies the two above. It is omitted in this case by neglecting thermal effects and considering a low viscosity fluid that is only slightly compressible. For simplicity, the net external force \mathbf{f}_e will only appear in specific cases where its presence is important. The second and third term on the right-hand side of the conservation of momentum equation relate to changes in momentum due to the viscosity of the fluid.

The flows considered in this thesis are at high Reynolds numbers. In other words, the inertial forces in the flow are much greater than the viscous forces. The momentum equation will be non-dimensionalized and scaled to show that for high Reynolds number flows, the viscous terms can be neglected. Let the characteristic length and velocity scale for the flow be L and U , respectively. The time scale is then $\frac{L}{U}$ and the pressure will be taken to scale as $P \sim \rho U^2$. The fluid in our case is only slightly compressible. From the continuity equation, it is clear that for small changes in density (compressibility), the divergence of the velocity field $\nabla \cdot \mathbf{u}$ is also small. For this reason, the term in the momentum equation containing $\nabla \cdot \mathbf{u}$ will be ignored, as will the external force term because it is case specific and cannot be scaled without further information. Let the non-dimensional quantities, in this section only, be denoted by the superscript $*$. For simplicity, we will consider a one-dimensional case. The

non-dimensional distance x^* , velocity u^* , and pressure P^* are

$$u^* = \frac{u}{U}, \quad x^* = \frac{x}{L}, \quad \text{and} \quad P^* = \frac{P}{\rho U^2}; \quad (3.22)$$

therefore

$$\frac{U^2}{L} \frac{\partial u^*}{\partial t^*} + \frac{U^2}{L} u^* \frac{\partial u^*}{\partial x^*} = -\frac{U^2}{L} \frac{\partial P^*}{\partial x^*} + \frac{U}{L^2} \frac{\mu}{\rho} \frac{\partial^2 u^*}{\partial x^{*2}}, \quad (3.23)$$

or

$$\frac{\partial u^*}{\partial t^*} + u^* \frac{\partial u^*}{\partial x^*} = -\frac{\partial P^*}{\partial x^*} + \frac{1}{Re} \frac{\partial^2 u^*}{\partial x^{*2}}, \quad (3.24)$$

where the Reynolds number is $Re = \frac{UL}{\nu}$ and the kinematic viscosity is $\nu = \frac{\mu}{\rho}$ with a value of $10^{-6} m^2/s$ for water. From (3.24), it is clear that for high Reynolds numbers, the viscous term in the momentum equation is negligible. There are several types of flows considered in this thesis, with geometries ranging from 1 to 100 m and velocities from 0.1 to 10 m/s. The smallest Reynolds number calculated from these scales still results in a viscous term that is five orders of magnitude smaller than the other terms in the momentum equation.

It should be noted that the result shown in (3.24) is applicable to the bulk flow away from the boundaries where the characteristic length scale is in fact L . Near the boundary, the characteristic length scale for the viscous forces is no longer L , but the characteristic thickness of the boundary layer, which is small. Because of the no-slip condition, the velocity near the boundary is small. Consequently, both the length and the velocity scales near the boundary are small, which results in low Reynolds numbers, meaning that viscous forces are important. Since the boundary layer thickness decreases as the Reynolds number increases, the Euler equations become a better and better approximation for increasing Re . Therefore, we will proceed by neglecting viscosity.

By neglecting viscosity, the Navier-Stokes equations simplify to the Euler equations governing the flow of an inviscid fluid. They are written here in both an Eulerian and a Lagrangian frame of reference. The Euler equations are

$$\begin{aligned} \text{Eulerian} & \left\{ \begin{array}{l} \frac{\partial \rho}{\partial t} + (\mathbf{u} \cdot \nabla) \rho = -\rho(\nabla \cdot \mathbf{u}) \\ \frac{\partial \mathbf{u}}{\partial t} + (\mathbf{u} \cdot \nabla) \mathbf{u} = -\frac{1}{\rho} \nabla P \end{array} \right. & \text{Lagrangian} & \left\{ \begin{array}{l} \frac{D\rho}{Dt} = -\rho(\nabla \cdot \mathbf{u}) \\ \frac{D\mathbf{u}}{Dt} = -\frac{1}{\rho} \nabla P \end{array} \right. \end{aligned} \quad (3.25)$$

where the Lagrangian derivative is expressed as $\frac{D}{Dt} = \frac{\partial}{\partial t} + (\mathbf{u} \cdot \nabla)$. In three dimensions, the Euler equations consist of one scalar equation, conservation of mass, and one vector equation, conservation of momentum, with three components, amounting to four equations in total. There are five unknowns: P , ρ , and three velocity components $\mathbf{u} = (u, v, w)^T$; therefore, there exists a closure problem.

If the fluid is considered truly incompressible, ρ is no longer a dependent variable; hence, the closure problem is solved. The continuity equation reduces to $\nabla \cdot \mathbf{u} = 0$. In this case, one can obtain an explicit expression for pressure in terms of velocity by taking the divergence of the momentum equation and eliminating the time dependence:

$$\overbrace{\frac{\partial(\nabla \cdot \mathbf{u})}{\partial t}}^{=0} + \nabla \cdot (\mathbf{u} \cdot \nabla) \mathbf{u} = -\nabla \cdot \left(\frac{1}{\rho} \nabla P \right); \quad (3.26)$$

therefore,

$$-\nabla^2 P = \rho \nabla \cdot ((\mathbf{u} \cdot \nabla) \mathbf{u}). \quad (3.27)$$

The pressure is expressed as some non-linear function of velocity in the form of Poisson's equation, $\nabla^2 P = f(u)$. The simplified form of the non-linear function is not important for this discussion. The significance of (3.27) is that the pressure field can be determined from the velocity field at the same instant in time. Furthermore, a change in velocity at one point in space instantly affects the pressure and resulting fluid acceleration everywhere else. This result follows from the incompressibility assumption in which the speed of sound becomes infinite. In this limit, sound waves carry pressure disturbances instantaneously across the entire fluid. The fact that there is no description on how pressure disturbances propagate across the fluid with time (no evolution equation for pressure) makes numerical solutions to the incompressible Euler equations challenging. The numerical solution attempts to impose zero velocity divergence (Cummins and Rudman, 1999), or zero change in density (Shao and Lo, 2003), or both (Hu and Adams, 2007).

Most SPH algorithms use a weakly compressible formulation where the density in the fluid is allowed to vary slightly. The closure problem is solved by using an equation of state to relate changes in pressure to changes in density. For SPH, the most widely used equation of state, described in Batchelor (1967), has the form

$$P(\rho) = \frac{\rho_0 c_0^2}{\gamma} \left[\left(\frac{\rho}{\rho_0} \right)^\gamma - 1 \right], \quad (3.28)$$

where ρ_0 is the reference density, c_0 is the speed of sound, and $\gamma \approx 7$. Equation (3.28)

predicts the propagation of sound waves in water and takes into account changes in pressure with small variations in density. Unlike a truly incompressible fluid, it takes time for a change in velocity at one point in space to affect the pressure at other points in the domain. The speed at which this occurs is governed by the speed of sound. It will be shown in section 3.5 that in numerical simulations, the minimum time-step size depends on the speed of sound. Although the speed of sound in water is $\sim 10^3 \text{ m/s}$, smaller numerical speeds of sound are often used to speed up the computation. The numerical speed of sound is generally chosen to ensure the fluctuations in density are less than 1%. If the pressure scales as $P \sim \rho_0 u^2$ where u is the velocity in the fluid, then rearranging (3.28) gives

$$\frac{\rho}{\rho_0} = \left(\frac{\gamma u^2}{c_0^2} + 1 \right)^{\frac{1}{\gamma}} \approx 1 + \frac{u^2}{c_0^2} + O \left(\left[\frac{\gamma u^2}{c_0^2} \right]^2 \right); \quad (3.29)$$

therefore,

$$\frac{|\delta\rho|}{\rho} \sim \frac{u^2}{c_0^2}. \quad (3.30)$$

It has been shown herein that the variations in density are proportional to the square of the Mach number $Ma = \frac{u}{c}$. From this relationship, it is clear that if the speed of sound is chosen as 10 times the maximum velocity in the fluid, $c_0 = 10u_{max}$, then the density fluctuations will stay below 1%.

The change in assumptions from treating the fluid as truly incompressible to treating it as slightly compressible may seem to be a minor detail from a physical point of view. Mathematically, this small modification changes the classification of partial differential equation from elliptic (Poisson's equation), to hyperbolic (the Euler equations). Consequently, the numerical methods used in each case differ substantially.

The weakly compressible SPH formulation will be shown here by discretizing the Euler equations shown in (3.25) in a Lagrangian frame of reference. The original SPH form by Gingold and Monaghan (1977), discretized the pressure gradient using (3.13):

$$\nabla_a P_a = \sum_{b \in D_a} \frac{m_b}{\rho_b} P_b \nabla_a W_{ab}, \quad (3.31)$$

so that the momentum equation becomes

$$\frac{D\mathbf{u}_a}{Dt} = -\frac{1}{\rho_a} \sum_{b \in D_a} \frac{m_b}{\rho_b} P_b \nabla_a W_{ab}. \quad (3.32)$$

This form does not conserve linear or angular momentum since the force on particle a

to b is not equal to the force on b to a :

$$F_{a \rightarrow b} = \frac{m_a m_b}{\rho_a \rho_b} P_b \nabla_a W_{ab} \neq F_{b \rightarrow a} = -\frac{m_b m_a}{\rho_b \rho_a} P_a \nabla_b W_{ba}, \quad (3.33)$$

since $P_a \neq P_b$, note $\nabla_a W_{ab} = -\nabla_b W_{ba}$ from (3.10). To solve this problem, the symmetric representation of the spatial derivative presented in (3.14) can be used. By doing so, the following two identities shown in Oger et al. (2007) can be proven:

$$\rho(\nabla \cdot \mathbf{u}) = \frac{\nabla(\rho^{\sigma-1} \mathbf{u}) - \mathbf{u} \nabla \rho^{\sigma-1}}{\rho^{\sigma-2}}, \quad (3.34)$$

and

$$\frac{\nabla P}{\rho} = \frac{P}{\rho^\sigma} \nabla \left(\frac{1}{\rho^{1-\sigma}} \right) + \rho^{\sigma-2} \nabla \left(\frac{P}{\rho^{\sigma-1}} \right), \quad (3.35)$$

where $\sigma \in \mathbb{R}$. Note that these identities correspond exactly to the right-hand side of the Euler equations in (3.25). Replacing $\rho(\nabla \cdot \mathbf{u})$ and $\frac{\nabla P}{\rho}$ by their SPH representations gives

$$\begin{cases} \frac{D\rho_a}{Dt} = \sum_b m_b \left(\frac{\mathbf{u}_a - \mathbf{u}_b}{\rho_a^{\sigma-2} \rho_b^{2-\sigma}} \right) \nabla_a W_{ab} \\ \frac{D\mathbf{u}_a}{Dt} = - \sum_b m_b \left(\frac{P_a}{\rho_a^\sigma \rho_b^{2-\sigma}} + \frac{P_b}{\rho_a^{2-\sigma} \rho_b^\sigma} \right) \nabla_a W_{ab}. \end{cases} \quad (3.36)$$

From this result, the two formulations most commonly found in literature can be expressed. Likely the more popular of the two, used by Monaghan, is found by setting $\sigma = 2$:

$$\begin{cases} \frac{D\rho_a}{Dt} = \sum_b m_b (\mathbf{u}_a - \mathbf{u}_b) \nabla_a W_{ab} \\ \frac{D\mathbf{u}_a}{Dt} = - \sum_b m_b \left(\frac{P_a}{\rho_a^2} + \frac{P_b}{\rho_b^2} \right) \nabla_a W_{ab}. \end{cases} \quad (3.37)$$

Vila (1999) and Colagrossi and Landrini (2003) use the following formulation by setting $\sigma = 1$:

$$\begin{cases} \frac{D\rho_a}{Dt} = \rho_a \sum_b \frac{m_b}{\rho_b} (\mathbf{u}_a - \mathbf{u}_b) \nabla_a W_{ab} \\ \frac{D\mathbf{u}_a}{Dt} = - \sum_b m_b \left(\frac{P_a + P_b}{\rho_a \rho_b} \right) \nabla_a W_{ab}. \end{cases} \quad (3.38)$$

Oger et al. (2007) notes that setting $\sigma = 1$ is a better formulation for multiphase flows with high density ratios, since the densities of both particles a and b appear in the continuity equation. Bonet and Lok (1999) and later Oger et al. (2007) show that the set of equations are consistent for any value of σ as long as the same one is used for both continuity and momentum.

3.5 Time integration

In any numerical scheme for time dependent problems, a suitable time-step must be chosen. It is generally a balance between choosing a time-step small enough to ensure numerical stability but large enough to maximize computational efficiency. For standard SPH methods, the time-step is governed by the Courant condition, the inertial forces, and the viscous time scale (for simulations with viscosity). It will be shown that the Courant condition is dependent on the numerical speed of sound and that the time-step of a simulation can be greatly increased by decreasing the speed of sound. This section shows how the Euler equations in SPH form can be integrated in time and how a suitable time-step is chosen.

The Euler equations have been spatially discretized into an SPH form. In doing so, the system of partial differential equations, dependent on space and time, has been reduced to a system of ordinary differential equations, dependent only on time. The spatial derivatives of the fluid variables have been re-expressed in SPH form using the summation interpolant.

Most SPH codes solve this set of ordinary differential equations using an explicit time integration scheme, for example Euler's method or higher-order Runge-Kutta schemes. For simplicity, the time integration is demonstrated herein using a first-order forward Euler scheme; however, the results in chapters 6 and 7 were calculated using a third-order Runge-Kutta scheme. Integrating the Euler equations in time gives

$$\begin{cases} \frac{\rho^{(n+1)} - \rho^{(n)}}{\delta t} = -\rho^{(n)}[\nabla \cdot \mathbf{u}]^{(n)} \\ \frac{\mathbf{u}^{(n+1)} - \mathbf{u}^{(n)}}{\delta t} = -\frac{1}{\rho^{(n)}}[\nabla P]^{(n)}, \end{cases} \quad (3.39)$$

where δt is the time-step from time n to $(n + 1)$. The Euler equations in (3.39) are expressed in a Lagrangian frame of reference. That is, a frame of reference following a fluid parcel in time. The position of these fluid parcels must also be integrated in time. For a fluid parcel with position vector \mathbf{x} , the time integration is

$$\frac{\mathbf{x}^{(n+1)} - \mathbf{x}^{(n)}}{\delta t} = \mathbf{u}^{(n+1)}. \quad (3.40)$$

Note, the equation of state contains no time derivatives, so it does not require a time integration scheme. At every time-step, the pressure at time n is related to the density at time n by (3.28). In SPH form, the set of equations governing the evolution of the fluid variables of a particle a is

$$\left\{ \begin{array}{l} \rho_a^{(n+1)} = \rho_a^{(n)} + \delta t \sum_b m_b \left(\mathbf{u}_a^{(n)} - \mathbf{u}_b^{(n)} \right) [\nabla_a W_{ab}]^{(n)} \\ \mathbf{u}_a^{(n+1)} = \mathbf{u}_a^{(n)} - \delta t \sum_b m_b \left(\frac{P_a^{(n)}}{[\rho_a^2]^{(n)}} + \frac{P_b^{(n)}}{[\rho_b^2]^{(n)}} \right) [\nabla_a W_{ab}]^{(n)} \\ \mathbf{x}_a^{(n+1)} = \mathbf{x}_a^{(n)} + \delta t \mathbf{u}_a^{(n+1)} \\ P_a^{(n+1)} = \frac{\rho_0 c_0^2}{\gamma} \left[\left(\frac{\rho_a^{(n+1)}}{\rho_0} \right)^\gamma - 1 \right]. \end{array} \right. \quad (3.41)$$

The set of equations in (3.41) consists of two scalar and two vector equations. In three dimensions, there are eight equations in total. The unknowns are P , ρ , three components of velocity $\mathbf{u} = (u, v, w)^T$, and three components of position $\mathbf{x} = (x, y, z)^T$, amounting to eight unknowns; therefore, the problem has closure.

The time-step is classically bounded by three conditions. The conditions presented below are the ones most commonly seen in SPH literature, but several variations exist. The Courant condition, in this case, limits the distance a sound wave can travel over a given time-step. If this condition is violated, unphysical pressure fluctuations may occur. The Courant condition can be expressed as

$$\delta t_1 = K \frac{h}{c_0(1 + 0.6\alpha)}, \quad (3.42)$$

where K is a coefficient less than 1 and α relates to the artificial viscosity described further in section 3.7. Inertial forces must be considered so that particles do not get too close to each other over a time-step. Morris et al. (1997) shows that

$$\delta t_2 = 0.25 \min_a \left(\sqrt{\frac{h}{|\mathbf{f}_a|}} \right) \quad (3.43)$$

is adequate, where $|\mathbf{f}_a|$ is the magnitude of the net external force on particle a , per unit mass. The last condition only applies if viscosity is considered. It restricts the time-step based on the viscous timescale using a characteristic length equal to the smoothing length. Following Morris et al. (1997),

$$\delta t_3 = 0.125 \frac{h^2}{\nu}, \quad (3.44)$$

where ν is the kinematic viscosity of the fluid. The last condition is often ignored and can be shown to be unnecessary except for low Reynolds number flows. The time-step is finally calculated by taking the minimum of the conditions above:

$$\delta t = \min(\delta t_1, \delta t_2, \delta t_3). \quad (3.45)$$

This time-step is used to advance the numerical simulation to the next time interval.

3.6 Boundary Conditions

When seeking the numerical solution to any boundary value problem, the proper implementation of boundary conditions is crucial. The same differential equation can have drastically different solutions by only slightly changing the boundary conditions. For this reason, it is possible for a small error in a boundary condition to introduce significant error into a numerical simulation. Due to its Lagrangian description and to kernel truncation, it is challenging to implement solid boundaries in SPH. On the other hand, free-surfaces are represented reasonably well without special treatment. Both solid and free-surface boundaries are discussed in this section.

Since the Navier-Stokes equations are a set of second-order partial differential equations, they require two boundary conditions for the problem to be well-posed. For impermeable surfaces, the no-slip condition is applied. It states that a fluid in contact with a solid body will have no velocity relative to the body at the contact surface. In other words, the velocity of the fluid in contact with the boundary is equal to the velocity of the boundary. This is true both normal and parallel to the contact surface, giving two boundary conditions. If we let \mathbf{u}_B denote the velocity of the boundary, the two boundary conditions can be compactly expressed as $\mathbf{u} = \mathbf{u}_B$, where \mathbf{u} is the velocity of the fluid in contact with the boundary. If the Navier-Stokes equations are simplified to the Euler equations by neglecting the viscous term, the set of partial differential equations reduces to first-order, requiring only one boundary condition to be well-posed. The no-slip condition is then relaxed to the no-penetration, or free-slip, condition which states that the fluid cannot penetrate the impermeable surface. In other words, the velocity of the fluid in contact with a surface must be equal to the velocity of the boundary in the direction normal to the contact surface. This can be expressed mathematically as $\mathbf{u} \cdot \mathbf{n} = \mathbf{u}_B \cdot \mathbf{n}$, where \mathbf{n} is a unit vector in the direction normal to the contact surface. The consequence of the free-slip condition is that the fluid velocity parallel to the wall is unrestricted.

There are three main methods to model solid boundaries in SPH. They are shown graphically in figure 3.5. The first method approximates the boundary by a collection of particles that moves with the boundary. The positions of these boundary particles remain constant relative to the boundary. They are arranged in layers extending out from the boundary. The layers are thick enough so that a fluid particle on or near the boundary no longer has a truncated support; therefore, the thickness must be greater than h_t . The region of fluid particle's support located outside the boundary is filled with what we will call *dummy particles*. They are included in the interpolation in a similar way to the fluid particles. To accurately calculate the density of a fluid particle near the boundary, the dummy particles must satisfy the continuity equation. For a boundary moving at a velocity \mathbf{u}_B , the boundary particles β are assigned the same velocity so that $\mathbf{u}_\beta = \mathbf{u}_B$ in the continuity equation. In the momentum equation, however, the boundary particle velocity \mathbf{u}_β is calculated differently, depending on which boundary condition is imposed and which order of accuracy is desired. A free-slip condition can be imposed by giving the dummy particle velocity \mathbf{u}_β the same normal component as the boundary velocity \mathbf{u}_B and the same tangential component as the fluid particle a . A zeroth order no-slip condition is achieved by setting $\mathbf{u}_\beta = \mathbf{u}_B$ in the momentum equation. Morris et al. (1997) introduced a first-order no-slip condition by extrapolating the velocity of the free fluid particles through the boundary to each dummy particle. In this case, the velocity of the dummy particles is anti-symmetric to the fluid particles. Their velocity gradient is equal to the velocity gradient at the boundary. For a fluid particle a with a velocity \mathbf{u}_a and distance d_a normal to the boundary, a dummy particle β located a distance d_β normal to the boundary has a velocity $\mathbf{u}_\beta = -\frac{d_\beta}{d_a} \mathbf{u}_a + \mathbf{u}_B$. Note, the positions of the dummy particles are not updated from the momentum equation; they remain fixed relative to the boundary.

The second boundary treatment follows the same idea as the first by adding particles outside the problem domain to fill the supports of fluid particles near the boundary. In this case, however, the particles are not fixed relative to the boundary. They are placed in a way that mirrors the fluid particles where the axis of symmetry is on the boundary. Randles and Libersky (1996) introduced this method known as *ghost particles*. A ghost particle has the same density and pressure as its corresponding fluid particle. Its position is updated at each time-step to ensure it is always a mirror image of the fluid particle. For a free-slip condition, a ghost particle has the same tangential velocity and opposite normal velocity as its corresponding fluid particle. For a no-slip condition, a ghost particle has opposite tangential and opposite normal velocities to its corresponding fluid particle. Since the positions of the ghost particles

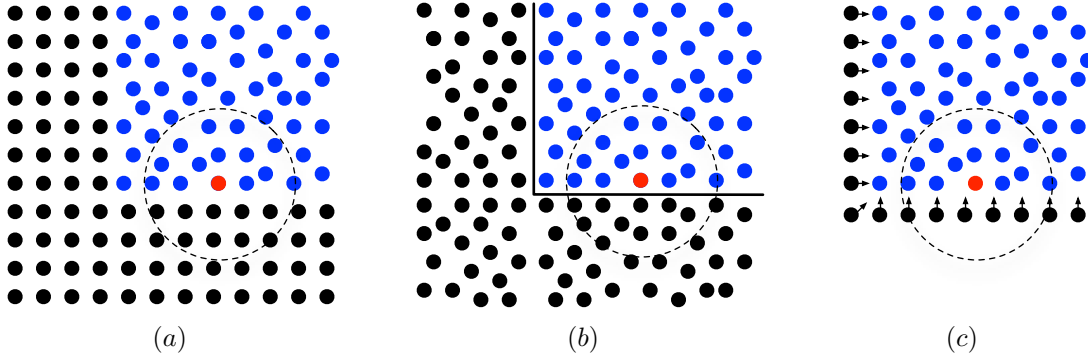


Figure 3.5 – Three types of boundary conditions for impermeable surfaces. The fluid particles are blue, the boundary particles are black, the particle of interest is red, and the kernel support is a dotted line. The three boundary conditions are: (a) dummy particles (b) ghost particles, and (c) repulsive force particles. Adapted from Robinson (2009).

are updated at every time-step, this method is more computationally demanding than the first one. In both methods, particles must be added to the outside of the problem domain. Consequently, it is challenging to accurately describe curved surfaces and sharp corners.

The third method does not require particles outside the problem domain. The boundary surface is defined by a single layer of particles that exerts repulsive forces radially on the fluid particles. The repulsive forces are similar to Lennard-Jones type forces describing the interaction between pairs of molecules. *Repulsive force particles* are presented in Monaghan (1994), with further developments described in Monaghan et al. (2003) and Monaghan (2005). This method can handle complex boundary surfaces more easily than the previous two, but at the cost of lower accuracy.

A fourth method is discussed in section 3.9, where the SPH-ALE method used in this work is described. The pressure on each surface element that makes up the boundary is calculated by solving a partial Riemann problem between the boundary surface and the neighbouring fluid. The value of pressure on the boundary is included in the SPH interpolation corresponding to the surface integral in (3.7). This surface integral is neglected in most standard methods. This boundary treatment is well suited for complex geometries and moving boundaries.

A free-surface is another type of boundary that changes position and shape with time. Its form is governed by the fluid motion and cannot be prescribed independently. As a result, such a boundary condition can be challenging to model with traditional grid-based methods. For a free-surface that does not interact with its surroundings, one boundary condition that can be imposed is zero pressure on the free-surface.

Since no pressure is exerted on the fluid at the free-surface, there are no resultant forces that can change the velocity. In this case, the surroundings do not contribute to the pressure, density, or velocity of the fluid. From an SPH viewpoint, consider a fluid particle a on or near a free-surface. Although particle a has a truncated support, the region in its support that is outside the free-surface does not influence the fluid variables at a . Therefore, the interpolation over this region should be zero. Since there are no particles in this region, the result of any interpolation of it will be in fact zero. Despite the fact that the fluid particles near the free-surface have truncated supports, their interpolations result in a zero pressure boundary condition being imposed on the free-surface. This is why SPH is often said to have a natural treatment of free-surfaces.

3.7 Artificial viscosity

For a fluid modelled by the Euler equations, information travels along particular directions called characteristics. These characteristics take on the form of non-linear acoustic (sound) waves and linear contact waves. The acoustic waves are either shock waves (compressive) or rarefaction waves (expansive). From a numerical point of view, shock waves are challenging to capture and their presence hinders the use of many methods. Using an inappropriate method can lead to spurious pressure oscillations near the shock or computing the shock with the wrong strength (LeVeque, 1992). Note that the SPH method presented so far makes no effort to determine the characteristics and use them in the numerical scheme.

For SPH particles distributed evenly on a Cartesian grid, the interpolation method is similar to a central difference scheme (Ben Moussa and Vila, 2000). Furthermore, the fluid variables \mathbf{u} , ρ , and P are all located at the same points in space. This amounts to using a central difference scheme on a collocated grid, which is well known to be unstable (Anderson and Wendt, 1995). For this reason, a diffusive term called artificial viscosity is added to stabilize the numerical scheme. A similar approach is taken in many finite difference methods. Monaghan and Gingold (1983) proposed that an artificial viscosity term be added to the pressure term, resulting in a momentum equation of the form

$$\frac{D\mathbf{u}_a}{Dt} = - \sum_b m_b \left(\frac{P_a}{\rho_a^2} + \frac{P_b}{\rho_b^2} + \prod_{ab} \right) \nabla_a W_{ab}, \quad (3.46)$$

and

$$\prod_{ab} = -\nu \frac{(\mathbf{u}_a - \mathbf{u}_b) \cdot (\mathbf{x}_a - \mathbf{x}_b)}{|\mathbf{x}_a - \mathbf{x}_b|^2 + \epsilon h^2}, \quad \nu = \begin{cases} \frac{\alpha h c_0}{\frac{1}{2}(\rho_a + \rho_b)} & \text{for } (\mathbf{u}_a - \mathbf{u}_b) \cdot (\mathbf{x}_a - \mathbf{x}_b) < 0 \\ 0 & \text{otherwise,} \end{cases} \quad (3.47)$$

where ϵh^2 is added to prevent a singularity at $|\mathbf{x}_a - \mathbf{x}_b|^2 = 0$. The coefficient α is a case specific constant and the user must choose a value high enough to achieve numerical stability but low enough to limit the amount of numerical diffusion being introduced.

While artificial viscosity remediates problems such as oscillations near shocks, it does so by smearing sharp gradients and dissipating energy at levels that can be much greater than the physical reality. For problems where wave propagation and energy conservation are important, using a high artificial viscosity can lead to erroneous results. For example, artificial viscosity can dissipate the energy in water wave propagation resulting in an under estimation of wave height (Guilcher et al., 2007). An alternative approach to adding artificial viscosity is to use a Riemann solver, which is a method used in many computational fluid dynamics codes. Riemann solvers propagate the characteristics throughout the fluid media and tend to capture high-resolution flow features such as shock waves that are often lost using other methods.

3.8 Riemann solvers

Riemann solvers increase the stability of the numerical scheme without explicitly adding artificial viscosity. The Riemann problem represents a solution to a system of hyperbolic conservation laws subject to initial conditions at two different states separated by a discontinuity. In this section, it will be shown that the Euler equations are in fact a system of hyperbolic conservation laws and their solution can be approximated by a superposition of solutions to local Riemann problems. Numerically, this means that solutions to the Riemann problem are found between calculation points. Each point has fluid variables with different values of \mathbf{u} , ρ , and P . The interface between two calculation points can be thought of as a discontinuity between these two values. The characteristics of the Euler equations are found at each discontinuity to determine how the information is being propagated to the rest of the fluid. The characteristics are combinations of shock, rarefaction, and contact waves that are used to find the solution of the local Riemann problem. The superposition of these local solutions makes up the global solution to the Euler equations.

There exists an exact solution to the Riemann problem for the Euler equations, first solved by Godunov (1959). This solution, however, cannot be expressed in a

closed-form; therefore, it is found iteratively to any desired, practical degree of accuracy. Exact solutions are often computationally demanding and can be replaced with approximations. Nonetheless, the exact solution can serve as a reference to assess the performance of an approximate numerical method.

A system of conservation laws can be expressed in integral form as

$$\frac{d}{dt} \int_{\Omega} \Phi d\Omega + \int_{\partial\Omega} \mathbf{F}(\Phi) \cdot \mathbf{n} dS = 0, \quad (3.48)$$

or in differential form as

$$\frac{\partial \Phi}{\partial t} + \frac{\partial \mathbf{F}(\Phi)}{\partial \mathbf{x}} = 0, \quad (3.49)$$

where Φ is a vector of conserved quantities $(\phi_1, \phi_2, \dots, \phi_n)^T$ and $\mathbf{F}(\Phi)$ contains flux vectors in columns $(F^{(1)}, F^{(2)}, \dots, F^{(m)})$ consisting of fluxes $(f_1, f_2, \dots, f_n)^T$ in rows. For a multi-dimensional problem, a new flux vector is added for each new dimension. In three dimensions, (3.49) becomes

$$\frac{\partial \Phi}{\partial t} + \frac{\partial \mathbf{F}^{(1)}(\Phi)}{\partial x} + \frac{\partial \mathbf{F}^{(2)}(\Phi)}{\partial y} + \frac{\partial \mathbf{F}^{(3)}(\Phi)}{\partial z} = 0. \quad (3.50)$$

There are important differences between (3.48) and (3.49). The integral form is more fundamental and can allow for discontinuous solutions. The differential form requires continuous solutions since the derivative of a quantity at a discontinuity is undefined. When viscosity is present, sharp gradients are smeared by viscous diffusion. In the absence of viscosity, as in the case of the Euler equations, these gradients remain abrupt. The solutions in this case admit discontinuities; therefore, the differential form is no longer valid. For this reason, it is preferable to remain with the more fundamental integral form if possible. Nevertheless, manipulations are more easily done in differential form; therefore, it is still used for some purposes.

The physical interpretation of (3.48) is that the state variables Φ enclosed by a control volume Ω , in the absence of sources or sinks, can only change by the flux of Φ through the boundary of the control volume $\partial\Omega$. From a numerical viewpoint, imagine that the fluid is discretized into small control volumes that make up a computational grid. The local enforcement of (3.48) on each cell is the basis of finite volume methods. Moreover, Riemann solvers are often used in finite volume methods. Classical SPH is not based on (3.48) so the quantities Φ are not necessarily conserved. Suppose now the computational domain is discretized into small control volumes represented by particles that can move with the flow and exchange fluxes of conserved quantities

with their neighbours. This description has similarities to both SPH and finite volume methods. Following this supposition, the next two sections present an alternative SPH formulation based on conservation laws that shows some resemblance to finite volume methods.

The conservative form of the Euler equations can be derived from first principles, or from the Reynolds Transport Theorem, or shown by reverting back from the non-conservative form in (3.25). Since the non-conservative form has been shown earlier without proof, it will serve as the starting point. From the non-conservative form, and using tensor notation where the summation is over repeated indices, the continuity equation becomes

$$\begin{cases} \frac{\partial \rho}{\partial t} + u_j \frac{\partial \rho}{\partial x_j} = -\rho \frac{\partial u_j}{\partial x_j} \\ \frac{\partial \rho}{\partial t} + \frac{\partial(\rho u_j)}{\partial x_j} = 0, \end{cases} \quad (3.51)$$

and the momentum equation becomes

$$\begin{cases} \frac{\partial u_i}{\partial t} + u_j \frac{\partial(u_i)}{\partial x_j} = -\frac{1}{\rho} \frac{\partial P}{\partial x_i} \\ \frac{\partial(\rho u_i)}{\partial t} - u_i \frac{\partial \rho}{\partial t} + \frac{\partial(\rho u_i u_j)}{\partial x_j} - u_i \frac{\partial(\rho u_j)}{\partial x_j} = -\frac{\partial P}{\partial x_i} \\ \frac{\partial(\rho u_i)}{\partial t} + \frac{\partial}{\partial x_j} (\rho u_i u_j + P \delta_{ij}) = u_i \underbrace{\left(\frac{\partial \rho}{\partial t} + \frac{\partial(\rho u_j)}{\partial x_j} \right)}_{=0 \text{ (from continuity)}} \\ \frac{\partial(\rho u_i)}{\partial t} + \frac{\partial}{\partial x_j} (\rho u_i u_j + P \delta_{ij}) = 0, \end{cases} \quad (3.52)$$

where δ_{ij} is the Kronecker delta having a value of 1 for $i = j$ and 0 otherwise. Expanding the conservative expressions for continuity and momentum in two dimensions gives

$$\frac{\partial}{\partial t} \begin{bmatrix} \rho \\ \rho u \\ \rho v \end{bmatrix} + \frac{\partial}{\partial x} \begin{bmatrix} \rho u \\ P + \rho u^2 \\ \rho vu \end{bmatrix} + \frac{\partial}{\partial y} \begin{bmatrix} \rho v \\ \rho uv \\ P + \rho v^2 \end{bmatrix} = 0. \quad (3.53)$$

Equation (3.53) is of the form in (3.49) where

$$\Phi = \begin{bmatrix} \rho \\ \rho u \\ \rho v \end{bmatrix}, \quad \mathbf{F}^{(1)} = \begin{bmatrix} \rho u \\ P + \rho u^2 \\ \rho v u \end{bmatrix}, \text{ and } \mathbf{F}^{(2)} = \begin{bmatrix} \rho v \\ \rho u v \\ P + \rho v^2 \end{bmatrix}. \quad (3.54)$$

Equation (3.53) can also be put into the integral form in (3.48). Although the pressure P is not a state variable in Φ , it is related to ρ by the equation of state in (3.28); therefore, the flux vector \mathbf{F} is in fact a function of Φ only. The pressure can be replaced by defining a new variable $c = c_0 \left(\frac{\rho}{\rho_0}\right)^{\frac{\gamma-1}{2}}$ so that $\partial P = c^2 \partial \rho$.

The Euler equations are written in conservative, differential form in (3.53). When solving these equations numerically in two or three dimensions, one can seek the solution of split Riemann problems. For example, the x -split Riemann problem considers only the fluxes in the x -direction. Split Riemann problems can be solved in each direction to ultimately have a full solution. For the SPH method, a multi-dimensional problem reduces to a set of one-dimensional Riemann problems between neighbouring particles. That is, the solutions to local Riemann problems are found at the midpoint between particles along the direction that connects them.

Let us define a unit vector \mathbf{n}_{ab} pointing from particle a to particle b and let a local $x = 0$ be at the midpoint between these two particles located at the global position vector \mathbf{x}_{ab} . Suppose that particle a is to the left of the midpoint and particle b is to the right. The direction tangent to \mathbf{n}_{ab} at $x = 0$ defines the interface between the state variables Φ_a at a and Φ_b at b . At the interface, there exists a discontinuity in state variables. This discontinuity of left and right states, along with the system of conservation laws forms the Riemann problem

$$\begin{cases} \frac{\partial \Phi}{\partial t} + \frac{\partial}{\partial \mathbf{x}(\mathbf{n}_{ab})} (\mathbf{F}(\Phi) \cdot \mathbf{n}_{ab}) = 0 \\ \Phi(x, 0) = \begin{cases} \Phi_a & \text{for } x < 0 \\ \Phi_b & \text{for } x > 0, \end{cases} \end{cases} \quad (3.55)$$

where the spatial derivative $\frac{\partial}{\partial \mathbf{x}(\mathbf{n}_{ab})}$ is evaluated along the direction \mathbf{n}_{ab} . The Riemann problem has a similarity solution depending only on x and t as a single variable $\frac{x}{t}$, with initial conditions from the left and right states Φ_a and Φ_b . It is represented graphically in figure 3.6. The solution is denoted by $\Phi^* = \Phi(\frac{x}{t}; \Phi_a, \Phi_b)$. The characteristic speeds can be represented on the space-time plane as rays connected to the initial discontinuity at $x = 0$. Suppose we wish to calculate the fluxes from the interacting particles a and b . For simplicity, suppose the vector \mathbf{n}_{ab} is aligned with the x -axis. These fluxes are

then in the x -direction. Since $\frac{\partial \mathbf{F}(\Phi)}{\partial x} = \frac{\partial F}{\partial \Phi} \frac{\partial \Phi}{\partial x}$, equation (3.53) can be re-expressed as

$$\frac{\partial \Phi}{\partial t} + \mathbf{A}(\Phi) \frac{\partial \Phi}{\partial x} = 0, \text{ with } \mathbf{A}(\Phi) = \begin{bmatrix} 0 & 1 & 0 \\ c^2 - u^2 & 2u & 0 \\ -uv & v & u \end{bmatrix}. \quad (3.56)$$

The system is hyperbolic if the matrix \mathbf{A} contains real eigenvalues and is diagonalizable. Its eigenvalues are

$$\begin{aligned} \lambda_1 &= u \\ \lambda_2 &= u + c \\ \lambda_3 &= u - c. \end{aligned} \quad (3.57)$$

Since the eigenvalues are real and distinct, the matrix \mathbf{A} is diagonalizable. Therefore, the Euler equations are hyperbolic. It is very important to know the type of system of equations in order to choose an appropriate method to solve them. If the fluid is treated as truly incompressible, the governing equations are no longer hyperbolic and a different solution method is needed.

The eigenvalues in (3.57) are the characteristic speeds determining how information is propagated in the fluid. At each point, there are three characteristics: two non-linear acoustic waves (either a shock or rarefaction) travelling at speeds $u \pm c$ and one linear contact wave travelling at a speed u . The characteristics can be plotted on the xt -plane as rays dividing the solution space into four regions shown in figure 3.7.

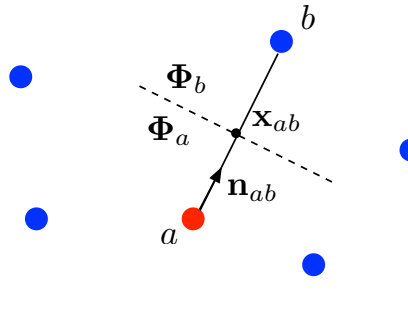


Figure 3.6 – Riemann problem between neighbouring particles. Adapted from Marongiu (2007).

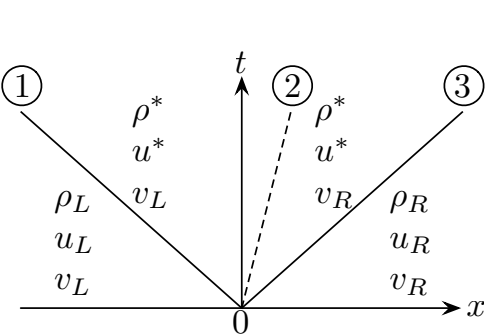


Figure 3.7 – Riemann solution structure.

The state variables in each region are, from left to right: Φ_L , Φ_L^* , Φ_R^* , and Φ_R . If particle a is to the left of the interface and particle b to the right, then $\Phi_L = \Phi_a$ and $\Phi_R = \Phi_b$. The eigenvalues λ_1 , λ_2 , and λ_3 correspond to waves 1, 2, and 3, respectively, labelled in figure 3.7. The region between waves 1 and 3 is the star region. The values in this region are unknown and determined by solving the Riemann problem. Waves

1 and 3 can either be shocks or rarefaction waves. Wave 2 is always a contact wave. If $u_L - c_L < u^* - c^*$, the speeds of the characteristics increase from left to right leading to a smooth transition in the form of a rarefaction wave. By a similar argument, if $u^* + c^* > u_R + c_R$, the speeds of the characteristics decrease from left to right leading to a discontinuity in the form of a shock wave. The solution to the Riemann problem can have any combination of rarefaction and shock waves. Figure 3.8 shows an example of a solution to the Riemann problem with a rarefaction wave and a shock wave.

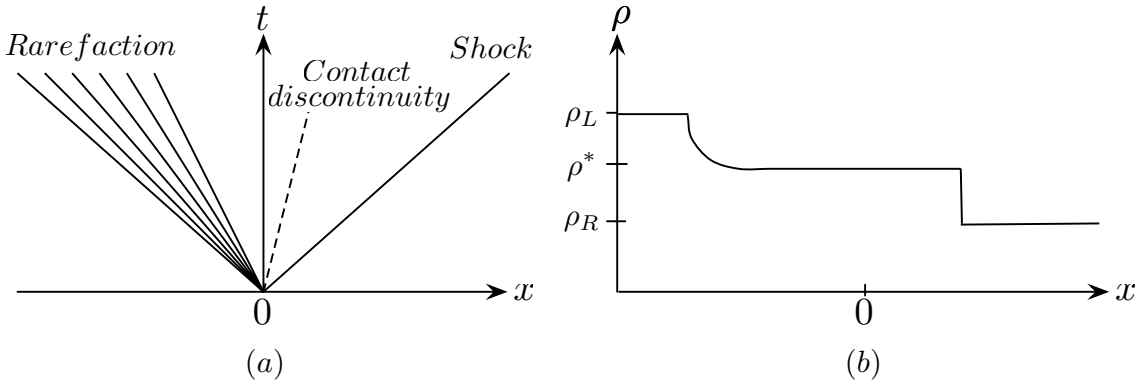


Figure 3.8 – An example of a Riemann solution with a rarefaction wave, contact discontinuity, and a shock wave. (a) Characteristics shown as waves propagating from the initial discontinuity. (b) The first component of the solution ρ is shown at some time after $t = 0$.

Considering the combinations of rarefaction and shock waves, there are four cases in total, shown in figure 3.9. To determine the exact solution, each case must be considered individually. Exact solutions are outlined in detail in Toro (1999) or LeVeque (1992). Marongiu (2007) shows an exact solution using the same equation of state as in (3.28). These solutions are somewhat cumbersome and computationally demanding. There are many approximate Riemann solvers varying in accuracy, speed, and applicability. A simple one is described herein. The VFRoe scheme by Masella et al. (1999) and described further for SPH applications in Marongiu et al. (2010) solves a linearized Riemann problem. The solution is

$$\left\{ \begin{array}{l} \rho^* = \frac{1}{2}(\rho_L + \rho_R) - \frac{1}{2\bar{c}} [(\rho u)_R - (\rho u)_L] \\ (\rho u)^* = \frac{1}{2} [(\rho u)_L + (\rho u)_R] - \frac{\bar{c}}{2}(\rho_R - \rho_L) \\ v^* = \begin{cases} v_L & \text{for } x/t < u^* \\ v_R & \text{for } x/t > u^*, \end{cases} \end{array} \right. \quad (3.58)$$

where $\bar{c} = \frac{1}{2}(c_L + c_R)$. All the quantities in the star region are known so the Riemann problem is solved. One motivation for using a Riemann solver is to avoid using

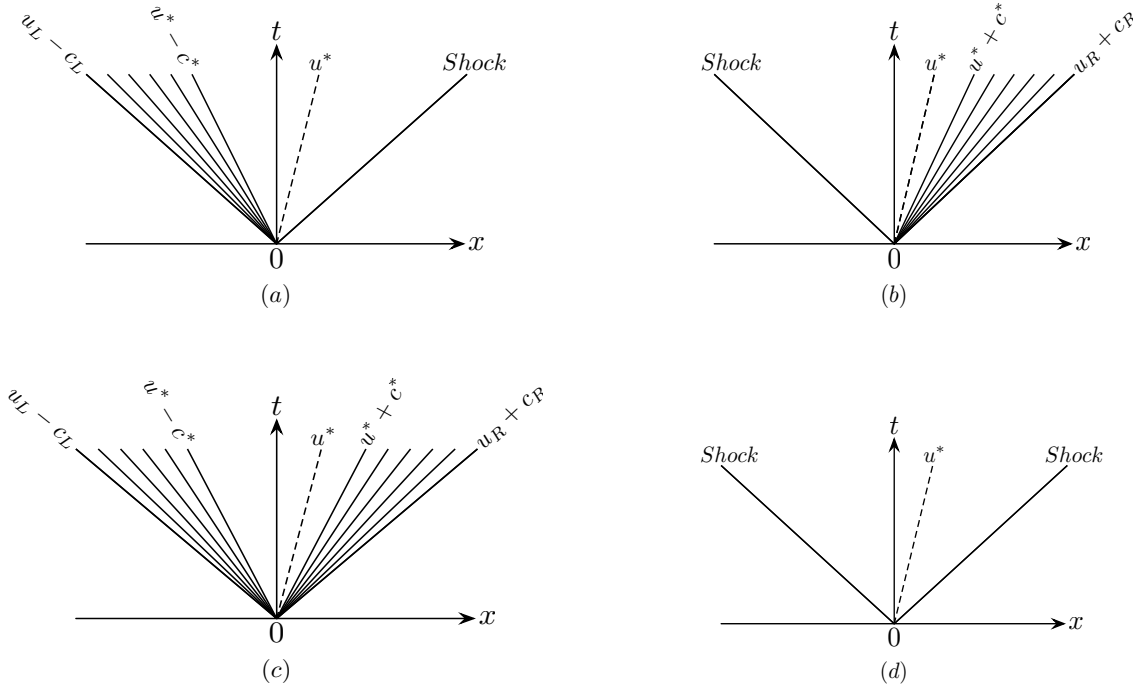


Figure 3.9 – Possible wave patterns in the solution of the Riemann problem. (a) Left rarefaction, centre contact, right shock; (b) left shock, centre contact, right rarefaction; (c) left rarefaction, centre contact, right rarefaction; and (d) left shock, centre contact, right shock.

artificial viscosity, which can introduce an unphysical amount of dissipation into the calculation. Unfortunately, some approximate Riemann solvers can be quite diffusive. There are higher-order schemes that can mitigate this problem. The simulations presented in chapters 6 and 7 use the second-order Monotone Upstream-centred Scheme for Conservation Laws (MUSCL) described in Toro (1999).

In finite volume methods with Riemann solvers, the Riemann problem is solved on cell interfaces to calculate the fluxes. The values in adjacent cells are known and there is a discontinuity at the cell interface. This is a natural description of a Riemann problem. In the SPH formulation, the Riemann problem is solved at the midpoint between the particle of interest a and each particle b in its support. The Riemann solutions are then interpolated with the kernel over the support to give the new value at particle a . That is, the SPH representation in (3.37) and (3.38) would no longer contain the values of the fluid variables at b , for example \mathbf{u}_b , ρ_b , and P_b ; they are replaced with the solutions to the Riemann problem u^* , ρ^* , and P^* . Furthermore, any values \mathbf{u}_a , ρ_a , and P_a that are used in the interpolation to ensure a symmetric derivative are also set to u^* , ρ^* , and P^* . Consequently, an expression such as $P_a + P_b$ in the original SPH representation would simply equal $2P^*$. Recall that the SPH representation in (3.37) and (3.38) are in non-conservative form. The equivalent expression to equation

(3.38) in conservative form in one dimension for simplicity is

$$\left\{ \begin{array}{l} \frac{\partial \rho_a}{\partial t} + \sum_b \frac{m_b}{\rho_b} [(\rho u)_b - (\rho u)_a] \nabla_a W_{ab} = 0 \\ \frac{\partial (\rho u)_a}{\partial t} + \sum_b \frac{m_b}{\rho_b} [(P + \rho u^2)_b + (P + \rho u^2)_a] \nabla_a W_{ab} = 0. \end{array} \right. \quad (3.59)$$

To obtain the SPH representation in (3.38), recall the identities in (3.34) and (3.35) were used with $\sigma = 1$. The result is a term with the derivative of a constant $-\rho u \nabla(1)$ which is equal to zero. This term will be left in to maintain symmetry but its sign will be switched to positive. This manipulation will allow the development of the SPH-ALE formulation shown later in (3.68) and also in Vila (1999). The SPH representation in conservative form with a Riemann solver then becomes

$$\left\{ \begin{array}{l} \frac{\partial \rho_a}{\partial t} + \sum_b \frac{m_b}{\rho_b} 2(\rho^* u^*) \nabla_a W_{ab} = 0 \\ \frac{\partial (\rho u)_a}{\partial t} + \sum_b \frac{m_b}{\rho_b} 2[P^* + \rho^*(u^*)^2] \nabla_a W_{ab} = 0, \end{array} \right. \quad (3.60)$$

where the quantities marked with a star are the solutions to the Riemann problem at the midpoint between particles a and b . Note that (3.59) and (3.60) are no longer in a Lagrangian frame of reference. Further modifications are made in the next section so that (3.60) can be expressed in a Lagrangian frame of reference if desired.

The fundamental difference between the methods described in sections 3.1 to 3.6 and the Riemann solvers in this section is that the SPH particles can no longer be thought of as a set of material fluid particles, but as control volumes exchanging fluxes. In the next section, the concept of a Riemann solver is applied to a special kind of SPH that has similarities to finite volume methods.

3.9 SPH-ALE

The methods presented in sections 3.1 to 3.6 relate to what is called classical SPH. This section describes a variation called SPH-ALE (Arbitrary Langrangian-Eulerian), where the particles in a simulation can move with the fluid in a Lagrangian frame of reference, or they can be fixed in an Eulerian frame of reference, or they can move with some other arbitrary transport velocity. An ALE description attempts to combine the advantages of both Eulerian and Lagrangian algorithms. In doing so, the ALE description enables the use of another boundary treatment that is well suited for complex geometries. The ALE formalism allows objects to move with an arbitrary transport

velocity, independent of the fluid velocity. This can be advantageous in simulations of fluid-solid interaction.

It is useful at this point to review some features of Eulerian and Lagrangian algorithms. Since the ALE description is not restricted to meshless particle methods, the following discussion attempts to generalize over grid and meshless techniques. Both solid and fluid continuum mechanics are considered. Let a material point be a localized region in the continuum containing information such as velocity, density, and pressure at a given time. Let a node be a point where the calculations are done. For grid-based methods, let the computational mesh connect the neighbouring nodes to form a grid. Figure 3.10 shows a visual representation of Lagrangian, Eulerian, and ALE algorithms.

Lagrangian algorithms have nodes that follow the material points during the motion. The main advantages are that the non-linear convective terms ($u \cdot \nabla$) vanish and that material interfaces are naturally tracked. For grid-based methods, the computational mesh connects the nodes and cannot handle large deformations without frequent re-meshing; therefore, grid-based Lagrangian approaches are more common in structural mechanics where the deformations are generally small. For meshless methods, large deformations are possible so Lagrangian algorithms can be used in a broader realm of continuum mechanics. The drawback is that large uncontrolled particle distortion can lead to reduced accuracy.

Eulerian algorithms have nodes that are fixed in space while the material points move with respect to the nodes. Large distortions in the continuum motion are handled easily at the cost of inaccurate description of material interfaces and inexact calculation of the non-linear convective terms.

ALE algorithms can have the nodes follow the material points in the Lagrangian way or they can be fixed in space in an Eulerian fashion, or, further still, they can move in some arbitrary way to suit to the specific application. This versatility allows for higher distortions than possible in Lagrangian grid-based methods, with higher accuracy than offered with an equivalent Eulerian description. The ALE description permits easier fluid-structure interaction in grid-based methods since solid-fluid interfaces are more easily defined. This could take the form of a Lagrangian description near the fluid-solid interface and an Eulerian description everywhere else in the fluid. For meshless methods, a solid can be moved at an arbitrary speed without sliding meshes or problems tracking the fluid-solid interface. The ALE description can allow for more accurate methods to calculate hydraulic forces on solid boundaries. In the SPH framework, this has been shown in Marongiu (2007).

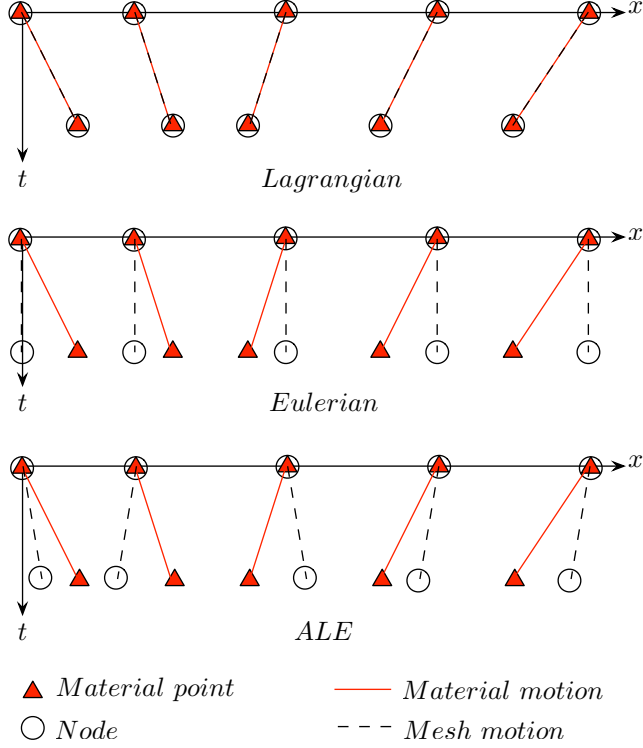


Figure 3.10 – Lagrangian, Eulerian, and ALE descriptions in one dimension. Adapted from Donea et al. (2004).

Consider the system of conservation laws in (3.49). Suppose we wish to view the evolution of a control volume with variables Φ in some arbitrary frame of reference moving at a velocity $\mathbf{u}_0 = (u_0, v_0, w_0)^T$. Equation (3.49) becomes

$$\left(\frac{\partial \Phi}{\partial t} + \mathbf{u}_0 \frac{\partial \Phi}{\partial \mathbf{x}} \right) + \left(\frac{\partial \mathbf{F}(\Phi)}{\partial \mathbf{x}} - \mathbf{u}_0 \frac{\partial \Phi}{\partial \mathbf{x}} \right) = 0. \quad (3.61)$$

Note the advection of Φ by \mathbf{u}_0 has merely been added and then subtracted from equation (3.49) without changing any of the physics. The first two terms can be written as a material derivative travelling at a velocity \mathbf{u}_0 and the second two as fluxes through a control volume moving with the same velocity \mathbf{u}_0 :

$$\frac{d_{\mathbf{u}_0} \Phi}{dt} + \frac{\partial}{\partial \mathbf{x}} (\mathbf{F}(\Phi) - \mathbf{u}_0 \otimes \Phi) = 0, \quad (3.62)$$

where \otimes denotes the outer product equivalent to the matrix multiplication of $\mathbf{u}_0 \Phi^T$, or in indicial notation, $u_{0,i} \Phi_j$. Equation (3.62) is equivalent to what is found in Vila (1999) and Marongiu et al. (2010), although they replace the material derivative travelling at \mathbf{u}_0 with what they call a transport operator $L_{\mathbf{u}_0}(\Phi)$, where

$$L_{\mathbf{u}_0}(\Phi) = \frac{d_{\mathbf{u}_0}\Phi}{dt} = \frac{\partial\Phi}{\partial t} + \mathbf{u}_0 \frac{\partial\Phi}{\partial\mathbf{x}}. \quad (3.63)$$

If (3.62) is written for the Euler equations, in one dimension for simplicity, then

$$\frac{\partial}{\partial t} \begin{bmatrix} \rho \\ \rho u \end{bmatrix} + u_0 \frac{\partial}{\partial x} \begin{bmatrix} \rho \\ \rho u \end{bmatrix} + \frac{\partial}{\partial x} \begin{bmatrix} \rho u - \rho u_0 \\ P + \rho u^2 - \rho u u_0 \end{bmatrix} = 0. \quad (3.64)$$

In this form, it is clear that for $u_0 = u$, the Lagrangian description in (3.25) is recovered and for $u_0 = 0$, we have the Eulerian description. This is true for multi-dimensional problems as well.

Vila (1999) introduced an SPH formalism with an ALE description. He further modified the classical SPH formalism by replacing the volume element in (3.3), $dV = \frac{m}{\rho}$ by a particle weight $dV = \omega$, where, for fluid particles, ω has units of volume in three dimensions, area in two dimensions, and length in one dimension. The idea is that the particles are transported at a velocity \mathbf{u}_0 and the weights are modified to compensate for any deformations of the velocity field; hence

$$\frac{d_{\mathbf{u}_0}\mathbf{x}_a}{dt} = \mathbf{u}_0(\mathbf{x}_a, t) \quad \text{and} \quad \frac{d_{\mathbf{u}_0,a}}{dt}(\omega_a) = (\nabla \cdot \mathbf{u}_0(\mathbf{x}_a, t))\omega_a, \quad (3.65)$$

where the shorthand $\mathbf{u}_{0,a} = \mathbf{u}_0(\mathbf{x}_a, t)$ is used for readability. To avoid adding artificial viscosity, a Riemann solver is used. Since the conservation laws are now transported at an arbitrary velocity, the solutions in section 3.8 must be modified to solve the *moving* Riemann problem where $\Phi^* = \Phi(\frac{x}{t}; \Phi_a, \Phi_b)$ becomes

$$\left\{ \begin{array}{l} \Phi^* = \Phi\left(\frac{x + X_0(t)}{t}; \Phi_a, \Phi_b\right) \\ X_0(t) = \int_0^t \mathbf{u}_0(x, \tau) \cdot \mathbf{n}_{ab} d\tau. \end{array} \right. \quad (3.66)$$

The particle approximation of (3.62) becomes

$$\frac{d_{\mathbf{u}_0,a}}{dt}(\omega_a \Phi_a) + \omega_a \sum_{b \in D_a} \omega_b 2(\mathbf{F}(\Phi^*) - \mathbf{u}_{0,ab} \otimes \Phi^*) \nabla_a W_{ab} = 0, \quad (3.67)$$

where $\mathbf{u}_{0,ab} = \mathbf{u}_0(\mathbf{x}_{ab}, t)$ and \mathbf{x}_{ab} is the position at the midpoint between particle a and b . The full solution in terms of the state variables is

$$\left\{ \begin{array}{l} \frac{d\mathbf{u}_{0,a}}{dt}(\mathbf{x}_a) = \mathbf{u}_{0,a} \\ \frac{d\mathbf{u}_{0,a}}{dt}(\omega_a) = \omega_a \sum_{b \in D_a} \omega_b (\mathbf{u}_{0,a} - \mathbf{u}_{0,b}) \nabla_a W_{ab} \\ \frac{d\mathbf{u}_{0,a}}{dt}(\omega_a \rho_a) + \omega_a \sum_{b \in D_a} \omega_b 2\rho^* (\mathbf{u}^* - \mathbf{u}_{0,ab}) \nabla_a W_{ab} = 0 \\ \frac{d\mathbf{u}_{0,a}}{dt}(\omega_a \rho_a \mathbf{u}_a) + \omega_a \sum_{b \in D_a} \omega_b 2 (\rho^* \mathbf{u}^* \otimes (\mathbf{u}^* - \mathbf{u}_{0,ab}) + P^*) \nabla_a W_{ab} = 0, \end{array} \right. \quad (3.68)$$

where $(\rho^*, \rho^* \mathbf{u}^*)^T = \Phi^*$ is the solution to the moving Riemann problem between particles a and b . Aside from the fact that the fluid particles can move at an arbitrary velocity, there are a few more subtle differences between this formalism and classical SPH. In classical SPH, each particle has a constant mass, whereas, the continuity equation in (3.68) shows that mass $m_a = \rho_a \omega_a$ changes with time. In fact, the particles in the SPH-ALE formalism exchange mass and momentum fluxes. Consequently, it is preferable to think of SPH-ALE particles not as small elements of fluid, but as control volumes that exchange momentum and mass between each other. While the convenient property of each particle having a constant mass is lost, (3.68) is based on conservation laws and ensures that mass is conserved globally over the set of calculation points. It was noted earlier that if the Euler equations were put in the form (3.62) with the transport velocity equal to the fluid velocity $\mathbf{u}_0 = \mathbf{u}$, the Lagrangian description in (3.25) is recovered. If the same procedure is done to (3.68) by setting $\mathbf{u}_0 = \mathbf{u}$, there are still convective fluxes present. The Riemann solver shifts the convective fluxes and pressure to naturally stabilize the scheme without the need for artificial viscosity. Since the ALE description can accommodate particles moving with the fluid as well as particles fixed in space, it may be more easily coupled with finite volume methods. This may lead to many interesting applications, for example, simulating Lagrangian SPH particles near a free-surface to capture its dynamic behaviour coupled with a fine Eulerian finite volume mesh near solid walls to capture boundary layer effects.

One of the motivations for developing an SPH-ALE formalism was to create another treatment for solid boundaries. Implementing accurate solid boundary treatments is challenging in SPH methods because particles near the boundary have truncated supports. Many SPH boundary treatments solve this problem by adding boundary particles outside the boundary so that the fluid particles near a wall no longer have

truncated supports. For complex geometries, there may be regions where boundary particles could not accurately describe the solid surface. This alternative method described in Marongiu (2007) calculates the pressure on every surface element that makes up the solid boundary. The pressure is calculated from the solution of a partial Riemann problem between each boundary element and the neighbouring fluid. The method stems from the integral approximation of spatial derivatives shown in (3.7) consisting of a volume integral over the support and a surface integral along its boundary. Most standard SPH methods ignore the surface integral and use methods described in section 3.6 to mitigate the problems associated with truncated supports. The method presented herein attempts to calculate this surface integral and therefore eliminates the need for particles outside solid boundaries. Recall that the SPH representation of a spatial derivative has the form

$$\left\langle \frac{\partial f(\mathbf{x})}{\partial \mathbf{x}} \right\rangle = \int_{\partial D} f(x') W(x - x', h) \cdot \mathbf{n} dS - \int_D f(\mathbf{x}') \frac{\partial W(\mathbf{x} - \mathbf{x}', h)}{\partial \mathbf{x}'} d\mathbf{x}'. \quad (3.69)$$

If the surface integral in (3.69) is included in the derivations presented in the previous sections, then the resulting SPH-ALE governing equations in (3.68) become

$$\left\{ \begin{array}{l} \frac{d\mathbf{u}_{0,a}}{dt}(\mathbf{x}_a) = \mathbf{u}_{0,a} \\ \frac{d\mathbf{u}_{0,a}}{dt}(\omega_a) = \omega_a \sum_{b \in D_a} \omega_b (\mathbf{u}_{0,a} - \mathbf{u}_{0,b}) \nabla_a W_{ab} + \dots \\ \qquad \qquad \qquad \omega_a \sum_{b \in \partial D_a} \omega_b^\partial (\mathbf{u}_{0,a} - \mathbf{u}_{0,b}) W_{ab} \cdot \mathbf{n}_b \\ \frac{d\mathbf{u}_{0,a}}{dt}(\omega_a \rho_a) + \omega_a \sum_{b \in D_a} \omega_b 2\rho^* (\mathbf{u}^* - \mathbf{u}_{0,ab}) \nabla_a W_{ab} + \dots \\ \qquad \qquad \qquad \omega_a \sum_{b \in \partial D_a} \omega_b^\partial 2\rho^* (\mathbf{u}^* - \mathbf{u}_{0,ab}) W_{ab} \cdot \mathbf{n}_b = 0 \\ \frac{d\mathbf{u}_{0,a}}{dt}(\omega_a \rho_a \mathbf{u}_a) + \omega_a \sum_{b \in D_a} \omega_b 2 (\rho^* \mathbf{u}^* \otimes (\mathbf{u}^* - \mathbf{u}_{0,ab}) + P^*) \nabla_a W_{ab} + \dots \\ \qquad \qquad \qquad \omega_a \sum_{b \in \partial D_a} \omega_b^\partial 2 (\rho^* \mathbf{u}^* \otimes (\mathbf{u}^* - \mathbf{u}_{0,ab}) + P^*) W_{ab} \cdot \mathbf{n}_b = 0, \end{array} \right. \quad (3.70)$$

where ω^∂ is the weight of the boundary element on $\partial\Omega$. The solid boundary is composed of a single layer of surface elements each with a weight ω^∂ and a unit vector \mathbf{n} pointing

into the problem domain, normal to the surface. Unlike the fluid weights, the boundary element weights have units of length and area in two and three-dimensional problems, respectively. From the momentum equation in (3.70), we can see that the pressure flux F^P exchanged between the boundary element a and the fluid particles b is

$$F_{a \rightarrow \Omega}^P = \omega_a^\partial \sum_{b \in D_a} \omega_b 2P^* W_{ab} \cdot \mathbf{n}_a. \quad (3.71)$$

The total pressure flux is also given by

$$F_{a \rightarrow \Omega}^P = \omega_a^\partial P_a \cdot \mathbf{n}_a. \quad (3.72)$$

Equating the two expressions for pressure flux gives

$$P_a = \sum_{b \in D_a} \omega_b 2P^* W_{ab}. \quad (3.73)$$

The result is that, in the continuous limit, the total force of the fluid on the boundary is equal to the pressure on each boundary element multiplied by its weight ω^∂ :

$$F_{\Omega \rightarrow \partial\Omega}^P = \sum_{b \in \partial\Omega} \omega_b^\partial P_b \cdot \mathbf{n}_b \approx \int_{\partial\Omega} P \cdot \mathbf{n} dS. \quad (3.74)$$

The value of P^* is the solution to the partial Riemann problem between the fluid and the boundary. The Riemann problem discussed in section 3.8 is composed of a left and right fluid state represented by an interface. The left and right states were located at SPH fluid particles and the interface was taken as the midpoint between the two particles. A partial Riemann problem consists of one single fluid state and a boundary condition. The main idea is that the influence of the boundary on the fluid is determined through the boundary fluxes located at the boundary surface. Therefore, the boundary surface plays a similar role to the interface between two fluid states. The partial Riemann problem is then defined by the fluid state and the boundary condition imposed on the boundary surface. Partial Riemann problems are discussed in detail in Dubois (2001). Partial Riemann problems related specifically to SPH-ALE are presented in Marongiu (2007); Leboeuf and Marongiu (2011).

The boundary treatment presented in this section calculates the force on the solid boundary by a partial Riemann problem that considers characteristics propagating from the fluid onto the boundary together with the imposed boundary condition. It eliminates the need for boundary particles outside the boundary surface and consequently allows for the use of complex geometries. Furthermore, the ALE description

makes the boundary treatment applicable to boundaries moving at an arbitrary velocity \mathbf{u}_0 . Numerical simulations using this boundary treatment have been in good agreement with laboratory experiments of water jets impacting Pelton buckets (Marongiu, 2007; Marongiu et al., 2010).

3.10 Summary

This chapter has presented the theory and the mathematical framework of the SPH method used to calculate the results in this thesis. It is useful at this point to distinguish between the *existing SPH code* and the *new developments*. For the remainder of this thesis, the *existing SPH code* will refer to the state of the numerical model used to calculate the results in this thesis before any of the present thesis work was done. All the SPH theory presented in this chapter had already been implemented in the existing SPH code. This numerical model has been validated with standard SPH benchmark tests outlined in section 2.1 and has enjoyed success in turbomachinery design. A detailed account of the implementation of the existing SPH code is in Marongiu (2007). The new developments focus on enabling the simulation of freely moving objects in a free-surface flow for river ice applications. The next chapter presents the theory and mathematical framework used to implement these new developments as part of this thesis work. They were achieved by including discrete element modelling capabilities within the existing SPH code to enable the simulation of freely moving solid objects subject to both hydrodynamic forces as well solid contact forces from collisions with other solids or boundaries.

Chapter 4

Discrete element method

The discrete element method (DEM) is a numerical technique for solving granular material problems. Its unique feature is that it explicitly considers each particle in the granular system and the interactions between them. Two types of DEM are discussed in this chapter: the hard-sphere and soft-sphere models. They are introduced in section 2.2.

In the hard-sphere model, the particles follow piece-wise linear trajectories between inelastic collisions. The interactions between particles are assumed to be instantaneous, where momentum is exchanged by impulsive forces. The dissipation of energy from the inelastic collisions is quantified by a coefficient of restitution, specifying the ratio of recoil velocity to approach velocity. For lower density systems, the hard-sphere model is considerably less computationally demanding than the soft-sphere model. For closely packed particles or low coefficients of restitution, the collisions can lead to large decreases in kinetic energy, such that the relative velocities of colliding particles approach zero. In this limit, the particles tend to be in resting contact with their neighbours. The hard-sphere model depends on the assumption that particles experience instantaneous collisions. For particles in resting contact, this assumption is clearly violated and the hard-sphere model is no longer valid.

In the soft-sphere model, particles are allowed to overlap slightly and the contact forces are calculated through a contact force relationship. The particles are still considered to be rigid in the sense that their deformation shape is not considered. The particle-particle contacts can last extended durations and, in dense systems, force networks can develop between clusters of contacting particles. The soft-sphere model can successfully simulate granular flow in the quasi-static and static regimes, where the hard-sphere model breaks down. This is achieved at the cost of a longer computation time. The contact forces are calculated based on the amount of overlap between particles, which depends on the particles' material properties. These are commonly described in terms of a spring stiffness, friction angle, and damping constant.

Both hard-sphere and soft-sphere models have their own strengths, weaknesses, and applicability. One approach may outperform the other, depending on the characteristics of the granular flow. Table 4.1 compares the two models. Since the collisions in a hard-sphere model are assumed to be instantaneous, from a computer simulation viewpoint, this means that collisions occur over a single time-step. In contrast, soft-sphere models must have time-steps that are significantly smaller than the particle

collision duration. Consequently, hard-sphere models are generally less computationally demanding than soft-sphere models. The faster hard-sphere approach does not come without a cost. Characteristics such as friction and cohesion are more easily described by particle interactions that have finite durations. As a result, these phenomena can be more readily incorporated into a soft-sphere model. Since soft-sphere models often characterize granular material in terms of a spring stiffness, friction angle, and damping constant, particles of different sizes generally need different spring stiffnesses, which can complicate the analysis. Most soft-sphere models approximate the particle shape as perfect spheres in three dimensions or circular discs in two dimensions. This greatly simplifies the contact detection, contact history, and the particle interaction calculations since all collisions are central collisions where the normal force acts through the body's centre of mass. Since the collisions are instantaneous in a hard-sphere model, there is no contact history and the particle interaction calculations are generally simpler than in a soft-sphere model. As such, arbitrarily shaped particles are more easily simulated using a hard-sphere model. Particles with large aspect ratios may preferentially flow in a specific orientation; therefore, approximating them as spheres may lead to erroneous results. In terms of the overall goal of simulating river ice processes, most ice floes are thin in the vertical direction so they flow preferentially in one orientation, which is more easily modelled by a hard-sphere model. On the other hand, the collision process described by the hard-sphere model is through momentum exchange so that lasting contact forces between particles cannot be calculated. As a result, the information concerning lasting contact forces of ice floes on structures or force networks between a dense aggregate of ice floes is more easily calculated from a soft-sphere model. Since there are elements of both the hard-sphere and soft-sphere models that could prove useful in modelling river ice flows, both are considered in this chapter.

Table 4.1 – Comparison between hard- and soft-sphere models. The symbols indicate GOOD (😊), NORMAL (😐), and NOT SUITABLE (😢).

	Hard-sphere	Soft-sphere
Computing efficiency	😊	😐
Multiple particle shapes and sizes	😊	😐
Incorporation of friction and cohesive forces	😐	😊
Dense systems	😢	😊
Calculation of contact forces	😢	😊

The DEM offers an alternative to the common approach of simulating granular ma-

terials as a continuum. In the continuum mechanics framework, the granular material is considered to be a continuous medium and the relative motion between individual particles is not considered. The analysis relies on complicated constitutive relationships to describe how the stress is generated. As discussed in section 2.2, granular material behaves very differently depending on the flow regime. Consequently, even sophisticated constitutive relationships can have limits of applicability that could break down for a granular flow that changes flow regimes. In the DEM, even simple contact models have been able to capture the overall behaviour of granular flow and in many cases, they agree well with laboratory experiments and theory (O’Sullivan, 2011). The DEM can also handle large deformations more easily than common continuum approaches for granular material, for example, finite element methods.

It should be noted that the DEM differs substantially from SPH. In the SPH method, the fluid is described in a continuum mechanics framework. The SPH particles are nothing more than interpolation points whose motion is dictated by the governing physical equations and the kernel. The interpolation occurs over a set of particles in the kernel support. The SPH particles in the kernel support are not necessarily in *contact* with the fluid particle of interest. In contrast, the DEM is a discrete method, where forces are calculated between particles in contact with each other. In the DEM, there is no interpolation and no need for a kernel.

This chapter first presents, in sections 4.1 to 4.5, theory on rigid body dynamics, which applies to both hard- and soft-sphere models. Both models use the same equations of motion and the same theory pertaining to coordinate systems, rotations, and moments of inertia. Where the two approaches differ is in the contact force schemes, which are outlined in sections 4.6 and 4.7. In this chapter, the term rigid body will be used for solid objects of any shape, including spheres, where their shape may be important but is not necessarily so. The term particle will refer to solid objects idealized by spheres in three dimensions or circular discs in two dimensions, such that their shape is no longer considered important. The exception to these definitions will only be made when the name of each DEM approach is used. That is, the hard-sphere model may refer to the simulation of either rigid bodies or particles, similarly for the soft-sphere model. Since it is considerably more difficult to simulate arbitrarily shaped solids with the soft-sphere model, this case is not considered. In section 4.6, the hard-sphere model is presented for simulating any arbitrarily shaped solid. In section 4.7, the soft-sphere model is presented for simulating spheres in three dimensions and circular shaped discs in two dimensions. Both these approaches are used to calculate the results found in chapters 6 and 7.

4.1 Position and rotation of a rigid body

An unconstrained rigid body in three dimensions has six degrees of freedom: three translational, and three rotational. The translation is usually described by a vector pointing from a fixed origin to the centre of mass of the rigid body. The rotation can be described in several ways including rotation matrices, Euler angles, and quaternions, each with their own strengths and weaknesses, discussed further in Dam et al. (1998). In this thesis, a rotation matrix is used to describe the orientation of rigid bodies.

4.2 Coordinate systems

Two coordinate systems are used herein to describe the motion of a rigid body. The first is a fixed coordinate system with its origin at an arbitrary point in space. This coordinate system will be called the *world frame*. The second moves with the rigid body over time with its origin at the centre of mass of the solid. This coordinate system will be called the *body frame*. Both are shown in figure 4.1. In the following sections, all quantities are given in the world frame unless explicitly stated.

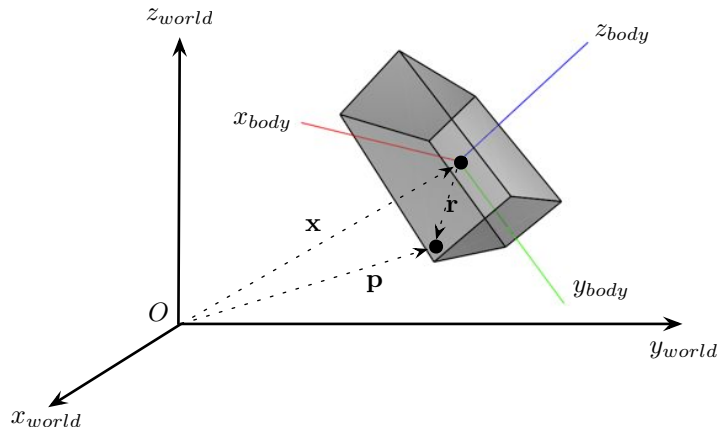


Figure 4.1 – Coordinate system in the world frame and the body frame. The position vector of the centre of mass of the rigid body is \mathbf{x} , \mathbf{p} is the position vector of a point on the rigid body’s surface, and \mathbf{r} is a vector pointing from the centre of mass \mathbf{x} to a point on the solid’s surface \mathbf{p} .

4.3 Rotation matrices

One of the most common ways to represent the rotation of a rigid body is by a rotation matrix. Any rotation in three dimensions can be described by a 3×3 orthogonal matrix \mathbf{R} , having the following properties:

- the inverse of the rotation matrix is equal to its transpose: $\mathbf{R}^{-1} = \mathbf{R}^T$,
- the transpose of the rotation matrix multiplied by the rotation matrix equals the identity matrix: $\mathbf{R}^T \mathbf{R} = \mathbf{I}$, and

- the determinant of the rotation matrix is equal to unity: $\det |\mathbf{R}| = 1$.

The rotation matrix describing the rotation of a rigid body through an arbitrary angle $\boldsymbol{\theta} = (\gamma, \beta, \alpha)^T$ can be expressed as the product of rotation matrices defining rotations about the x , y , and z axis denoted by $\mathbf{R}_x(\gamma)$, $\mathbf{R}_y(\beta)$, and $\mathbf{R}_z(\alpha)$, respectively. The rotation matrices about a specified axis are given by

$$\mathbf{R}_x = \begin{bmatrix} 1 & 0 & 0 \\ 0 & \cos\gamma & -\sin\gamma \\ 0 & \sin\gamma & \cos\gamma \end{bmatrix} \quad \mathbf{R}_y = \begin{bmatrix} \cos\beta & 0 & \sin\beta \\ 0 & 1 & 0 \\ -\sin\beta & 0 & \cos\beta \end{bmatrix} \quad \mathbf{R}_z = \begin{bmatrix} \cos\alpha & -\sin\alpha & 0 \\ \sin\alpha & \cos\alpha & 0 \\ 0 & 0 & 1 \end{bmatrix} \quad (4.1)$$

and the rotation matrix about an arbitrary angle is

$$\mathbf{R} = \mathbf{R}_z \mathbf{R}_y \mathbf{R}_x. \quad (4.2)$$

The angles γ , β , and α about the x , y , and z axes are measured as positive in the counterclockwise direction, following the right-hand rule. It can also be useful to define a rotation matrix \mathbf{H} in terms of a single angle ψ rotated about an arbitrary axis defined by the unit vector $\mathbf{h} = (h_x, h_y, h_z)^T$. The rotation matrix is then

$$\mathbf{H} = \begin{bmatrix} c + qh_x^2 & qh_xh_y - h_zs & qh_xh_z + h_ys \\ qh_xh_y + h_zs & c + qh_y^2 & qh_yh_z - h_xs \\ qh_zh_x - h_ys & qh_zh_y + h_xs & c + qh_z^2 \end{bmatrix}, \quad (4.3)$$

where

$$c = \cos(\psi), \quad q = 1 - c, \text{ and } s = \sin(\psi). \quad (4.4)$$

Rotation matrices provide a relatively easy way to parameterize the rotation of any unconstrained arbitrarily shaped rigid body. A rotation matrix is also a useful tool to transform a vector from one coordinate system to another. Rotation matrices, however, use nine elements to define only three degrees of freedom. From a computer programming perspective, this uses more memory storage than is really necessary. Furthermore, rotation matrices are prone to numerical drift. In other words, as a simulation progresses, a rotation matrix may lose its orthogonality due to numerical error. To ensure the rotation matrix remains orthogonal, it is required to re-normalize the matrix, which is a time consuming process.

Another method to describe rotations is to use a quaternion, which is a type of four-element vector containing a rotation angle about an axis defined by a unit vector.

Quaternions experience less numerical drift than rotation matrices and use less memory storage. It is becoming widely accepted in literature that this method is the preferred method to use to model non-spherical bodies in three dimensions (O’Sullivan, 2011). Nevertheless, if the right precautions are taken, rotation matrices can be acceptable.

4.4 Moments of inertia

The mass moment of inertia is a measure of resistance to rotation. In other words, it describes how difficult it is to spin an object about an axis. In two dimensions, the axis of rotation cannot change. For example, if the two-dimensional object is in the xy -plane, the rotation is fixed to the z axis. In this case, the moment of inertia is a single value, and the rotation can be described by a single angle. Since the axis of rotation of a three-dimensional object can be in any direction, the situation is more complex. In three dimensions, the moment of inertia is represented by a symmetric tensor called the inertia tensor \mathbf{I} , given by

$$\mathbf{I} = \begin{bmatrix} I_{xx} & -I_{xy} & -I_{xz} \\ -I_{yx} & I_{yy} & -I_{yz} \\ -I_{zx} & -I_{zy} & I_{zz} \end{bmatrix}, \quad (4.5)$$

and the elements of the tensor are

$$\mathbf{I} = \begin{bmatrix} \int y^2 dm + \int z^2 dm & -\int xy dm & -\int xz dm \\ -\int yx dm & \int x^2 dm + \int z^2 dm & -\int yz dm \\ -\int zx dm & -\int zy dm & \int x^2 dm + \int y^2 dm \end{bmatrix}, \quad (4.6)$$

where dm is the mass differential. The integral is evaluated using a local Cartesian coordinate system with its origin at the centre of mass of the body, but with its axes aligned with the world frame. Note the difference between this new coordinate system and the body frame where the axes rotate with the solid and are not necessarily aligned with the world frame. Also note that the inertia tensor is symmetric; therefore, it can be diagonalized by an orthogonal matrix. In other words, for any inertia tensor \mathbf{I} , it is possible to find a rotated coordinate system for which \mathbf{I} is a diagonal matrix, even for arbitrarily shaped rigid bodies. In the body frame, the inertia tensor is constant since the coordinate axes move with the body. In the world frame, the inertia tensor changes as the body rotates. It can be shown, as in Baraff (2001), that the two inertia tensors are related by

$$\mathbf{I}_{world} = \mathbf{R}\mathbf{I}_{body}\mathbf{R}^T. \quad (4.7)$$

This relationship is useful since we ultimately want the quantities in the world frame. They are of interest because they are in the inertial frame of reference where Newton's Laws are valid.

4.5 Equations of motion

A rigid body's motion is governed by the forces and torques acting on it. Specific to this thesis, these could include hydraulic forces, gravitational forces, and any contact forces and torques with other rigid bodies. The hydraulic forces are calculated by integrating the pressure on each boundary element of the solid over its surface area. The pressure is calculated through a solution to the moving partial Riemann problem described in section 3.9. The gravitational force is the body's mass multiplied by the acceleration due to gravity. There are different methods for calculating contact forces, presented later in this chapter. The forces acting on a solid a can be divided into contact forces, hydraulic forces and external forces giving

$$m_a \frac{d^2 \mathbf{x}_a}{dt^2} = \mathbf{F}_{contact,a} + \mathbf{F}_{hydraulic,a} + \mathbf{F}_{external,a}, \quad (4.8)$$

where \mathbf{x}_a is the solid's centre of mass, $\mathbf{F}_{contact,a}$ includes the forces on a from any solids in contact with a , $\mathbf{F}_{hydraulic,a}$ includes the hydraulic forces calculated from the moving Riemann problem on the boundary elements associated with solid a , and $\mathbf{F}_{external,a}$ includes any gravitational forces or other external forces acting on the solid. The torque $\boldsymbol{\tau}$ on solid a is calculated by

$$\boldsymbol{\tau}_a = \sum_{k \in \partial\Omega_a} (\mathbf{p}_k - \mathbf{x}_a) \times \mathbf{F}_k, \quad (4.9)$$

where \mathbf{p}_k is the position vector of a boundary element k on the surface $\partial\Omega_a$ of solid a and \mathbf{F}_k is any surface force including contact forces and hydraulic forces acting on solid a at \mathbf{p}_k .

The change in linear and angular momentum with time can be related to force and torque by

$$\mathbf{F} = \frac{d\mathbf{P}}{dt}, \quad (4.10)$$

and

$$\boldsymbol{\tau} = \frac{d\mathbf{L}}{dt}, \quad (4.11)$$

respectively, where \mathbf{P} is linear momentum equal to $m\mathbf{v}$, \mathbf{v} is the linear velocity at the

solid's centre of mass, and \mathbf{L} is angular momentum. Note that \mathbf{L} is related to the inertia tensor \mathbf{I} and angular velocity $\boldsymbol{\omega}$ by

$$\mathbf{L} = \mathbf{I}\boldsymbol{\omega}. \quad (4.12)$$

Let us define a state vector $\Phi(t)$ of quantities describing a rigid body's position \mathbf{x} , orientation $\boldsymbol{\theta}$, linear momentum \mathbf{P} and angular momentum \mathbf{L} . We can define a vector $\Gamma(t)$ of variables \mathbf{v} , $\boldsymbol{\omega}$, \mathbf{F} , and $\boldsymbol{\tau}$ which are related to the state vector by

$$\frac{d}{dt} \begin{bmatrix} \mathbf{x} \\ \boldsymbol{\theta} \\ \mathbf{P} \\ \mathbf{L} \end{bmatrix} = \begin{bmatrix} \mathbf{v} \\ \boldsymbol{\omega} \\ \mathbf{F} \\ \boldsymbol{\tau} \end{bmatrix}. \quad (4.13)$$

The time integration is done using an explicit time integration scheme as described in section 3.5. For a first-order forward Euler time integration, the state variables at time $n + 1$ are given by

$$\Phi^{(n+1)} = \Phi^{(n)} + \delta t \Gamma^{(n)}. \quad (4.14)$$

After the state vector has been advanced in time, auxiliary variables at time $n + 1$ can be calculated using the new values in the state vector without any time-stepping:

$$\left\{ \begin{array}{l} \mathbf{v} = \frac{\mathbf{P}}{m} \\ \mathbf{I} = \mathbf{R}\mathbf{I}_{body}\mathbf{R}^T \\ \boldsymbol{\omega} = \mathbf{I}^{-1}\mathbf{L}. \end{array} \right. \quad (4.15)$$

Both the hard- and soft-sphere models follow these equations of motion. For particles shaped as spheres and circles, the analysis is simplified since any collision that occurs is a central collision where the normal force acts through the particles centre of mass. Furthermore, as a sphere rotates, its inertia tensor remains constant because its resistance to rotation is the same for any axis of rotation through its centre of mass. The next section describes how the motion of colliding solids is determined for the hard-sphere model.

4.6 Hard-sphere model

At low concentrations and high shear rates, the motion of a granular material is dominated by nearly instantaneous inelastic collisions where particles exchange momentum through impulsive forces. The physics of granular flow and computer simula-

tion methods for granular material are discussed in more detail in section 2.2. As the concentration of granular material decreases, fewer and fewer collisions occur and the fluid phase then dominates the motion. The flow can no longer be called a granular flow. In the limit of low concentrations, there will only be one solid particle and its motion will be determined entirely by the fluid in addition to any other external forces such as gravity. Non-spherical particles with high aspect ratios may have preferential orientations in a flow and may not be accurately modelled by spheres. In this case, arbitrarily shaped solids can be modelled through principles of rigid body dynamics.

This section describes how the principle of impulse can be used to model instantaneous inelastic collisions between rigid bodies of arbitrary shapes. Note that the methodology described in this section applies to rapidly flowing granular material or to flows dominated by the fluid phase where only a few solids are present.

When two bodies collide, momentum is exchanged giving rise to a change in velocity. We are assuming the bodies have infinite elastic moduli so that collisions are instantaneous. Therefore, the change in velocity is also instantaneous. We can define impulse \mathbf{J} as

$$\mathbf{J} = \mathbf{F}\Delta t, \quad (4.16)$$

where Δt represents a very small increment in time over which the collision occurs. Impulse is a vector quantity with units of momentum. Let us denote the scalar j as the magnitude of the impulse such that $J = j \cdot \mathbf{n}$ where \mathbf{n} is a unit vector in the direction normal to the impulse. The change in velocity of a solid, subject to an impulse can be written as

$$\Delta\mathbf{v} = \frac{\mathbf{J}}{m} = \frac{j \cdot \mathbf{n}}{m}. \quad (4.17)$$

Since torque is defined as $\boldsymbol{\tau} = \mathbf{r} \times \mathbf{F}$, where \mathbf{r} is a vector from the solid's centre of mass \mathbf{x} to a point on its surface \mathbf{p} , then the change in angular momentum from an impulse is

$$\Delta\mathbf{L} = \mathbf{r} \times \mathbf{J}. \quad (4.18)$$

The velocity $\dot{\mathbf{p}}$ of a point located on a solid's surface has both a translational and a rotational component and can be expressed as

$$\dot{\mathbf{p}} = \mathbf{v} + \boldsymbol{\omega} \times \mathbf{r}. \quad (4.19)$$

Consider two solids a and b in a collision. Let \mathbf{n} be the unit vector normal to contact surface of solid b , exerting an impulse on a . The velocity of solid a relative to b in the direction \mathbf{n} becomes

$$\mathbf{v}_{rel} = (\dot{\mathbf{p}}_a - \dot{\mathbf{p}}_b) \cdot \mathbf{n}. \quad (4.20)$$

The coefficient of restitution ϵ is the ratio of the recoil velocity to approach velocity of colliding solids and is given by

$$\epsilon = -\frac{\mathbf{v}_{rel}^+}{\mathbf{v}_{rel}^-}, \quad (4.21)$$

where the superscripts $(-)$ and $(+)$ indicate the value of the quantity before and after the collision, respectively. The translational and rotational velocities after the collision are then

$$\mathbf{v}^+ = \mathbf{v}^- + \Delta\mathbf{v} = \mathbf{v}^- + \frac{j \cdot \mathbf{n}}{m} \quad (4.22)$$

and

$$\boldsymbol{\omega}^+ = \boldsymbol{\omega}^- + \Delta\boldsymbol{\omega} = \boldsymbol{\omega}^- + \mathbf{I}^{-1}\Delta\mathbf{L} = \boldsymbol{\omega}^- + \mathbf{I}^{-1}(\mathbf{r} \times \mathbf{J}). \quad (4.23)$$

Combining (4.22) and (4.23), for solid a , (4.19) can be written as

$$\dot{\mathbf{p}}_a^+ = (\mathbf{v}_a^- + \frac{j \cdot \mathbf{n}}{m_a}) + [\boldsymbol{\omega}_a^- + \mathbf{I}_a^{-1}(\mathbf{r}_a \times j \cdot \mathbf{n})] \times \mathbf{r}_a, \quad (4.24)$$

which can be rearranged to give

$$\dot{\mathbf{p}}_a^+ = \dot{\mathbf{p}}_a^- + j \left[\frac{\mathbf{n}}{m_a} + \mathbf{I}_a^{-1}(\mathbf{r}_a \times \mathbf{n}) \times \mathbf{r}_a \right]. \quad (4.25)$$

For solid b , an opposite impulse $-j \cdot \mathbf{n}$ is exerted; therefore,

$$\dot{\mathbf{p}}_b^+ = \dot{\mathbf{p}}_b^- - j \left[\frac{\mathbf{n}}{m_b} + \mathbf{I}_b^{-1}(\mathbf{r}_b \times \mathbf{n}) \times \mathbf{r}_b \right]. \quad (4.26)$$

Subtracting (4.25) from (4.26) gives

$$(\dot{\mathbf{p}}_a^+ - \dot{\mathbf{p}}_b^+) = (\dot{\mathbf{p}}_a^- - \dot{\mathbf{p}}_b^-) + j \left[\frac{\mathbf{n}}{m_a} + \frac{\mathbf{n}}{m_b} + \mathbf{I}_a^{-1}(\mathbf{r}_a \times \mathbf{n}) \times \mathbf{r}_a + \mathbf{I}_b^{-1}(\mathbf{r}_b \times \mathbf{n}) \times \mathbf{r}_b \right]. \quad (4.27)$$

Multiplying through by \mathbf{n} while noting the definition of \mathbf{v}_{rel} in (4.20) yields

$$\mathbf{v}_{rel}^+ = \mathbf{v}_{rel}^- + j \left[\frac{1}{m_a} + \frac{1}{m_b} + \mathbf{n} \cdot (\mathbf{I}_a^{-1} (\mathbf{r}_a \times \mathbf{n}) \times \mathbf{r}_a + \mathbf{I}_b^{-1} (\mathbf{r}_b \times \mathbf{n}) \times \mathbf{r}_b) \right]. \quad (4.28)$$

Finally, solving for j gives

$$j = \frac{-(1+\epsilon) \mathbf{v}_{rel}^-}{\left[\frac{1}{m_a} + \frac{1}{m_b} + \mathbf{n} \cdot (\mathbf{I}_a^{-1} (\mathbf{r}_a \times \mathbf{n}) \times \mathbf{r}_a + \mathbf{I}_b^{-1} (\mathbf{r}_b \times \mathbf{n}) \times \mathbf{r}_b) \right]}. \quad (4.29)$$

The result is an expression for the impulse, based solely on known, pre-collision variables. The instantaneous momentum exchange between solid bodies is then solved. Nevertheless, in a numerical simulation, time is discretized into finite increments. Consequently, there is no such thing as an instantaneous collision. The smallest increment in time is one time-step. Therefore, (4.29) represents the impulse over one time-step. The resulting change in translational and rotational velocity is calculated according to (4.22) and (4.23), respectively. These new velocities are used to calculate the hydraulic forces and torques on the solid for the following time-step.

Note that the solid contact forces between colliding solids are never explicitly calculated. This should not be surprising since in a hard-sphere model, solids are never in contact with each other for any extended duration. In fact, the longest two particles are in contact with each other is one time-step. Imagine the simple case of a spherical ball dropped from a height H with no initial velocity onto a flat surface. The ball will hit the surface and rise to some height less than H according to its coefficient of restitution. The ball will continue to hit the surface and rebound to a lesser and lesser height. Only at infinity will the ball actually be in static equilibrium with the plate such that lasting contact between the two solids is established. At this point, however, the assumptions of the hard-sphere model break down since the solids are no longer experiencing instantaneous collisions. It is for this reason, that contact forces are not calculated in the hard-sphere model. In the next section a method is described for calculating contact forces and force networks between particles.

4.7 Soft-sphere model

In a soft-sphere model, colliding solids are allowed to overlap slightly and the contact forces are calculated from the deformation history by a contact force relationship. Unlike the hard-sphere model, solids may remain in contact for extended durations, and one solid can be in contact with several others concurrently. In the last section, we saw the complexity of describing an instantaneous frictionless collision between two arbitrarily shaped solids. The complexity increases substantially if friction is con-

sidered and also if the bodies are allowed to stay in contact for extended durations. For this reason, the soft-sphere model described herein applies to circular discs in two dimensions and spheres in three dimensions, rather than arbitrarily shaped solids.

Soft-sphere models differ from each other depending on their contact force scheme. The approaches to calculate contact forces between solids vary in applicability and complexity and are discussed in Schafer et al. (1996). Many soft-sphere contact models stem from the linear spring and dashpot model proposed by Cundall and Strack (1979). This section presents the DEM used to calculate the results in chapters 6 and 7 based on the model by Cundall and Strack (1979) and presented herein using most of the same notation as in Van der Hoef et al. (2006). In this model, the normal force $\mathbf{F}_{ab,n}$ between particle a and b can be calculated by

$$\mathbf{F}_{ab,n} = -k_n \delta_n \cdot \mathbf{n}_{ab} - \eta_n \mathbf{v}_{ab,n}, \quad (4.30)$$

where k_n is the normal spring stiffness, \mathbf{n}_{ab} is the unit vector pointing from the centre of mass of a to the centre of mass of b , η_n is the normal damping coefficient, and $\mathbf{v}_{ab,n}$ is the normal relative velocity. The overlap δ_n is given by

$$\delta_n = (R_a + R_b) - |\mathbf{x}_a - \mathbf{x}_b|, \quad (4.31)$$

where R_a and R_b are the particle radii, and \mathbf{x}_a and \mathbf{x}_b are the particle centres of mass. Figure 4.2 shows the notation used in this section in a problem definition sketch. Figure 4.3 shows a graphical representation of a spring and dashpot model.

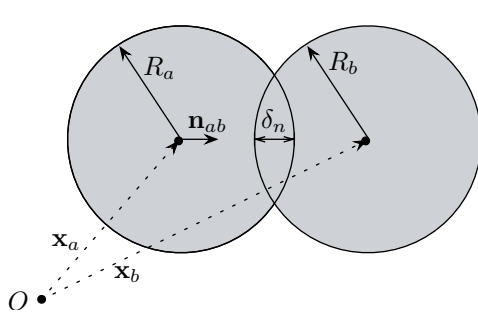


Figure 4.2 – Soft-sphere model nomenclature.

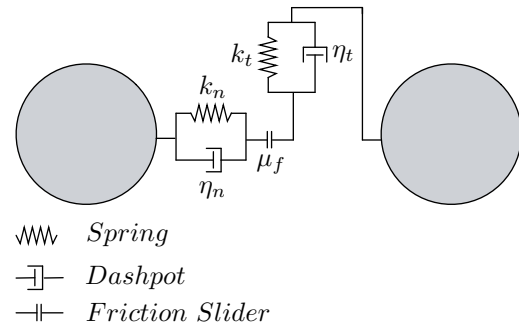


Figure 4.3 – Soft-sphere model with spring and dashpot system.

The tangential component of the contact force \mathbf{F}_t is calculated by a Coulomb friction law using a coefficient of friction μ_f . It can be expressed as

$$\mathbf{F}_{ab,t} = \begin{cases} -k_t \delta_t \cdot \mathbf{t}_{ab} - \eta_t \mathbf{v}_{ab,t} & \text{for } |\mathbf{F}_{ab,t}| < \mu_f |\mathbf{F}_{ab,n}| \\ -\mu_f |\mathbf{F}_{ab,n}| \cdot \mathbf{t}_{ab} & \text{for } |\mathbf{F}_{ab,t}| > \mu_f |\mathbf{F}_{ab,n}|, \end{cases} \quad (4.32)$$

where k_t , δ_t , and η_t are the tangential spring stiffness, tangential overlap, and tangential damping coefficient, respectively. The tangential relative velocity $\mathbf{v}_{ab,t}$ and the tangential unit vector \mathbf{t}_{ab} are

$$\mathbf{v}_{ab,t} = \mathbf{v}_{ab} - \mathbf{v}_{ab,n} \quad \text{and} \quad \mathbf{t}_{ab} = \frac{\mathbf{v}_{ab,t}}{|\mathbf{v}_{ab,t}|}. \quad (4.33)$$

The calculation of δ_t is not as straightforward as for δ_n . To calculate the tangential displacement, let us consider an initial tangential displacement δ_{t_0} at time t_0 , then a tangential displacement δ_t at some time $t > t_0$ could be found by integrating the relative tangential velocity in time:

$$\delta_t \cdot \mathbf{t}_{ab} = \delta_{t_0} \cdot \mathbf{t}_{0,ab} + \int_{t_0}^t \mathbf{v}_{ab,t} dt. \quad (4.34)$$

Equation (4.34) is only valid for two-dimensional problems. In three dimensions, the calculation becomes more complicated because the tangential displacement is no longer restricted to a single plane and neither is the normal unit vector. Consequently, the tangential displacement δ_{t_0} must be rotated to the new contact plane at time t before calculating the new tangential displacement. In three dimensions, the tangential displacement becomes

$$\delta_t \cdot \mathbf{t}_{ab} = \delta_{t_0} \cdot \mathbf{t}_{0,ab} \cdot \mathbf{H} + \int_{t_0}^t \mathbf{v}_{ab,t} dt, \quad (4.35)$$

where \mathbf{H} is the rotation matrix defined by an axis of rotation \mathbf{h} and a single angle ψ rotated about \mathbf{h} as in (4.3). Since the tangential relative velocity is always perpendicular to the unit normal vector, the axis of rotation and the angle are

$$\mathbf{h} = \frac{\mathbf{n}_{ab} \times \mathbf{n}_{0,ab}}{|\mathbf{n}_{ab} \times \mathbf{n}_{0,ab}|} \quad \text{and} \quad \psi = \arcsin(|\mathbf{n}_{ab} \times \mathbf{n}_{0,ab}|), \quad (4.36)$$

where $\mathbf{n}_{0,ab}$ is the normal vector at time t_0 and \mathbf{n}_{ab} is the normal vector at time t . By developing an expression for δ_t , it is now possible to calculate $\mathbf{F}_{ab,t}$ from (4.32).

In the soft-sphere model, the equations of motion in (4.8) and (4.9) depend on five material parameters: k_n , k_t , η_n , η_t , and μ_f . To see how they are related, it is

instructive to look at the following case. Consider the time evolution of the overlap in the normal direction between particle a and b , described by a spring and dashpot model. The overlap δ_n is given by the initial value problem

$$\begin{cases} m_{eff}\ddot{\delta}_n = -k_n\delta_n - \eta_n\dot{\delta}_n \\ \delta_n(0) = 0 \\ \dot{\delta}_n(0) = v_0, \end{cases} \quad (4.37)$$

where m_{eff} is related to the mass of the colliding solids by

$$\frac{1}{m_{eff}} = \frac{1}{m_a} + \frac{1}{m_b}, \quad (4.38)$$

and v_0 is the magnitude of the relative velocity between solid a and b in the normal direction. Equation (4.37) is a well-known second-order ordinary differential equation with constant coefficients. For the given initial conditions, the solution to (4.37) is

$$\delta_n(t) = \frac{v_0}{\Omega} \exp(-\Psi t) \sin(\Omega t), \quad (4.39)$$

where

$$\Omega = \sqrt{\Omega_0^2 - \Psi^2}, \quad \Omega_0 = \sqrt{\frac{k_n}{m_{eff}}}, \text{ and } \Psi = \frac{\eta_n}{2m_{eff}}. \quad (4.40)$$

Let the duration of contact between two solids be denoted by t_c and the initial time of contact be at $t = 0$. At $t = t_c$, there is no overlap between solids; therefore, $\delta_n(t_c) = 0$. From (4.39), The contact time is

$$t_c = \frac{\pi}{\Omega}, \quad (4.41)$$

and the relative velocity after contact is

$$\dot{\delta}_n(t_c) = -v_0 \exp(-\Psi t_c). \quad (4.42)$$

The coefficient of restitution, specifying the ratio of recoil to approach velocity becomes

$$\epsilon = -\frac{\dot{\delta}_n(t_{contact})}{\dot{\delta}_n(0)} = \exp\left(-\frac{\pi\Psi}{\Omega}\right). \quad (4.43)$$

Expanding Ψ and Ω in terms of the material properties in (4.40) and solving for η_n gives an expression relating the damping term η_n to the coefficient of restitution ϵ :

$$\eta_n = -\frac{2\ln(\epsilon)\sqrt{m_{eff}k_n}}{\sqrt{\pi^2 + \ln^2(\epsilon)}}. \quad (4.44)$$

The contact time t_c can also be expressed in terms of the material properties in (4.40), giving

$$t_c = \sqrt{\frac{\pi^2 + \ln^2(\epsilon)}{k_n/m_{eff}}}. \quad (4.45)$$

A similar expression to (4.37) can be formulated for the displacement in the tangential direction. For a tangential coefficient of restitution ϵ_t equal to ϵ , the tangential damping coefficient becomes

$$\eta_t = -\frac{2\ln(\epsilon)\sqrt{m'_{eff}k_t}}{\sqrt{\pi^2 + \ln^2(\epsilon)}}, \quad (4.46)$$

where $k_t = \frac{2}{7}k_n$. The value of $\frac{2}{7}$ causes the normal and tangential springs to react on similar time scales (Luding, 1998), since in the tangential direction both translational and rotational momentum is considered. The contact time calculated in (4.45) must be equal to the one calculated based on the tangential material properties k_t and m'_{eff} . From the denominator of (4.45), it is clear that $\frac{k_n}{m_{eff}} = \frac{k_t}{m'_{eff}}$; therefore, $m'_{eff} = \frac{2}{7}m_{eff}$. Recall that in soft-sphere models, the contacts must be evaluated over 40 to 50 time-steps to produce accurate results (Walton, 1993). From (4.45), a condition can be imposed on the time-step to ensure this requirement. The maximum allowable time-step Δt is then

$$\Delta t = \frac{t_c}{50} = \frac{1}{50}\sqrt{\frac{\pi^2 + \ln^2(\epsilon)}{k_n/m_{eff}}}. \quad (4.47)$$

In this section, the time-step will be denoted by Δt instead of δt to avoid confusion with the displacement δ . For a numerical simulation containing both SPH and soft DEM particles, the maximum allowable time-step is the minimum of the three conditions in (3.45) related to SPH particles and the condition in (4.47).

The linear and angular motion of the particles can now be calculated in terms of the five material parameters: k_n , k_t , η_n , η_t , and μ_f . Since the damping coefficients have been expressed in terms of ϵ , m_{eff} , and k_n ; and k_t can be related to k_n , we can reduce the number of user defined parameters to three: k_n , μ_f , and ϵ . The other parameters k_t , η_n , and η_t can be calculated from k_n , μ_f , and ϵ . While the parameters μ_f and ϵ are chosen to represent the simulated material, the spring stiffness k_n is often selected

to speed up computation time without producing erroneous results. From (4.47), it is clear that large values of k_n give small time-steps. Although k_n can be related to the physical properties of the simulated material, for example, Young's modulus, this value often produces prohibitively small time-steps. Instead, k_n is chosen so that the contact time remains over 40 to 50 time-steps while the maximum overlap is less than 1% of the particle diameter. The maximum displacement can be calculated from (4.39). In terms of the time-step, it is favourable to have a small k_n but in terms of the maximum overlap, k_n must be sufficiently large. The speed of the DEM simulation depends on the selection of k_n in a similar way that an SPH simulation depends on the selection of the numerical speed of sound c_0 .

4.8 Summary

This chapter has presented theory and mathematical framework of the DEM. Both hard- and soft-sphere models have been implemented in the existing SPH code to enable the simulation of freely moving objects subject to hydraulic and contact forces. In the next chapter, theory related to ice jams is presented. Similarities will be drawn between the DEM discussed in this chapter and certain ice jam processes.

Chapter 5

Ice Jams

This chapter presents theory for river ice jam analysis that is relevant to the concepts used for the numerical simulations presented in chapter 7. First, theory predicting ice block stability and under-turning is presented. The chapter concludes with a basic analysis on calculating forces and jam thicknesses of a static ice jam. While static ice jam theory is not explicitly used in this thesis, it shows the parameters that have been studied over the years and the approach that has been taken. To take advantage of the previous field and laboratory studies that have parameterized physical quantities characteristic of ice jams, the writer has made efforts to formulate the present numerical model using many of the same physical quantities.

5.1 Floating block stability

Two primary types of submergence are considered in this section: vertical submergence and under-turning, as shown in figure 2.4. Section 2.3 presents the background on this topic. Two approximate analytical solutions are presented herein: (1) by Pariset and Hausser (1961) based on the assumption that the incipient motion of a floating block coincides with the top upstream edge of it submerging without rotation; and (2) by Ashton (1974) based on a balance between the hydrostatic righting moment under the block, buoyancy, and the under-turning moment due to flow acceleration under the block. There have been improvements to these approximate analytical solutions (Daly and Axelson, 1990; Dow Ambtman et al., 2011b); however, for simplicity and clarity, only the original approximate analytical solutions are presented.

The problem under consideration involves flow in an open-channel with a floating block pushed against a stationary cover, both with the same thickness and density, as shown in figure 2.3. A dimensional analysis suggests that the critical velocity V , for submergence of the floating block has the following functional dependencies:

$$V = f(t_i, b, L, H, \rho_w, \rho_i, g), \quad (5.1)$$

where the floating block is of length L , thickness t_i , width b ; the depth of flow upstream of the block is H ; the density of water and the block are ρ_w and ρ_i , respectively; and the gravitational acceleration is g . Note, in this chapter and in subsequent discussions on ice, the subscript i stands for *ice* and is not an index for tensor notation. In non-dimensional form, (5.1) becomes

$$\frac{V}{\sqrt{gH}} = f \left(\frac{t_i}{H}, \frac{t_i}{L}, \frac{L}{b}, \frac{\rho_i}{\rho_w} \right). \quad (5.2)$$

Ashton (1974) presented his result in terms of a densimetric Froude number based on block thickness and density. Through dimensional analysis, Ashton reasoned that instability is likely to occur when the pressure forces exceed the buoyant forces and the most significant parameter is a ratio of these two forces. By taking the pressure forces to scale as $\rho_w V^2 L b$ and the buoyant forces to scale as $(\rho_w - \rho_i) g t_i L b$, then the ratio of the two is

$$\frac{\rho_w V^2}{g t_i (\rho_w - \rho_i)}. \quad (5.3)$$

By re-arranging and taking the square root, (5.3) can be expressed as a densimetric Froude number

$$F_D = \frac{V}{\sqrt{g t_i \left(1 - \frac{\rho_i}{\rho_w} \right)}}. \quad (5.4)$$

This result reduces the functional relation in (5.2) to

$$F_D = f \left(\frac{t_i}{H}, \frac{t_i}{L} \right). \quad (5.5)$$

Both approximate solutions by Pariset and Hausser (1961) and Ashton (1974) start with Bernoulli's equation and assume no head loss between the upstream section and under the floating block. The following discussion shows how Pariset and Hausser (1961) developed a stability criterion for floating ice blocks. The velocity under the block can be related to the upstream velocity by

$$H + \frac{V^2}{2g} = H_u + \frac{V_u^2}{2g} + t_s. \quad (5.6)$$

To prevent incoming water spilling over the top of the blocks,

$$H + \frac{V^2}{2g} \leq H_u + t_i. \quad (5.7)$$

From (5.6) and (5.7), it follows that

$$\frac{V_u^2}{2g} \leq t_i - t_s. \quad (5.8)$$

The blocks are assumed to be floating; therefore, $t_s = \frac{\rho_i}{\rho_w} t_i$, and (5.8) becomes

$$\frac{V_u^2}{2g} \leq t_i \left(1 - \frac{\rho_i}{\rho_w}\right). \quad (5.9)$$

Assuming a constant width, continuity requires that $VH = V_u H_u$, and combining this with (5.7) gives

$$V = V_u \left(1 + \frac{V^2}{2gH} - \frac{t_i}{H}\right). \quad (5.10)$$

For small Froude numbers, $Fr = \frac{V}{\sqrt{gH}}$, which are characteristic of most natural river reaches, the second term on the right-hand side of (5.10) can be neglected. By substituting the result in (5.9) for V_u , (5.10) becomes

$$V = \sqrt{2gt_i \left(1 - \frac{\rho_i}{\rho_w}\right)} \left(1 - \frac{t_i}{H}\right). \quad (5.11)$$

The critical upstream velocity in (5.11) can be expressed in terms of the densimetric Froude number defined in (5.4), which gives

$$F_D = \sqrt{2} \left(1 - \frac{t_i}{H}\right). \quad (5.12)$$

The result is an expression for the critical upstream velocity as a function of block thickness, flow depth, and density. Any upstream velocity exceeding this critical value, according to the analysis, should cause instability of the floating block.

Ashton (1974) showed that under-turning occurs at a critical velocity lower than predicted by Pariset and Hausser (1961). The reason being, Pariset's analysis assumed the approaching block reached the no spill condition by vertical submergence rather than by rotation. By summing the moments about point A in figure 2.3,

$$\frac{\rho_i g t_i L^2}{2} + \left(\frac{\rho_w V_u^2}{2} - \frac{\rho_w V^2}{2}\right) = \frac{\rho_w g t_s L^2}{2} + \frac{\rho_w g L^2}{2} \frac{2}{3} L \sin \alpha. \quad (5.13)$$

Dividing through by $\frac{\rho_w g t_i L^2}{2}$ gives

$$\frac{V_u^2}{2gt_i} - \frac{V^2}{2gt_i} = -\frac{\rho_i}{\rho_w} + \frac{t_s}{t_i} + \frac{2L \sin \alpha}{3t_i}. \quad (5.14)$$

By assuming incipient motion occurs when the top upstream corner of the block submerges, then

$$L \sin \alpha = t_i - t_s - \frac{V_u^2}{2g}. \quad (5.15)$$

Substituting the right-hand side of (5.15) into (5.14) and assuming that $t_s = t_i \frac{\rho_i}{\rho_w}$, (5.14) can be re-written as

$$\frac{5V_u^2}{6gt_i} - \frac{V^2}{2gt_i} = \frac{2}{3} \left(1 - \frac{\rho_i}{\rho_w} \right). \quad (5.16)$$

By continuity, $V = V_u \left(1 - \frac{t_i}{H} \right)$, which leads to the critical upstream velocity expressed in terms of the densimetric Froude number:

$$F_D = \frac{V}{\sqrt{gt_i \left(1 - \frac{\rho_i}{\rho_w} \right)}} = \frac{2 \left(1 - \frac{t_i}{H} \right)}{\sqrt{5 - 3 \left(1 - \frac{t_i}{H} \right)^2}}. \quad (5.17)$$

In both these analyses, there are several simplifying assumptions. In both cases, the analysis starts off with Bernoulli's equation which assumes steady, incompressible, inviscid, irrotational flow where energy is conserved along a streamline. The flow is assumed to be uniform upstream of the floating block and below it. Pariet and Hausser (1961) assumed that a floating block will vertically submerge until the no spill condition is satisfied, then the block will be entrained by the flow by under-turning or further vertical submergence. Ashton (1974) showed that the under-turning moment required for the block to reach instability could arrive at velocities less than for vertical submergence. Neither study considered the pressure exerted on the upstream face of the floating block, nor the dynamic pressures that may arise from the acceleration of flow underneath the floating block. The simulations presented in chapter 7 show a floating block under-turning under various flow conditions. The dynamic pressure on all the block faces are calculated and there are no assumptions about the steadiness or uniformity of the flow.

5.2 Steady state and equilibrium ice jams

In this section, a simple one-dimensional steady ice jam analysis is presented. While the analysis below may seem rudimentary, it has formed the foundation for many of the current ice jam models. In computer simulations of ice jams, many of the validation cases compare their results to the simplified analysis presented below.

Consider a steady flow in a straight channel. Let T be the streamwise force per unit width of channel B at a location x along the length of channel starting at the leading edge of the ice jam. The driving forces considered are the shear on the underside of the ice cover $\tau_i = \rho_w g R_i S$ and the downslope weight component of the ice $w_i = \rho_i g S t_i$, where R_i is the hydraulic radius of the ice cover and S is the channel slope. These forces are opposed by the bank resistance. Summing the forces on the ice cover gives

$$B \frac{dT}{dx} = B (\tau_i + w_i) - 2k_0 k_1 T \quad (5.18)$$

where k_0 is the coefficient of lateral thrust (ratio of lateral stress to longitudinal stress) equal to $(1 - \sin\phi)$, ϕ is the angle of internal friction, and k_1 is the coefficient of friction equal to $\mu_f = \tan\phi$. The first term on the right-hand side represents the driving forces and the second term represents the bank resistance, where the coefficient 2 indicates that the jam is resisted from both riverbanks. If the thrust at the leading edge has a value of T_0 , then the first order ordinary differential equation in (5.18) has the solution

$$T = T_0 + \left\{ \frac{B(\tau_i + w_i)}{2k_0 k_1} - T_0 \right\} \left[1 - \exp \left(-\frac{2k_0 k_1}{B} x \right) \right]. \quad (5.19)$$

Taking the limit as x goes to infinity gives

$$T_\infty = \frac{B(\tau_i + w_i)}{2k_0 k_1}. \quad (5.20)$$

Pariset et al. (1966) used (5.20) to distinguish between wide and narrow channel jams. For $T_0 > T_\infty$, the jam is a narrow channel jam. The thrust will decrease in the downstream direction with the maximum at the leading edge. Hence, no internal collapse of the jam can occur. For $T_0 < T_\infty$, the jam is a wide channel jam. The thrust increases to a maximum as x goes to infinity. For a wide jam on the verge of collapsing, the asymptotic value in (5.20) is equal to the compressive strength of the jam:

$$(\sigma_x)_{max} = k_2 \rho_i \left(1 - \frac{\rho_i}{\rho_w} \right) \frac{gt_i}{2}, \quad (5.21)$$

where k_2 is the passive earth pressure coefficient given by $\tan^2 \left(\frac{\pi}{4} + \frac{\phi}{2} \right)$, or equivalently $\frac{1+\sin\phi}{1-\sin\phi}$. The result in (5.18) contains several simplifying assumptions. The obvious one is that the river width B is constant. It has also been implicitly assumed that the jam thickness t_i is independent of x and that the flow depth under the jam is constant. From the discussions in section 2.3, we know that this is not true, especially in the case of thickened jams. For simplicity, many other parameters such as ice porosity and cohesion are not included in this analysis.

If the ice thickness t_i is now considered as a function of x , then (5.18) becomes

$$\frac{d(\sigma_x t_i)}{dx} = (\tau_i + w_i) - \frac{2k_0 k_1}{B} (\sigma_x t_i). \quad (5.22)$$

If the initial jam thickness is zero and if we neglect the weight of the jam w_i , the

differential equation has the solution:

$$\sigma_x t_i = \left(\frac{B\tau_i}{2k_0 k_1} \right) \left(1 - \exp \left(-\frac{2k_0 k_1}{B} x \right) \right). \quad (5.23)$$

Finally solving for t_i and setting the compressive strength equal to the right-hand side of 5.21 leads to

$$t_i = \left(\frac{B\tau_i}{k_0 k_1 k_2 \rho_i g \left(1 - \frac{\rho_i}{\rho_w} \right)} \right)^{\frac{1}{2}} \left(1 - \exp \left(-\frac{2k_0 k_1}{B} x \right) \right)^{\frac{1}{2}}. \quad (5.24)$$

Note that $k_0 k_1 k_2 = \tan\phi (1 + \sin\phi)$ and $k_0 k_1 = (1 - \sin\phi) \tan\phi$. The result is a jam thickness profile starting at the leading edge and continuing downstream until the jam reaches an equilibrium thickness. This analysis has been used as a validation test case in numerical studies such as Shen et al. (2000). If the weight of the jam is considered, the solution to (5.22) is more complicated. This equation can, however, be written in terms of flow depth under the jam h and slope of the water surface S_w . If the discharge per unit width q is determined from

$$q = h \sqrt{\frac{4}{f_0} gh S}, \quad (5.25)$$

then (5.22) becomes

$$\frac{dt_s}{dx} = \beta_1 \left[S_w + \beta_2 \frac{f_0 q^2}{4gh^2 t_s} \right] - \beta_3 \frac{t_s}{B}, \quad (5.26)$$

where

$$\beta_1 = \frac{\frac{\rho_i}{\rho_w}}{k_2 \left(1 - \frac{\rho_i}{\rho_w} \right)}, \quad \beta_2 = \frac{f_i}{2f_0}, \quad \beta_3 = k_0 k_1, \quad \text{and} \quad f_0 = \frac{f_i + f_b}{2}, \quad (5.27)$$

and f_i , f_b , and f_0 denote ice, channel bed, and composite friction factors, respectively. Equation (5.26) can be solved numerically, given a specified discharge, flow depth and roughness. For equilibrium conditions, that is, when t_s does not change with x , (5.26) can be solved algebraically to give an equilibrium jam thickness:

$$\frac{t_s^{eq}}{S_0 B} = \frac{\frac{\rho_i}{\rho_w}}{2k_0 k_1 k_2 \left(1 - \frac{\rho_i}{\rho_w} \right)} \left\{ 1 + \sqrt{1 + 2 \frac{f_i}{f_0} k_0 k_1 k_2 \frac{1 - \frac{\rho_i}{\rho_w}}{\frac{\rho_i}{\rho_w}} \frac{h}{S_0 B}} \right\}, \quad (5.28)$$

where the superscript eq indicates equilibrium thickness, S_0 is the slope of the channel bed, which is equal to the slope of the water surface for uniform flow conditions. Equa-

tion (5.26) is similar to one of the fundamental governing equations in the numerical model RIVJAM (Beltaos, 1993), developed at the Canadian National Water Research Institute.

Numerical models such as RIVJAM and others mentioned in section 2.3 have had success predicting jam thicknesses and water levels. The computational results from these models have, in many cases, been in good agreement with field observations over long river reaches. The models, however, have many simplifying assumptions discussed in more detail in section 2.3. Existing ice jam models often rely on depth averaged approximations, such as the shallow water equations. The aim of the present study is to examine the dynamic effects associated with ice jams, in cases where depth averaged approximations may break down.

5.3 Summary

In this chapter, theory of floating ice block stability and steady ice jams was presented. The approximate analytical solutions for floating ice blocks are compared with numerical simulations in chapter 7. The theory on steady ice jams is presented to show how many of the numerical models are currently formulated and to highlight some of their strengths and weaknesses. Chapter 7 also presents simulations showing ice floes accumulating at an obstruction.

Chapter 6

Application and validation of simulations with freely moving solid objects

In this chapter, both the hard- and soft-sphere discrete element methods are implemented into the existing SPH framework. In order to validate the new developments, a few simple simulations are presented. Initially, simulations are run without a fluid phase so that the particle interactions of the solids can be observed without the effect of hydraulic forces. Afterwards, a fluid is introduced to evaluate the motion of the solids due to interactions with both the fluid and other solids.

Each DEM technique is evaluated separately with simulations that test their respective contact force schemes. Since the hard-sphere model is based on instantaneous exchanges of momentum between colliding solids, the validation is made through a comparison of the computational results to simple analytical solutions for instantaneous collisions with different coefficients of restitution.

Compared to the hard-sphere model, the soft-sphere model can be applied to a broader range of flow regimes, from rapid granular flow to granular material in static equilibrium. As a result, the validation test case was chosen so that the granular material experiences this range of flow regimes. In the test case, the granular material initially falls under the force of gravity onto a flat surface to form a pile. The granular material is initially rapidly flowing and finishes in static equilibrium, where the particles form a force network that transmits its bulk weight onto the supporting surface. The computational results are compared to the predicted shape of the pile surfaces given the different friction angles and also the expected value of the bulk weight that is transmitted from the particles onto the supporting surface. The final height and the horizontal distance the piles spread are compared to empirical relationships based on laboratory experiments of the collapse of granular columns.

After the DEM techniques are evaluated in the absence of hydraulic forces, a fluid is added to the simulation to assess the solid motion due to the fluid flow. The effects of dynamic forces, hydrostatic forces, and buoyancy are tested. The computational results are compared to laboratory experiments as well as to approximate analytical solutions. Finally, a three-dimensional simulation is presented demonstrating the behaviour of multiple solids with six degrees of freedom subject to both hydraulic and contact forces.

In all the simulations presented herein, the modelled fluid is water with a reference

density $\rho_0 = 1000 \text{ kg/m}^3$. For each simulation, the key parameters are listed. These include the geometry of the system, the number of solids in the simulation, the number of SPH particles in the simulation, the discretization size Δx of the SPH particles, and the material properties of the solids, such as solid density ρ_s , coefficient of restitution ϵ , and coefficient of friction $\mu_f = \tan\phi$. Recall that the fluid medium is made up of SPH particles as are the solids. Each solid is discretized into a set of SPH boundary particles that describes its overall shape. The pressure acting on the solid is integrated over the SPH boundary particles to determine the total hydraulic force on the solid. The number of particles quoted in this chapter refers to the total number of SPH particles in the simulation, including both fluid particles and boundary particles. This quantity represents the number of calculation points in the simulation.

6.1 Hard-sphere model

The hard-sphere model is based on instantaneous exchanges of momentum between colliding solids. Two simulations were run as validation test cases. In the first, two identical spheres experience a central collision and exchange momentum. In the second, a single sphere is dropped onto a level surface and rebounds to a given height according to its coefficient of restitution. The validation cases presented in this section are similar to those in Wei (2006).

6.1.1 Central collision between two solids

In this simulation, two identical spheres experience a central collision. One sphere has an initial velocity v_a^- and approaches the other, which is initially at rest. Gravity and all other external forces are ignored. The pre- and post-collision velocities are calculated in the numerical simulation and compared to the analytical solution based on the principle of impulse. The collision is assumed to be frictionless. Three collision types are considered: (a) purely elastic $\epsilon = 1$, (b) purely plastic $\epsilon = 0$, and (c) partially elastic $\epsilon = 0.5$. The purpose of this numerical simulation is to verify that the momentum exchange between two colliding solids agrees with the theory of frictionless collisions based on the principle of impulse.

The problem domain contains two spheres initially separated by one sphere-radius. Sphere a approaches sphere b at a velocity of 1 m/s and sphere b is initially at rest. The geometry of the system and the relevant simulation parameters are shown in figure 6.1.

The post-collision velocities for each sphere can be calculated from their initial velocities and the coefficient of restitution. Since the spheres are identical, their masses do not appear in the calculation. The equations of motion are

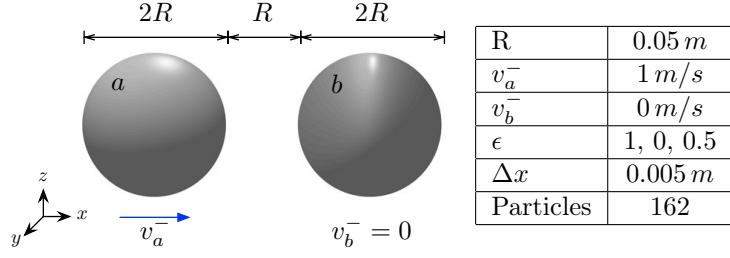


Figure 6.1 – Central collision between two solids: numerical setup.

$$\begin{cases} v_a^+ = \frac{1}{2}(1 - \epsilon)v_a^- + \frac{1}{2}(1 + \epsilon)v_b^- \\ v_b^+ = \frac{1}{2}(1 + \epsilon)v_a^- + \frac{1}{2}(1 - \epsilon)v_b^- . \end{cases} \quad (6.1)$$

Figure 6.2 shows the velocities of both spheres along the direction of the collision for case (a), (b), and (c). For the purely elastic collision, sphere a stops immediately after the collision and sphere b continues with the initial velocity of sphere a . In the purely plastic case, the two spheres stick together and continue to the right with half the initial velocity of sphere a . For the partially elastic collision, sphere a continues to the right at a slower rate than sphere b . Table 6.1 compares the pre- and post-collision velocities of the simulation to the analytical solution. The computational results are in good agreement with the analytical solution. The slight differences between the analytical solution and the computational results may be caused by the discretization size of the spheres. That is, the point of contact between the two spheres may lie between neighbouring boundary elements making up the sphere surfaces. In this case, the true direction of the impulse is slightly different from the calculated direction, which leads to a small velocity introduced in the direction tangent to the collision. This small velocity may partly explain the slight under-prediction of post-collision velocities observed in the results.

Table 6.1 – Central collision between two solids: comparison of computational results to theory. All quantities are in units of [m/s].

Sphere	Purely Elastic $\epsilon = 1$		Purely Plastic $\epsilon = 0$		Partially Elastic $\epsilon = 0.5$	
	Analytical	Numerical	Analytical	Numerical	Analytical	Numerical
a	0	0.005	0.5	0.498	0.25	0.254
b	1	0.995	0.5	0.499	0.75	0.745

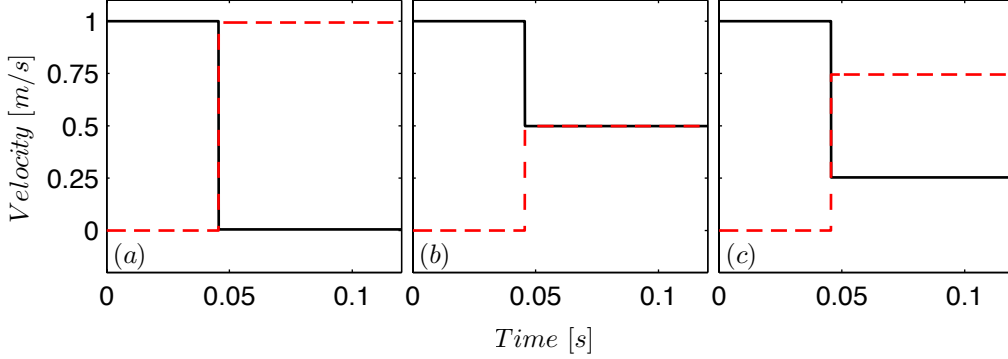


Figure 6.2 – Central collision between two solids: computational results. Velocity as a function of time for three coefficients of restitution: (a) $\epsilon = 1$, (b) $\epsilon = 0$, and (c) $\epsilon = 0.5$. The solid black line represents sphere a and the dashed red line represents sphere b .

6.1.2 Solid dropping onto a level surface

In this simulation, a sphere is dropped under the influence of gravity onto a level surface. It rebounds to a given height according to its coefficient of restitution. The sphere is allowed to rebound many times to observe the successive decreases in rebound height due to dissipation of energy from the collision with the surface. The purpose of this simulation is to verify that the momentum exchange between a solid and a flat boundary agrees with theory based on the principle of impulse and also to see if the motion of the solid subject to a gravitational force is accurate.

The problem domain contains one sphere whose bottom is 0.5 m above a level flat surface on the xy -plane, as shown in figure 6.3. The sphere is dropped and falls under the force of gravity until it contacts the level surface. It then rebounds to a maximum height less than the original height according to its coefficient of restitution. The height of the solid over time is compared to the analytical solution.

For a solid dropped from a height H_0 at a time t_0 , the rebound height H_n at time t_n after n bounces is given by

$$\begin{cases} H_n = \epsilon^{2n} H_0 \\ t_n = \sqrt{\frac{2H_0}{g}} \left(-1 - \epsilon^n + 2 \sum_{i=0}^n \epsilon^i \right) \end{cases} \quad (6.2)$$

Figure 6.4 compares the height of the bouncing solid as a function of time to the analytical solution in (6.2). The rebound height and timing agrees very well with the analytical solution. It is only near the very end of the simulation where the computational results start to deviate from the theory. This is not surprising because near the end of the simulation, the solid is approaching its inelastic limit where the

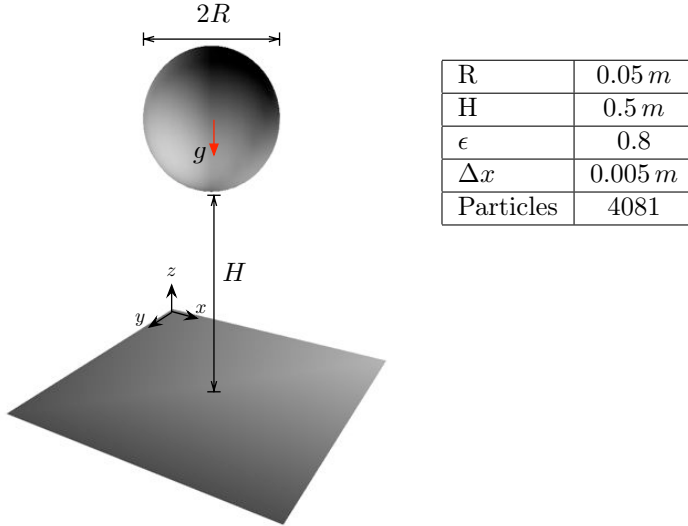


Figure 6.3 – Solid dropping onto a level surface: numerical setup.

hard-sphere model is no longer valid. That is, almost all the kinetic energy of the solid has been dissipated such that it is approaching resting contact with the level surface. The formulation of the hard-sphere model does not allow for resting contact; therefore, the hard-sphere model approaches the limit of its applicability. Furthermore, the computational results only start to deviate from the analytical solution once the rebound height is quite small. In fact, the deviation from the analytical solution starts when the rebound height is roughly the same size as the discretization size Δx of the sphere and the level surface. It is, therefore, understandable that there are small differences from the analytical solution for these small rebound heights.

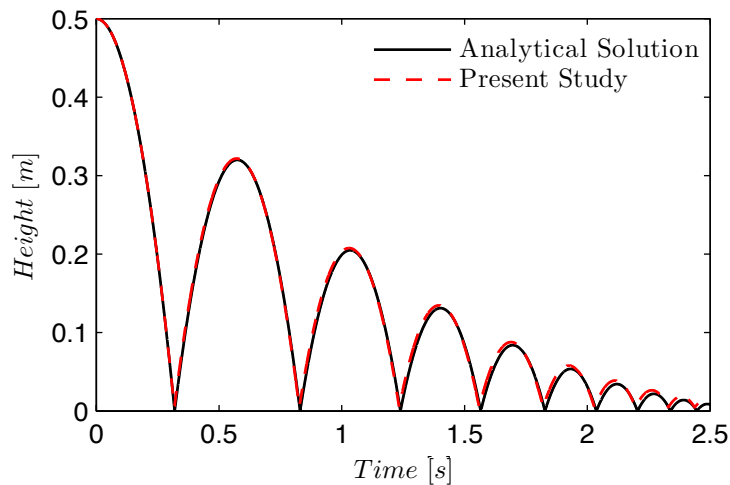


Figure 6.4 – Solid dropping onto a level surface: computational results. The figure shows the height of the solid above the level surface as a function of time.

6.2 Soft-sphere method

The soft-sphere model allows particles to be in contact with each other for extended durations and to develop force networks in a granular material. It can model a broader range of granular flow regimes than the hard-sphere model at the cost of higher computation times. The validation test case was chosen to demonstrate the range of granular flow regimes from a rapidly flowing regime to a static granular material. This section describes the simulation of a collapse of a granular column onto a horizontal plane.

6.2.1 Collapse of a granular column onto a horizontal plane

The collapse of a granular column onto a horizontal plane has been simulated in both two and three dimensions. The purpose of the simulation is (1) to observe the range of granular flow regimes, from rapidly flowing to static, and (2) to determine, once the flow comes to rest and forms a pile, if the force network between particles accurately transmits the bulk weight of the pile to the horizontal plane.

Recent experiments by Lube et al. (2004) and Lajeunesse et al. (2004) on the collapse of granular columns have generated significant interest and motivation for subsequent experimental (Balmforth and Kerswell, 2005; Lube et al., 2005), theoretical (Balmforth and Kerswell, 2005; Larrieu et al., 2006), and computational studies (Staron and Hinch, 2005; Zenit, 2005). The original experiments studied the collapse of a suddenly released axisymmetric column of granular material onto a horizontal plane. They analyzed the results in terms of run-out distance r_∞ and the height of the final deposition h_∞ , as shown in figure 6.5. They relate these quantities to the aspect ratio a of the initial height h_0 to the radius of the column r_0 through scaling laws. They found that the run-out distance and the height of the final deposit are strongly dependant on the aspect ratio. Table 6.2 summarizes the findings from various authors. They include findings from laboratory experiments of both axisymmetric (Lajeunesse et al., 2004; Lube et al., 2004) and two-dimensional granular collapses (Lube et al., 2005; Balmforth and Kerswell, 2005) as well as two-dimensional computational results (Staron and Hinch, 2005).

The dynamics of a granular collapse can be divided into two regimes, depending on the initial aspect ratio a . In the first regime, the granular column is shallow and the value of a is small. When the column is suddenly released, the grains near the edges start to fall. The motion propagates from the edges inwards until a slope develops along which material slides down and eventually stabilizes. In this regime, only the grains near the edges of the column participate in the flow, while the column's central

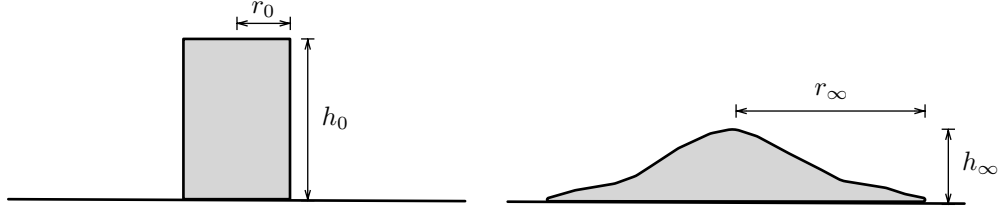


Figure 6.5 – Geometry of the initial column and final pile in a granular collapse.

Table 6.2 – Granular collapse: comparison of scaling laws.

	$\frac{r_\infty - r_0}{r_0} =$	$\frac{h_\infty}{r_0} =$
Lube et al. (2004)	$\begin{cases} 1.24a, & a < 1.7 \\ 1.6a^{0.5}, & a > 1.7 \end{cases}$	$\begin{cases} a, & a < 1.7 \\ 0.88a^{\frac{1}{6}}, & a > 1.7 \end{cases}$
Lajeunesse et al. (2004)	$\begin{cases} \frac{1}{2\mu_f} \left(a + \sqrt{4\mu_f^2 - \frac{a^2}{3}} \right) a, & a < 0.74 \\ 2a^{0.5}, & a > 0.74 \end{cases}$	$\begin{cases} a, & a < 0.74 \\ 0.74, & a > 0.74 \end{cases}$
Lube et al. (2005)	$\begin{cases} 1.2a, & a < 2.3 \\ 1.9a^{2/3}, & a > 2.3 \end{cases}$	$\begin{cases} a, & a < 1.15 \\ a^{2/5}, & a > 1.15 \end{cases}$
Staron and Hinch (2005)	$\begin{cases} 2.5a, & a < 2 \\ 3.25a^{0.705}, & a > 2 \end{cases}$	$\begin{cases} a, & a < 1 \\ 0.65a^{0.35}, & 1 < a < 10 \\ 1.45a^{2/5}, & a > 10 \end{cases}$

core moves very little if at all, resulting in a largely flat undisturbed upper surface. As the aspect ratio of the initial column increases, less material remains stationary and eventually almost all the material contributes to the collapse. The second regime, for high values of a , has most of the grains participating in the dynamics. The collapse is more energetic and the initial downward momentum is redirected sideways, resulting in longer run-outs and thin tails near the nose of the pile.

It is tempting to assume that the final slope of the pile reflects the frictional properties of the material rather than the flow dynamics. The findings from Lube et al. (2004) suggest that the pile's final height and run-out do not depend at all on the internal friction angle of the material. Lajeunesse et al. (2004) proposed that for shallow columns, there is a dependency on the internal friction angle ϕ but not for tall columns. Balmforth and Kerswell (2005) suggested that h_∞ and r_∞ are related to h_0 and r_0 by a power law of a multiplied by a coefficient, which is a function of internal friction angle and bed friction. Balmforth and Kerswell (2005) points out that for their experiments of a granular collapse in a narrow channel, the final slopes near the edge of the original column match closely to the internal friction angle. No matter what

theory is adopted, the granular behaviour during a collapse is undoubtedly complex and multi-faceted. The purpose of the simulation presented herein is not to reproduce in detail the findings described above, but to observe the behaviour of the granular material subjected to such complex circumstances and to verify that the resulting stationary pile transmits its bulk weight to the horizontal surface. The height of the final deposit and the run-out are compared with the scaling laws proposed in Lube et al. (2005) and Staron and Hinch (2005) for two-dimensional collapse and to the seminal work by Lube et al. (2004) and Lajeunesse et al. (2004) on axisymmetric granular collapses.

For the computer simulations presented herein, the computational model consists of the collapse of a granular column onto a flat surface. The aspect ratio of the column is kept constant and the internal angle of friction is varied. It is expected that a higher angle of friction will produce a smaller run-out because more energy is dissipated in the collapse, leading to a smaller horizontal flow. The central region of stationary grains may also be larger for higher friction angles, also due to the higher energy dissipation. Between the central core and the nose, the slope of the pile is expected to be steeper for higher friction angles. Near the location of the edge of the original column, the final pile may have a slope similar to the internal angle of friction of the material as suggested by Balmforth and Kerswell (2005). The slope of the pile near the nose is expected to be small, due to the dynamics of the run-out. The slope near the summit of the deposit depends the aspect ratio of the column, but for shallow column, the summit should remain flat or mildly sloped.

6.2.2 Granular collapse in two dimensions

In this simulation, a square two-dimensional granular column is released from rest and forms a pile. The aspect ratio $a = h_0/r_0$ of the column is kept constant at a value of 2, while three different internal angles of friction are simulated: 40° , 30° , and 20° .

The two-dimensional computational domain is $8\text{ m} \times 3\text{ m}$ containing a $2.5\text{ m} \times 2.5\text{ m}$ granular column with 1024 solids, a 8 m long horizontal surface and no fluid. Each solid has a density $\rho_s = 1000\text{ kg/m}^3$, weighing 2.83 kg per metre depth. The solid has a normal spring stiffness of 10^5 N/m and a coefficient of restitution of 0.8. The geometry of the system is the same as in figure 6.5 with $r_0 = 1.25\text{ m}$ and $h_0 = 2.5\text{ m}$. The relevant simulation parameters are summarized in table 6.3.

Table 6.3 – Granular collapse in two dimensions: simulation parameters.

r_0	h_0	R	ϵ	ϕ	k_n	Δx	Solids	Particles
1.25 m	2.5 m	0.03 m	0.8	$40^\circ, 30^\circ, 20^\circ$	10^5 N/m	0.01 m	1024	20,992

Figure 6.6 shows a time series of the granular collapses. The vertical and horizontal forces on the horizontal surface are plotted in figure 6.7. After the pile reaches static equilibrium, the vertical force on the surface should equal the bulk weight of the granular material: $1024\rho_s g \pi R^2 = 28.4\text{ kN}$. The bulk weight is indicated in figure 6.7 as the *expected value*. By symmetry, the horizontal force on the surface should be zero. Table 6.4 compares the computational results to the scaling laws presented earlier in table 6.2.

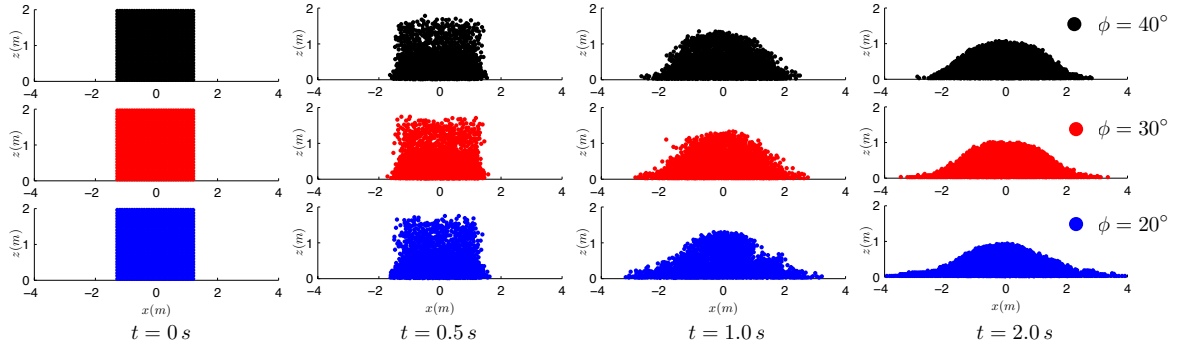


Figure 6.6 – Granular collapse in two dimensions: computational results. The time series shows a granular material with three different angles of internal friction: (top) $\phi = 40^\circ$, (middle) $\phi = 30^\circ$, and (bottom) $\phi = 20^\circ$.

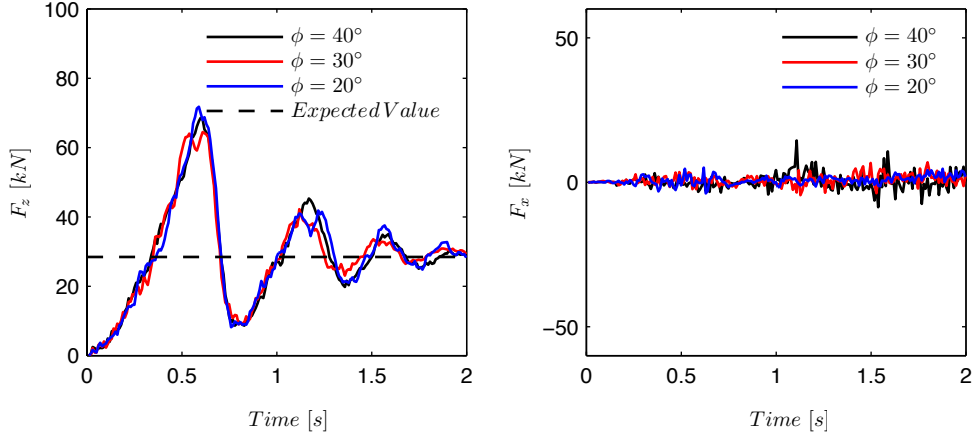


Figure 6.7 – Granular collapse in two dimensions: (left) vertical and (right) horizontal forces with time.

The time series in figure 6.6 shows a few of the key characteristics of a granular collapse. First, the grains near the edge of the column start to flow as seen at $t = 0.5\text{ s}$. This is followed by a slope developing upon which material slides down, evident at $t = 1.0\text{ s}$. The initial vertical momentum is redirected sideways in a spreading motion

Table 6.4 – Granular collapse in two dimensions: comparison with theory. Final height and final run-out for a column of fixed aspect ratio $a = 2$ ($r_0 = 1.25\text{ m}$, $h_0 = 2.5\text{ m}$). The internal angles of friction used in the various studies are: Lube et al. (2004) ($\phi = 30^\circ\text{--}35^\circ$), Lajeunesse et al. (2004) ($\phi = 21^\circ$), Lube et al. (2005) ($\phi = 29.5^\circ\text{--}35^\circ$), and Staron and Hinch (2005) ($\phi = 20^\circ$).

ϕ [°]	r_∞ [m]	h_∞ [m]
40	2.9	1.1
30	3.4	1.0
20	4.3	0.94
Lube et al. (2004)	4.1	1.2
Lajeunesse et al. (2004)	4.8	0.93
Lube et al. (2005)	4.3	1.6
Staron and Hinch (2005)	7.5	1.0

observed from $t = 0.5\text{ s}$ to $t = 2.0\text{ s}$. The aspect ratio simulated is neither shallow nor tall, but in a transitional regime. The fact that the final deposit does not have a flat summit shows that there was some grain movement in the central region of the initial column. Nonetheless, it is evident that there is a large portion of grains in the central column that contribute very little to the flow of the granular material. The effects of the material properties are noticeable. The material with the highest angle of friction spreads out the least and has the steepest maximum slopes. As ϕ decreases, the run-out increases, and the maximum slope decreases. From these three tests alone, it is not possible to tell how sensitive the material properties are to the shape of the final deposit. The run-out lengths between the three cases vary by over 30%, but in terms of grain size, they vary by less than 25 grain diameters.

The force time history in figure 6.7 shows that after the pile reaches static equilibrium, the forces calculated on the supporting surface agree with the bulk weight of the granular material. During the granular collapse, considerable oscillations in the vertical force are observed. Indeed, the inertia from the collapse may give rise to a force on the supporting surface that is greater than the bulk weight of the material. Since the collapse occurs in several stages, it may be possible for the force to decrease below the bulk weight at several instances during the collapse as observed in figure 6.7; although, at a first glance, it seems to make little physical sense. It is probable that these oscillations are a product of the spring stiffness k_n assigned to the solid material and the damping effect, which is due to η_n .

It is clear from table 6.4 that the scaling laws from different authors vary somewhat. The findings by Lajeunesse and Lube are based on laboratory experiments, while those by Staron are from numerical simulations. Notice that the scaling laws by all three authors have similar exponents on a but Staron found considerably larger coefficients

(see table 6.2). The difference is attributed to material properties. In the computer simulations, the circular shape of the grains is thought to enhance their mobility. Furthermore, the quasi-two dimensional experiment by Lube et al. (2005) is carried out in a vertical channel with sidewalls, which may increase dissipation of energy. From Staron's observations, it was expected in the present study to have computational results that over predict the theories in the laboratory experiments. Contrarily, the computational results slightly under predict the run-out distances predicted by the various theories. The height of the final deposit, however, agrees fairly well with the various theories.

There are too few simulations carried out in the present work to determine exactly how well the numerical model matches the theories. Nevertheless, the following conclusions and observations can be made: (1) the computational results show some of the key characteristics of a granular collapse, (2) the bulk weight of the granular material is accurately calculated for a pile in static equilibrium through a network of contact forces, and (3) a material with a higher friction angle more readily dissipates energy and subsequently forms a steeper pile with less run-out. In the next section, the simulation of a granular collapse in three dimensions is presented.

6.2.3 Granular collapse in three dimensions

In this simulation, a cubic three-dimensional granular column is released from rest and forms a pile. The aspect ratio of the column is $a = 2$ and one internal angle of friction of 40° is simulated.

The three-dimensional computational domain is $2.5\text{ m} \times 2.5\text{ m} \times 0.4\text{ m}$ containing a cubic granular column with 1000 solids, a 2.5 m long horizontal surface and no fluid. Each solid weighs 0.0335 kg , has a normal spring stiffness of 10^5 N/m and a coefficient of restitution of 0.8. The geometry of the system is a three-dimensional version of figure 6.5 and the relevant simulation parameters are summarized table 6.5.

Table 6.5 – Granular collapse in three dimensions: simulation parameters.

r_0	h_0	R	ϵ	ϕ	k_n	Δx	Solids	Particles
0.3 m	0.6 m	0.02 m	0.8	40°	10^5 N/m	0.01 m	1000	109,081

Figure 6.8 shows a time series of the granular collapse. The simulation shows similar behaviour to the two-dimensional case. Unlike the two dimensional case, where the grain size $2R$ was kept to be much smaller than the length scale of the problem, namely $r_0/(2R) > 20$, in three dimensions, this restriction was not enforced. If it were, the simulation would have required 64,000 solids instead of 1000 as presented in this

section. While simulating 64,000 solids is computationally viable, it was decided to focus on the two-dimensional case. The simple three-dimensional simulation allows for a qualitative comparison to the two-dimensional simulation. The same key elements of the granular collapse are observed in this three-dimensional simulation. The initial vertical fall is redirected sideways into a spreading motion. When compared to the two-dimensional case, the final run-out is not as pronounced.

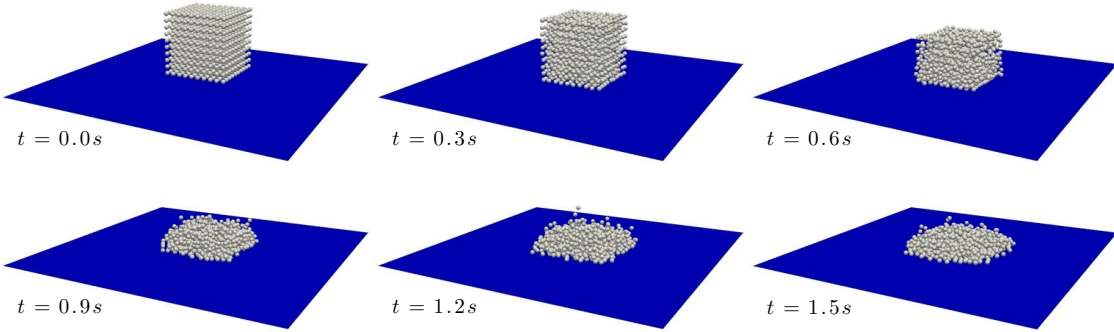


Figure 6.8 – Granular collapse in three dimensions: computational results. The time series shows a granular material with $\phi = 40^\circ$, and an aspect ratio $a = 2$ ($r_0 = 0.3\text{ m}$, $h_0 = 0.6\text{ m}$).

6.2.4 Granular collapse of dilated circular discs in three dimensions

Recall that particles with high aspect ratios may have preferential orientations in a granular flow. The flow dynamics can be quite different from that in a granular material made up of perfect spheres. Since the thickness of an ice floe is generally much smaller than its length, the ability to model high aspect ratio solids provides a useful step towards one of the objectives of this thesis: the accurate numerical simulation of river ice flows. While the hard-sphere model can handle any arbitrarily shaped solid with relative ease, it is not suitable for dense systems or for calculating contact forces. For this reason, it is desired to have a soft-sphere model that can model high aspect ratio particles. Although the soft-sphere model is not as readily modified to handle particles of arbitrary shape, it can be modified to model three-dimensional circular discs. Following Hopkins et al. (1996), the new developments to the existing SPH code contain the ability to model three-dimensional circular discs.

In this simulation, a staggered array of three-dimensional circular discs form a column and the column is released from rest to form a pile. One internal angle of friction of 20° is used. The three-dimensional computational domain is $1\text{ m} \times 1\text{ m} \times 1\text{ m}$ containing a staggered array of 54 solids, a $1\text{ m} \times 1\text{ m}$ horizontal surface with walls and no fluid. Each solid weighs 2.06 kg , has a spring stiffness of 10^5 N/m and a coefficient of restitution of 0.5. The relevant simulation parameters are shown in table 6.6.

Table 6.6 – Granular collapse of dilated circular discs in three dimensions : simulation parameters.

r_0	h_0	R_{Disc}	t_{Disc}	ϵ	ϕ	k_n	Δx	Solids	Particles
0.5 m	1 m	0.125 m	0.05 m	0.5	20°	$10^5 N/m$	0.017 m	54	56,376

Figure 6.9 shows a time series of the granular collapse. Only 54 solids are simulated; therefore, it is not expected that the main elements of a granular collapse will be observed. Nevertheless, the formation of a pile is observed without interpenetration of solids or other unrealistic qualities.

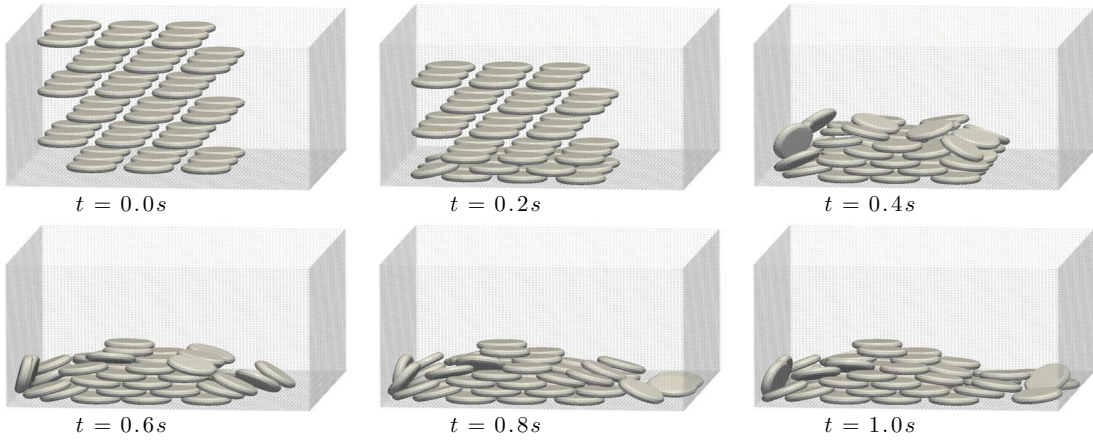


Figure 6.9 – Granular collapse of dilated circular discs in three dimensions: computational results. The time series shows a granular material with $\phi = 20^\circ$, and an aspect ratio $a = 2$ ($r_0 = 0.5 m$, $h_0 = 1 m$).

6.3 SPH simulations with freely moving solid objects

One of the objectives of this thesis is to implement the accurate numerical simulation of freely moving solids in a free-surface flow. Before this thesis work, i.e. in the existing SPH framework as defined in section 3.10, solids could only move if their motion was fully prescribed by the user. The developments made as part of this thesis have allowed the free movement of solids in a free-surface flow. Their motion is no longer prescribed by the user, but by the flow conditions in the simulation.

To demonstrate these developments, three simulations are presented. The first consists of a triangular wedge falling into calm water. The hydraulic forces on the wedge are calculated and compared to laboratory experiments and an approximate analytical solution. The second simulation evaluates the effects of buoyancy on solids with different densities. The results are evaluated based on Archimedes' principle. The third simulation involves multiple solids driven by a water stream and the results show believable fluid-solid and solid-solid interactions.

6.3.1 Wedge entry

The aim of this simulation is to evaluate the fluid-solid coupling of a solid in a free-surface flow. The simulation involves the free fall of a triangular wedge entering calm water. The hydraulic force time history is compared to laboratory experiments and approximate analytical solutions proposed by Zhao et al. (1997). The pressure distribution in the water column from the impact of the wedge is compared to computational results by Oger et al. (2006).

The experiments in Zhao et al. (1997) involve a triangular wedge attached to a trolley with vertical guide-rails that restrict any horizontal or angular motion. The wedge is raised to a specified height above the calm water, and then released from rest. The force, pressure, acceleration and velocity time histories are measured using instrumentation detailed in their paper. The numerical simulation presented herein allows the wedge to move freely in the vertical direction subject to gravitational and hydrodynamic forces, but its horizontal motion and rotation are restricted to mimic the test rig used in the experiment. In the experiment, the vertical velocity of the wedge just before impacting the water was 6.15 m/s . Measurements were presented for the first 0.025 s after initial impact.

Oger et al. (2006) used SPH to simulate wedge entry into calm water. The purpose of their study was to validate a spatially varying SPH particle resolution and a new technique to evaluate fluid pressure on solid boundaries. They also compared their results to the laboratory experiments and analytical solutions in Zhao et al. (1997). Oger et al. (2006) used a weakly compressible classical SPH formulation with a spatially varying particle resolution to compute their results. Since they used a slightly different SPH formulation than in the present work, it is interesting to compare the two computational results.

The two-dimensional computational domain has one symmetrical triangular wedge 0.5 m wide with a 30° deadrise angle, and a $4\text{ m} \times 2\text{ m}$ tank containing still water with a hydrostatic pressure distribution. The dimensions of the tank were chosen so that a pressure disturbance from the wedge's impact will not reach the edge of the tank over the course of the simulation.

Recall that the numerical speed of sound is chosen as ten times the maximum fluid velocity in the simulation. This restricts the variations in fluid density to less than 1%. The numerical speed of sound also dictates at what speed a pressure wave propagates through the fluid medium. In this simulation, the numerical speed of sound was taken to be 80 m/s and the simulation runs for 0.025 physical seconds. Therefore, a pressure wave can travel a maximum of 2 m over the course of the simulation.

In Zhao's experiment, the wedge is dropped from approximately 2 m to reach a velocity of 6.15 m/s just before impact with the free-surface. For the numerical simulation presented herein, the wedge is placed just above the free-surface and given an initial velocity of 6.15 m/s . This eliminates the needless computation time of the wedge falling solely under the force of gravity. Figure 6.10 shows the geometry of the system and lists the key parameters for the simulation.

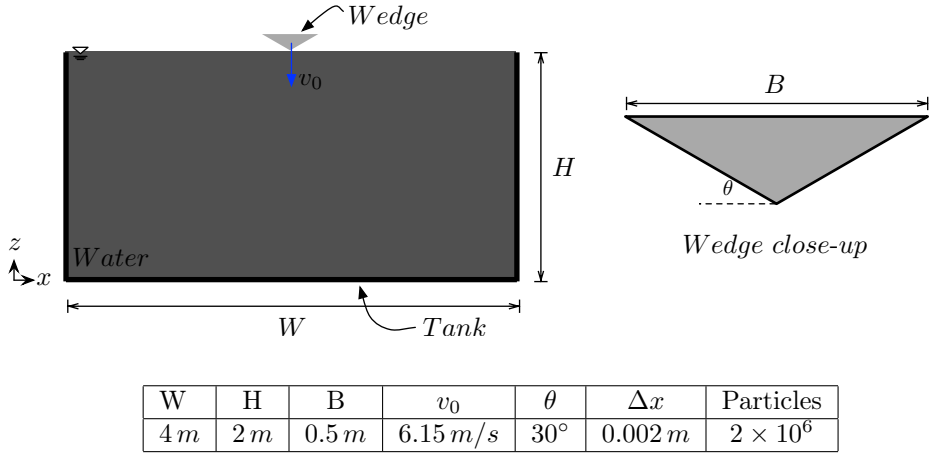


Figure 6.10 – Wedge entry: numerical setup.

The approximate analytical solution presented in Zhao et al. (1997) is a two-dimensional fully non-linear solution for an asymmetric body with a time dependent vertical downward velocity, forced through initially calm water. Both viscous effects and compressibility are ignored, so the problem is solved using potential theory. The solution is solved numerically but from theory specific to potential flow past a wedge with a free-surface. Similarity solutions have been theoretically derived for a wedge entry with constant vertical velocity (Dobrovol'Skaya, 1969) and approximate solutions at small deadrise angles (Wagner, 1932).

Figure 6.11 compares the wedge entry simulation in this thesis to computational results presented in Oger et al. (2006). The colour gradient in both simulations similarly scales pressure and the frames of the time series are taken at the same instant in time. Figure 6.12 compares the vertical force history on the wedge calculated in this thesis to the experimental and approximate analytical results in Zhao et al. (1997) as well as the computational results in Oger et al. (2006).

Since the computational results in the present study are calculated using SPH-ALE with a Riemann solver and the results in Oger et al. (2006) are calculated using classical SPH, it is not surprising the results show some differences. The propagation

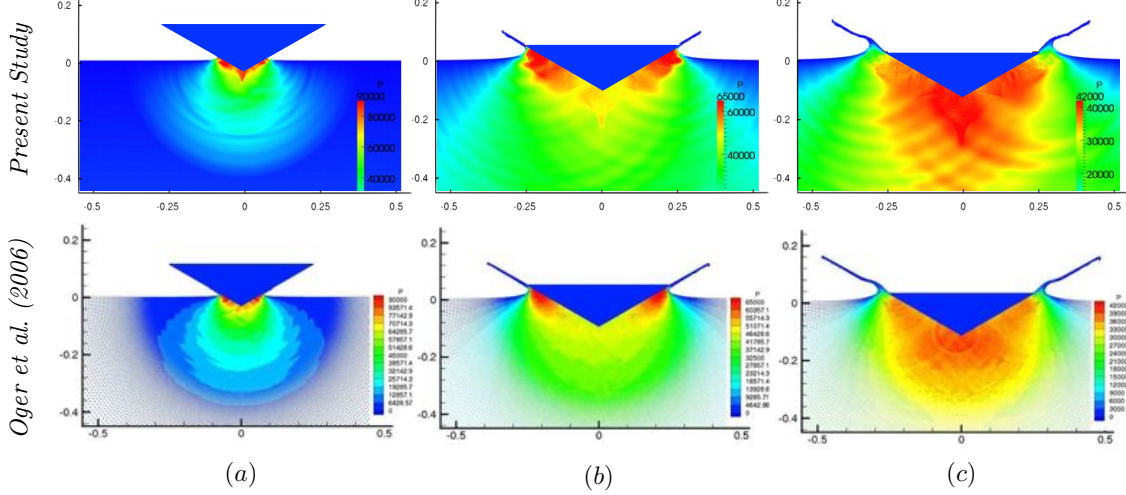


Figure 6.11 – Wedge entry: computational results. Time series of wedge entry at (a) $t = 0.00435\text{ s}$, (b) $t = 0.0158\text{ s}$, and (c) $t = 0.0202\text{ s}$. The colour gradient shows pressure scaled from (a) 0 to $90,000\text{ Pa}$, (b) 0 to $65,000\text{ Pa}$, and (c) 0 to $42,000\text{ Pa}$. (Top) present study, and (bottom) computational results from Oger et al. (2006).

of the pressure waves appears more pronounced in the SPH-ALE case. Nevertheless, the shape of the free-surface and the overall pressure distribution in the two cases are very similar, at least when visually comparing them.

Figure 6.12 shows that the SPH force calculations are reasonably close to the experiments and theory presented in Zhao et al. (1997). In the first 0.0025 s , the SPH results oscillate noticeably and over predict the expected values of vertical force on the wedge. This error may be due to using a discretization size that is too coarse. Recall that a solid is composed of boundary elements that are used to calculate the pressure on the solid. As the wedge enters the water, there are initially very few boundary elements in contact with the water. This could lead to jumps and drops in the force calculation as observed in figure 6.12. After 0.0025 s , the force history becomes smoother and follows more or less the predicted results. Zhao et al. (1997) attributes the differences in the theoretical and experimental results to the three-dimensional effects that are not considered in the theoretical solution. They appear to become important after approximately 0.0075 s , when the two curves start to separate. Since the simulation in this thesis is two-dimensional, one would expect the SPH results to be closer to the theoretical solution than the experiments. Nevertheless, it is not surprising that the SPH results are lower than the theory because of the numerical dissipation inherent in any numerical scheme.

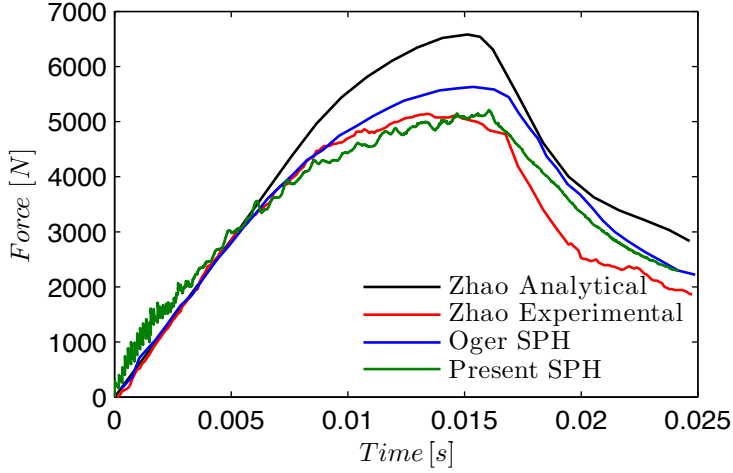


Figure 6.12 – Wedge entry: vertical force time history. The results are compared to approximate analytical solutions and experiments by Zhao et al. (1997), as well as other computational results by Oger et al. (2006).

6.3.2 Falling solids with different densities

The purpose of the simulation of falling solids with different densities is to evaluate the effects of buoyancy on a solid in a free-surface flow. The simulation involves the free fall of a solid into calm water. The density of the solid is changed from one simulation to the next to observe the effects of buoyancy. The computational results show the same simulation at three different solid densities: 500 kg/m^3 , 1000 kg/m^3 , and 2000 kg/m^3 .

The two-dimensional computational domain has one $0.1 \text{ m} \times 0.1 \text{ m}$ square solid above a $0.5 \text{ m} \times 0.5 \text{ m}$ water column with an initial hydrostatic pressure distribution. There are periodic boundary conditions in the horizontal direction. The solid is released from rest under the force of gravity and impacts the calm free-surface. Depending on its density, the solid will either sink or float. The two-dimensional solid has all its degrees of freedom. That is, it can move in the x - and z -directions as well as rotate about the y -axis. Figure 6.13 shows the geometry of the system and lists the key parameters in the simulation. The geometry of the system is identical to that used in Lee et al. (2010).

For this simulation, the computational results are not compared with analytical solutions or experiments. We will apply Archimedes' principle without any calculations to determine if the simulation results are believable. It is expected that the lighter solid will float with half its volume above the free-surface. The neutrally buoyant solid is expected to have its whole volume immersed in water. It should be suspended in

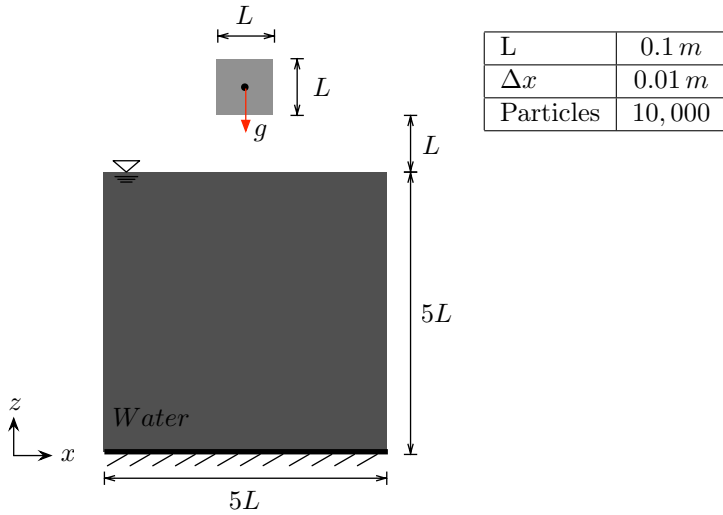


Figure 6.13 – Falling solid with different densities: numerical setup.

the water column, neither sinking nor floating. The heavier solid is expected to sink to the bottom of the water column.

Figure 6.14 shows a time series of the numerical simulations. For the lighter solid, the free-surface is disturbed slightly as the solid enters the water. The fluid motions are small due to the disturbance of the solid. As predicted, the solid floats with roughly half its volume above the free-surface. Observe that the solid rotates 45° . A simple righting moment analysis shows that at this solid density, this is its natural equilibrium position. The neutrally buoyant solid enters the free-surface so that its entire volume is immersed in the water. The solid does, however, rise slightly so that a small portion is above the free-surface. The heavier solid, as expected, sinks to the bottom and causes the largest fluid motion compared to the lighter solids. The computational results are in reasonable agreement with the predicted outcome following Archimedes' principle.

6.3.3 Solids driven by a water stream

The previous simulations presented in section 6.3 contain only a single solid. Their aim is to evaluate the fluid-solid coupling in terms of the hydraulic force on a freely moving solid. The purpose of this simulation is to evaluate the combined effect of hydraulic and contact forces on multiple solids. Using the hard-sphere model, three-dimensional solids with six degrees of freedom are driven through a stepped-channel by the hydraulic forces from a stream of water. Their motion is governed by the hydraulic forces from the stream and by any collisions that occur between the solids. The simulation is similar to that described in Wei (2006) presenting the implementation of

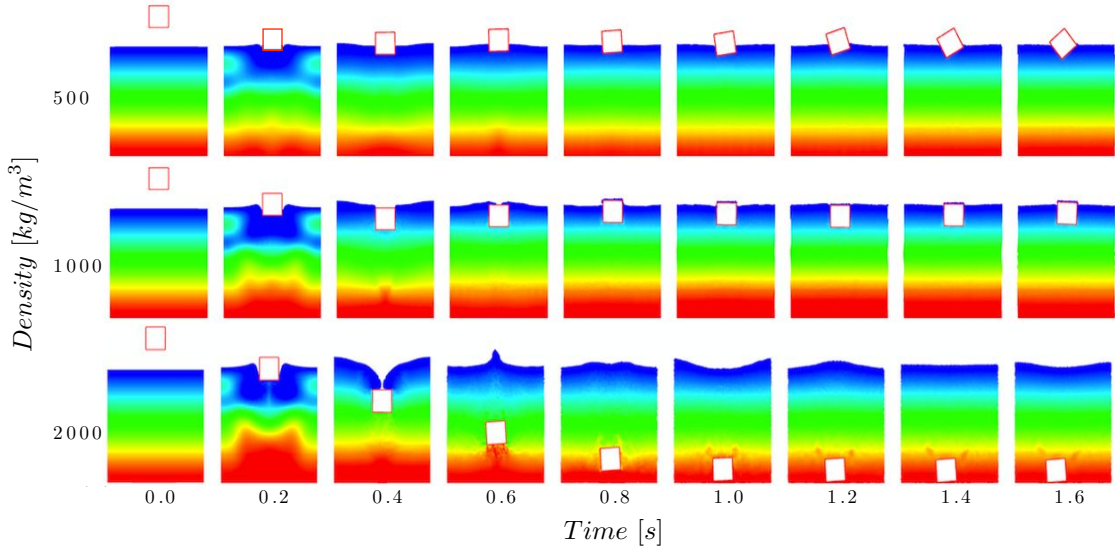
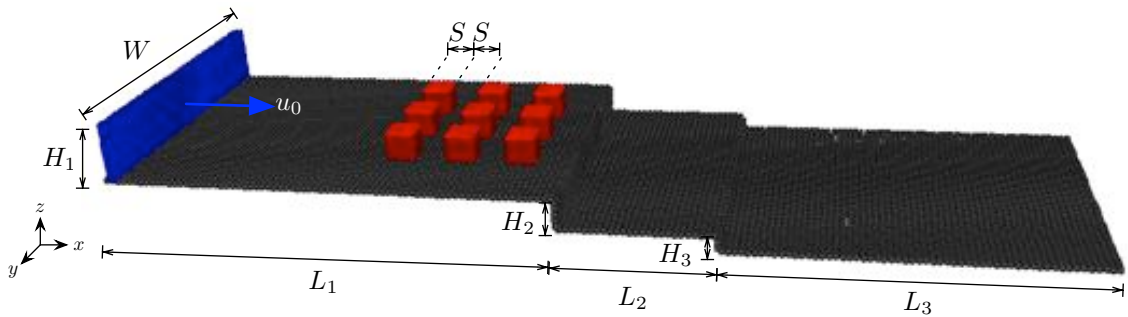


Figure 6.14 – Falling solids with different densities: computational results. The colour gradient shows pressure from zero (blue) to hydrostatic (5000 Pa) (red).

freely moving solids in the commercial software Flow-3D.

As shown in figure 6.15, the computational domain is 9.5 m long, 3 m wide and 1.2 m high. It contains a stepped channel, nine 0.3 m cubic solids initially at rest on the top-most level of the channel. A 0.6 m high stream of water moving at 4 m/s enters the problem domain and floods the channel, pushing the solids down the steps. Both the solids and the channel bed have a coefficient of restitution of 0.8. The solids have a density of 2500 kg/m^3 .



W	L_1	L_2	L_3	H_1	H_2	H_3	S
3 m	4.5 m	1.5 m	3.5 m	0.6 m	0.3 m	0.15 m	0.3 m

u_0	ρ_s	ϵ	Δx	Particles (max.)
4 m/s	2500 kg/m^3	0.8	0.06 m	123,730

Figure 6.15 – Solids driven by a water stream: numerical setup.

It is expected that the water stream will push the solids down the stepped channel. Once the stream impacts the solids, they will experience many collisions with the channel bed and each other. The collisions are expected to be particularly strong when the solids fall over the steps in the channel. After the water hits the solids, the flow that is obstructed in the central region of the channel will be redirected along the sides. The flow is, therefore, expected to be faster along the sides of the channel than in the central region behind the solids.

This computational model cannot be easily compared to analytical solutions or theory. Nevertheless, the two features governing the solid's motion: hydraulic and collision forces have been compared with theory in the previous simulations presented in this chapter. The computational results in this section serve as proof that solids subjected to a combination of hydraulic and collision forces in a complicated flow can move in a realistic manner. Some possible outcomes that would make the simulation unrealistic are: (1) if the SPH fluid particles penetrate the solid surfaces, and (2) if solid surfaces penetrate other solids. The results will be assessed qualitatively.

The time series in figure 6.16 shows the nine solids driven down the stepped channel by the water stream. The computational results agree more or less with the predicted outcomes. The strongest collisions appear to be between $t = 0.6\text{ s}$ and $t = 1.2\text{ s}$ as the solids fall down the steps. The flow moves faster along the sides of the channel going around the solids. No interpenetration of fluid-solid interfaces or solid-solid interfaces is observed. The solids move down the channel in a manner that is believable to the mind's eye.

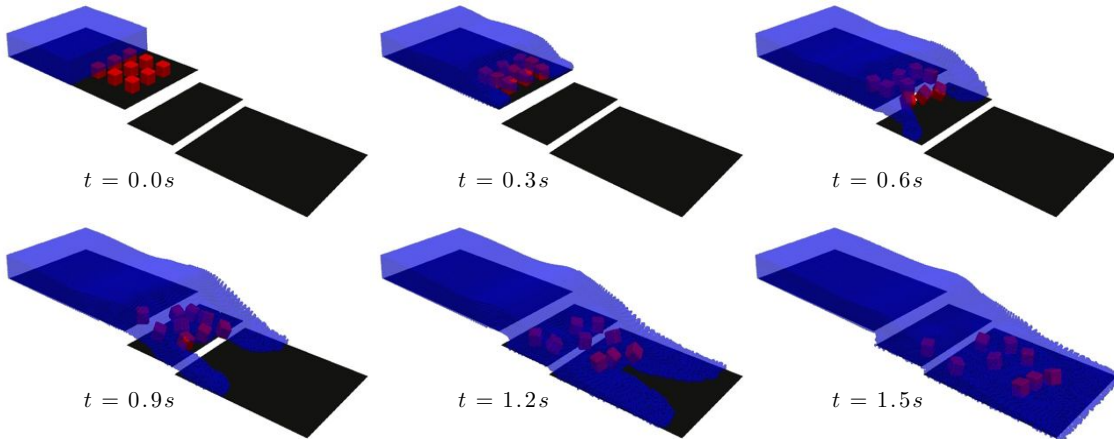


Figure 6.16 – Solids driven by a water stream: computational results.

6.4 Summary

The groundwork has been laid for the simulation of free-surface flows containing freely moving objects. The applicability of these new developments is not exclusive to river ice flows, but could be used for many engineering problems. Debris flows, rockfalls into lakes, and floating breakwaters are all examples of engineering problems where these new capabilities could be applied. The next chapter applies these new developments to a few simple river ice dynamics problems.

Chapter 7

Ice jam simulations

This chapter describes three numerical simulations related to ice jams. First, floating blocks are simulated approaching a stationary cover. Depending on the block geometry and the flow conditions, they accumulate at the leading edge of the stationary cover or they are entrained under the stationary cover. The results are compared to the theory presented in chapter 5. The second simulation calculates the hydrodynamic forces exerted on an individual ice floe after it has come to rest against a stationary cover. The chapter concludes with a simulation of ice floes accumulating upstream of an obstruction composed of cylindrical piers. The force history on the piers is calculated during the jam evolution.

These three simulations were chosen to demonstrate the dynamic effects that are not accounted for in most current ice jam analyses. For example, the approximate analytical methods to predict floating block stability assume a uniform flow upstream and beneath the floating block. They also assume hydrostatic pressure distributions. Furthermore, only the pressure on the bottom face of the block is considered. The first simulation considers the pressure on all the block faces and there is no assumption about the shape of the pressure distributions. The second simulation shows that the pressure distribution under a stationary floating block is non-uniform. The third simulation shows how jam initiation can be a highly dynamic process. Existing highly sophisticated river ice dynamics models solve the unsteady shallow water equations to model the river flow. When the characteristic horizontal length scales are much greater than the vertical length scales, as is the case in most river engineering problems, the simplifying assumptions associated with the shallow water equations are valid. These assumptions can break down in the dynamic regions where the flow is no longer gradually varied and the vertical pressure distribution deviates from hydrostatic, for example, near the leading edge or the toe of an ice jam. For violent river ice events, such as jam release waves or the arrest of a breaking front, the dynamic effects can also play a significant role.

7.1 Floating block stability

A floating block of constant length and thickness was simulated approaching a stationary cover of the same thickness. The flow velocity was increased incrementally, corresponding to a range of densimetric Froude numbers between 0.2 and 2.0 in increments of 0.2. The block thickness to flow depth ratio $\frac{t_i}{H}$ was varied from 0.1 to 0.6 in

increments of 0.1. All other parameters were kept the same. The results were compared with approximate analytical solutions from Pariset and Hausser (1961), Ashton (1974), and Daly and Axelson (1990); and with experimental data from Uzuner and Kennedy (1972).

The numerical setup matches that shown in figure 7.1. The computational domain contains one 0.097 m by 0.382 m freely moving block, and one stationary block of the same length. The solids have a coefficient of restitution of 0.8, and a density of 874 kg/m^3 . While the density of ice is usually near 920 kg/m^3 , the density and geometry in this simulation were chosen to match laboratory experiments by Uzuner and Kennedy (1972). Table 7.1 summarizes the test parameters used in the simulation, which match one of several laboratory experiments by Uzuner and Kennedy (1972).

Table 7.1 – Floating block stability: simulation parameters.

F_D	$\frac{\rho_i}{\rho_w}$	$\frac{t_i}{L}$	$\frac{t_i}{H}$	t_i	ϵ	Δx	Particles
0.2–2.0	0.874	0.254	0.1–0.6	97 mm	0.8	0.0085	50,000

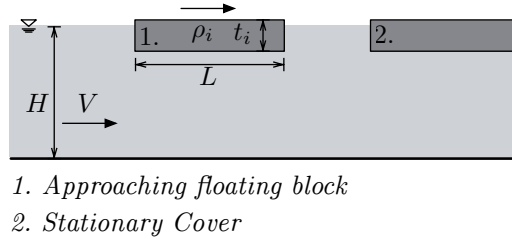


Figure 7.1 – Floating block stability: numerical setup.

Figure 7.2 shows a representative time series of a floating block under-turning with a densimetric Froude number greater than the critical value. In total, there were 60 simulations run at different values of F_D and $\frac{t_i}{H}$. Figure 7.3 compares the results in all of the simulations to the approximate analytical solutions and laboratory data. The top limit of the error bar indicates the densimetric Froude number at which under-turning was observed. The bottom limit indicates the nearest simulation at a lower densimetric Froude number at which there was no under-turning. The critical value is, therefore, between these two.

From figure 7.3, the SPH simulations agree well with theory and experiments for large values of $\frac{t_i}{H}$, from 0.4 to 0.6. For smaller values of $\frac{t_i}{H}$, from 0.1 to 0.3, the SPH simulations tend to overestimate the critical densimetric Froude number. Since the approximate analytical solutions assume a uniform velocity profile with depth and a hydrostatic pressure distribution, the SPH results were not expected to match perfectly. The greater concern is that the SPH results agree poorly with the experimental

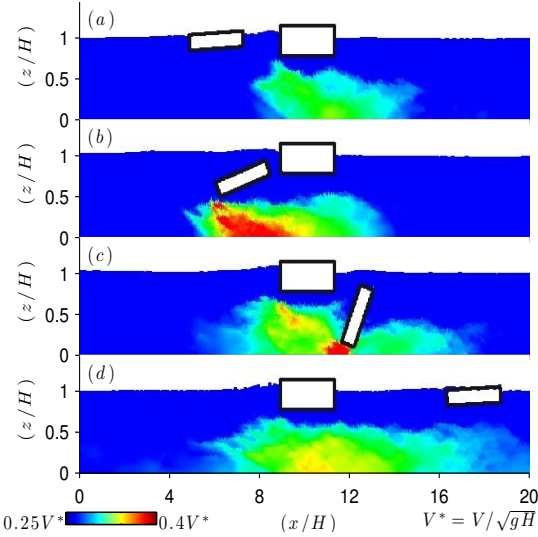


Figure 7.2 – Floating block stability simulation: a representative time series of a floating block under-turning with a densimetric Froude number greater than the critical value for times (a) 0 s, (b) 2.5 s, (c) 5.0 s, (d) 7.0 s, $F_D = 1.6$ and $\frac{t_i}{H} = 0.2$.

data for smaller values of $\frac{t_i}{H}$ and that the approximate analytical solutions match the data more closely. One possible explanation could be that the stationary block in the SPH simulation should be longer. Since the stationary block is relatively short in length, the deceleration of flow at the trailing edge may influence the flow conditions at the leading edge, which may lead to higher critical values of F_D . This effect would likely be less pronounced at shallower flow depths, since the block length does not change and the flow depth under the block decreases. This could explain why there is better agreement between the SPH results and experiments for higher values of $\frac{t_i}{H}$. While efforts were made to closely match the experiments in Uzuner and Kennedy (1972), there is no indication of the length of the “downstream support block.” The difference between the computed and the observed results are discussed further in 7.2.

7.2 Dynamic pressure on a partially submerged stationary block

In this simulation, the dynamic pressure beneath a partially submerged stationary block was examined. The motivation of this simulation is to better understand the complex flow dynamics near the leading edge of an ice cover. It is these flow conditions that determine whether approaching ice floes accumulate at the leading edge or are entrained by the flow. The results are compared to experimental data from Dow Ambtman et al. (2011a).

The two-dimensional computational domain contains one partially submerged stationary block and a free-surface flow moving from left to right. The simulation is run

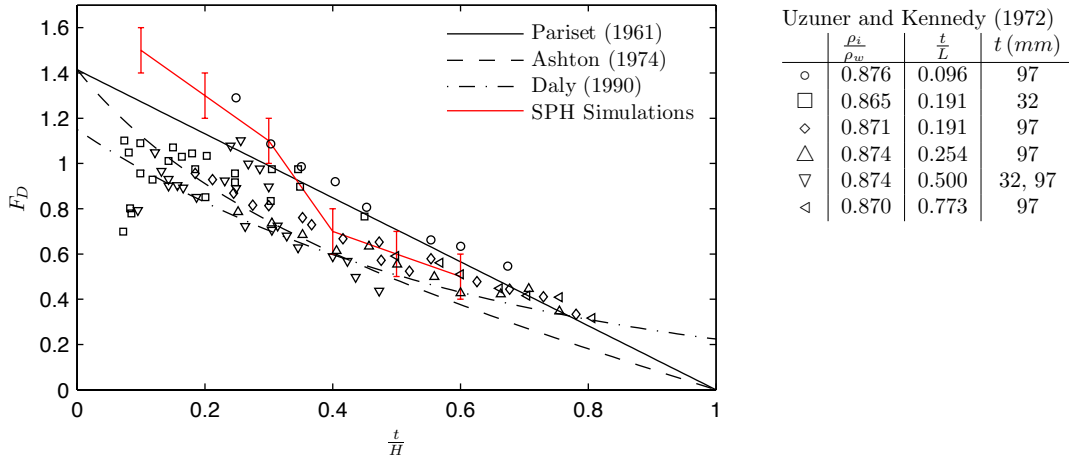


Figure 7.3 – Floating block stability: comparison of SPH results with theory and experiments. The top limit of the error bar indicates the F_D at which under-turning was observed. The bottom limit indicates the nearest simulation at a lower F_D at which there was no under-turning. The critical value is between these two. The results are compared to approximate analytical solutions by Pariset et al. (1966), Ashton (1974), and Daly and Axelson (1990), and experiments by Uzuner and Kennedy (1972).

at three different discharges. The computational setup is shown in figure 7.4. Table 7.2 summarizes the parameters used in both the SPH simulation and the laboratory experiment.

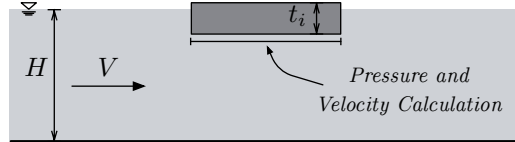


Figure 7.4 – Dynamic pressure on a partially submerged stationary block: numerical setup.

Following from the physical description in section 2.3, the dynamic pressures are expected to be most pronounced near the leading edge of the block. Farther downstream, they are expected to decrease as the vertical and horizontal accelerations dwindle. Figure 7.5 shows the dynamic pressure and velocity distribution beneath the block. In the present study, the marker symbols indicate the location of the *pressure probes* along the underside of the stationary block, where the pressure was recorded. For the laboratory experiments in Dow Ambtman et al. (2011a), the marker symbols indicate the location of the *pressure taps* connected to a manometer board. In their study, they measured the pressure distributions under a rectangular block with a sharp leading edge and one with a rounded leading edge. In the present work, only a rectangular block with a sharp leading edge was simulated.

Table 7.2 – Dynamic pressure on a partially submerged stationary block: simulation parameters. The simulation parameters were chosen to match the experimental data in Dow Ambtman et al. (2011a). The length of the stationary block in both cases is 0.5 m.

Run number	t_i (cm)	H (cm)	t_i/H	V (cm/s)
tH005-Q79	1.59	30.64	0.05	34.4
tH005-Q111	1.59	30.64	0.05	48.2
tH005-Q142	1.59	30.64	0.05	61.8
tH03-Q79	8.33	29.02	0.3	36.5
tH03-Q111	8.33	29.02	0.3	51.0
tH03-Q142	8.33	29.02	0.3	65.3

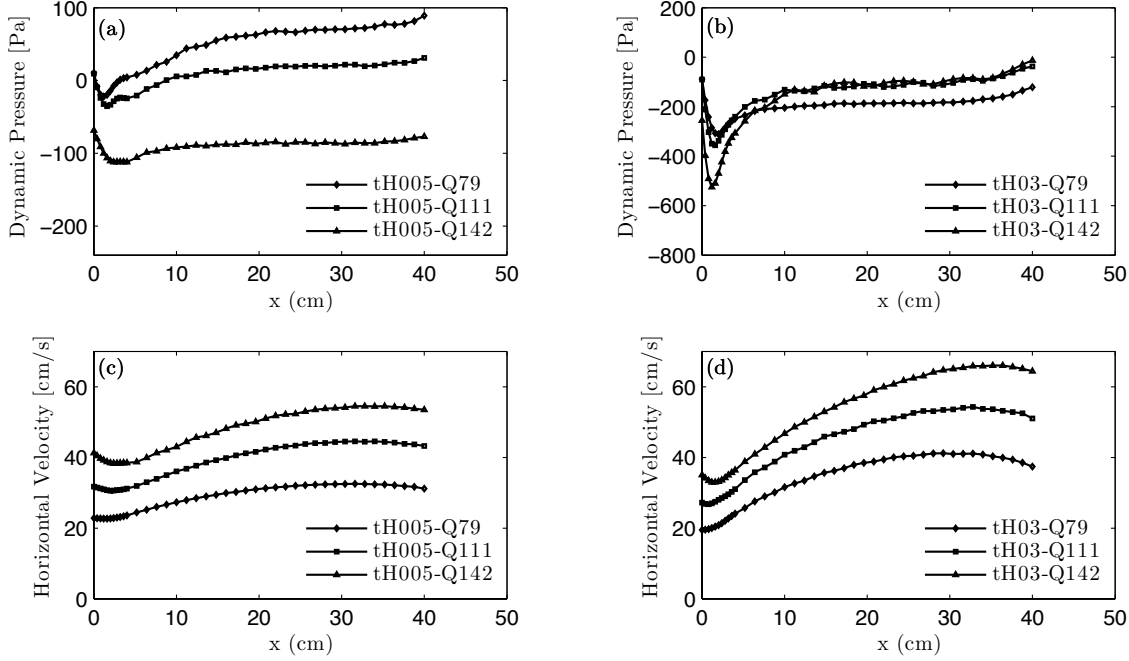
The dynamic pressures differ significantly between the numerical simulations and the laboratory experiments, both shown in figure 7.5. To explain these differences, it is first instructive to consider the fluid mechanics of the problem. There are two primary mechanisms that contribute to the shape of the pressure distribution beneath the stationary block. The first mechanism arises because the block reduces the cross-section of the flow; therefore, the velocity under the block increases, and by Bernoulli's principle, the pressure decreases. For a block with a flat underside overlying a flat bed surface, this pressure reduction is constant along the length of the block and results in an equally distributed downward force. The second mechanism is due to the hydraulics at the leading edge of the block. In this region, the flow undergoes rapid vertical and horizontal accelerations past the bottom upstream corner of the block, resulting in an area of increased velocities and decreased pressures. This decrease in pressure causes a localized downward force near the upstream edge of the block and results in an under-turning moment. The summation of the pressure distributions in the first and second mechanisms gives a region with the lowest pressures near the leading edge, then gradually increasing to a plateau farther along the length of the block. While both the computed and the observed pressure distributions in figure 7.5 show this characteristic shape, they differ substantially in magnitude and in the precise shape of the region near the leading edge. These differences are likely due to the numerical model failing to capture the important fluid dynamics phenomena at the leading edge of the block.

To further understand the given fluid mechanics problem, it can be idealized as a steady flow over a forward-facing step. For a sharp-edged bluff body, such as the rectangular block, the flow detaches from the upstream corner and reattaches on the block farther downstream. This creates a separation zone containing a vortex-filled wake, where the flow dynamics are considerably different from what is predicted by inviscid theory. Furthermore, the separation zone creates a suction drag that is generally much larger than the viscous drag from an attached boundary layer. To accurately describe

the flow dynamics of this problem in a numerical simulation, the model must be able to predict flow separation, re-attachment, the turbulence in the separation zone, and the flow in the boundary layer where viscous forces are important. Recall that the SPH formulation used for the numerical simulations presented herein solves the Euler equations describing the flow of an inviscid fluid. Therefore, it cannot accurately describe flows where viscous effects, separation zones, and boundary layer phenomena are dominant factors determining the overall nature of the flow. Given the limitations of the numerical approach and the complexity of the flow, it is understandable that the computed results are not in good agreement with the observed data.

It is interesting to note the differences between the observed pressure distributions for a rectangular block and a rounded block, both shown in figure 7.5. Compared to the rounded block, the rectangular block experiences larger reduced pressures near the leading edge, resulting in greater under-turning moments. Consequently, for the same thickness to depth ratio, the rectangular block would under-turn more readily than the rounded one. The difference in the pressure distributions is likely the result of the flow separation zone on the rectangular block, which creates increased suction drag. In the absence of adverse pressure gradients, the flow past the leading edge of the rounded block will stay attached and will create less drag than if the flow separated. Since the numerical model used to calculate the results cannot accurately predict flow separation or the flow behaviour inside the separation zone, the higher under-turning moment observed on the rectangular block is not reproduced in the numerical results. This discrepancy in the pressure distributions is a plausible cause for the discrepancy in the stability results shown in figure 7.3. That is, the calculated results under predict the reduction of pressure at the leading edge of a block, which results in an overestimate of the block's stability. Recall that for smaller thickness to depth ratios, the calculated results tend to overestimate the block stability but for larger ratios the results agree well with the observed data. As the block thickness to depth ratio increases, so does the reduction in the cross-section of the flow. The resulting pressure distribution is dominated by flow acceleration due to the reduction in cross-section of the flow, rather than the hydraulics at the leading edge. This could explain why the overestimate in block stability is more pronounced for smaller thickness to depth ratios.

Present Study



Dow Ambtman et al. (2011a)

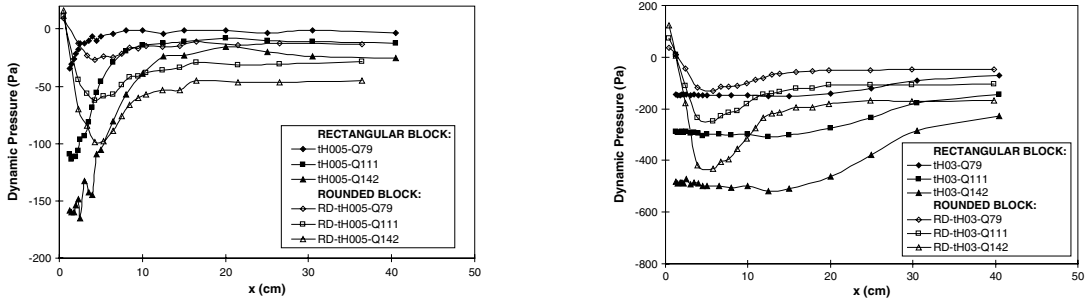


Figure 7.5 – Dynamic pressure on a partially submerged stationary block: computational results. The results in the present study are compared with experimental data from Dow Ambtman et al. (2011a) for a rectangular block with a sharp leading edge and a block with a rounded leading edge. Note the computational results in the present study simulated a rectangular block with a sharp leading edge.

7.3 Ice accumulation at an obstruction

Ice jamming can cause an increase in the forces exerted on hydraulic structures and an increase in water level. Estimating these forces and water levels is of great interest to engineers. In this simulation, sphere-shaped solids accumulate at an obstruction of narrowly spaced piers in an open-channel.

The three-dimensional computational domain contains 600 solids located upstream of 7 vertically oriented cylindrical piles spanning a straight rectangular channel. The solids have a density $\rho_i = 920 \text{ kg/m}^3$ and they float partially submerged in water with a flow depth of 2 m and a velocity of 1 m/s . The geometry of the system is shown in figure 7.6 and the relevant simulation parameters are summarized in table 7.3.

Table 7.3 – Ice accumulation at an obstruction: simulation parameters. The variables are indicated on the numerical setup in figure 7.6.

V	H	L	W	D_i	D_c	S	ϵ	ϕ	k_n	Particles
1 m/s	2 m	15 m	5 m	0.2 m	0.24 m	0.71 m	0.8	45°	10^5 N/m	$300,000$

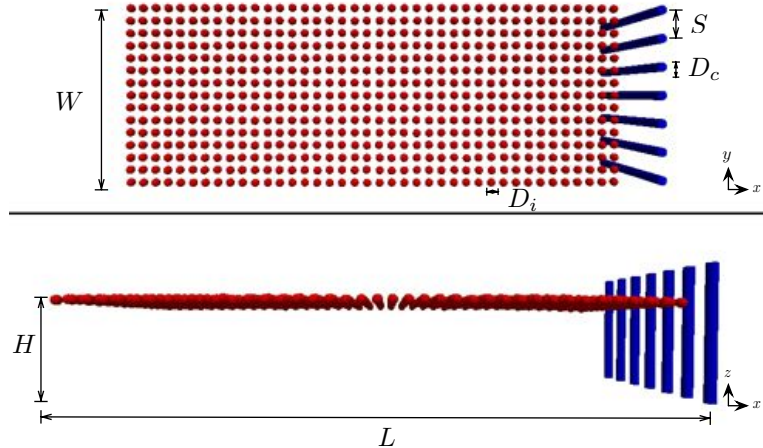


Figure 7.6 – Ice accumulation at an obstruction: numerical setup.

The computational results cannot be easily compared to analytical solutions. Nevertheless, there has been some quantitative evaluation of ice jamming processes earlier in this chapter, in sections 7.1 and 7.2. The results in this section will be assessed qualitatively based on the discussions on granular flow and ice jam initiation in sections 2.2 and 2.3. Since the solids are arranged in a single layer with a small space between each one, they are expected to initially travel at about the same speed as the water surface. As they float downstream, the solids near the channel walls are expected to slow down due to friction. As these solids decelerate, they will likely experience glancing collisions with faster moving solids farther from the wall, causing

further deceleration in subsequent layers. Given enough time, the effects of the bank resistance may be “felt” all the way to the centreline of the channel. Under the right flow conditions and solid concentrations, the solids may form a contiguous layer and form a jam.

In this simulation, the intent of the narrowly spaced piers is to facilitate jam formation. In fact, this technique has been used for constructing ice control structures (ICSs). The purpose of an ICS is to encourage an ice jam to form at a specific location, generally upstream of a community that is at risk of ice jam flooding. Key parameters in their design include the pier diameter and pier spacing, as well as the maximum loads exerted on the piers. Numerical simulations in the early design cycle may assist engineers in coming up with these parameters. In this simulation, it is expected that the piers will lead to enhanced congestion on their upstream side, in a first attempt to model jamming conditions. The jam will increase the resistance to the flow causing the flow to back up and increase the water level.

Figure 7.7 shows a time series of the simulation, in plan and in profile. The water has been removed while post-processing the computational results to better view the ice floes. It should be highlighted that the numerical simulation did in fact contain water and the three-dimensional flow field and fluid-solid interactions were calculated in an identical way to the simulations shown previously.

As expected, the bank resistance slows the solids near the walls first. They, in turn, decelerate the faster moving solids farther from the wall. As the process continues, it is apparent that the fastest moving solids are near the centreline of the channel. The bank resistance and subsequent collisions between solids cause the surface layer to resist the flow somewhat. Consequently, the flow backs up and the water level rises slightly as shown in figure 7.7 (b) and (c). However, the solids do not form a jam and the piers do little to facilitate congestion. With lower water velocities or smaller pile spacing, jam initiation may occur.

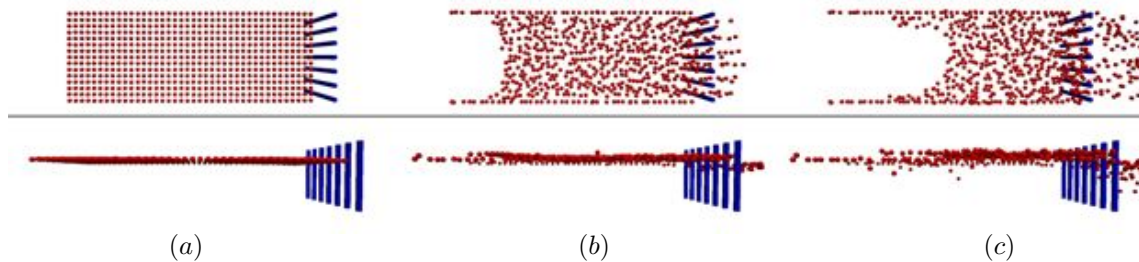


Figure 7.7 – Ice accumulation at an obstruction. Time series showing the movement of the ice floes at (a) 0 s, (b) 5 s, and (c) 10 s.

7.4 Summary

This chapter presented three numerical simulations related to ice jam processes. The first examined the stability of a floating block approaching a stationary cover. The dynamic pressures on all the faces of the block were considered. Effects such as rotational inertia and fluid added mass are all accounted for given that the full unsteady two-dimensional flow field is solved. When compared to theory and experiments, the computational results show fair agreement. The second simulation involved the calculation of the dynamic pressure under a stationary partially submerged block. As expected, the pressure distribution was non-uniform. When compared to laboratory experiments, the computational results differed somewhat. This is not surprising because the numerical model used cannot reproduce viscous effects that are important near solid boundaries. Nevertheless, the overall shape of the pressure distribution in the present study is qualitatively similar to, and quantitatively in the same range as, the experimental data. In the final simulation, ice floes were simulated in a straight channel containing narrowly spaced piers. The intention was to simulate jam initiation upstream of the piers, but no full stationary jam was observed. The computational results, however, show several characteristics common to the early stages of jam initiation, as described in section 2.3. With different simulation parameters, it is expected that jam initiation could be simulated using the numerical model implemented in this thesis. While the results in this section require further refinement, they show the potential for this numerical model to be a useful tool in simulating certain river ice dynamics processes.

Chapter 8

Conclusions and future work

This thesis explored the application of SPH to river ice flows. New developments were implemented in an existing SPH code to tailor it to the engineering problem under consideration - modelling river ice processes. The study involved two main steps. The first was to enable the simulation of freely moving solid objects in a free-surface flow subject to hydraulic and solid contact forces. The second step was to apply these new capabilities to river ice dynamics problems.

As a result of this thesis work, freely moving solid objects in a free-surface flow have been simulated. Both hard-sphere and soft-sphere discrete element models are available to treat solid interactions with other solids and boundaries. The hard-sphere model allows for instantaneous, inelastic collisions between arbitrarily shaped objects and is suitable for low concentrations of solids that do not stay in contact for extended periods. The soft-sphere model is more suitable for solids at high concentrations where they stay in contact for extended durations and develop contact force networks between large groups of solids. The soft-sphere approach can accommodate solids shaped as spheres and three-dimensional circular discs of finite thickness.

The computational results showing the simulation of freely moving solids have been compared to analytical solutions, laboratory experiments, and other numerical simulations. The hard-sphere model was evaluated by simulating the central collision of two spheres as well as a sphere dropping onto a level surface. The computational results were in good agreement with analytical solutions based on the principle of impulse. The soft-sphere model was examined by simulating the collapse of a granular column onto a horizontal plane. The purpose of the simulation was to observe the range of granular flow regimes, from rapidly flowing to static, and to determine, once the flow comes to rest and forms a pile, if the force network between particles accurately transmits the bulk weight of the pile to the horizontal plane. The two-dimensional computational results show some of the same key characteristics of a granular collapse as described in literature (see section 4.7) and the bulk weight of the granular material is accurately calculated for a pile in static equilibrium through a network of contact forces exerted onto a horizontal plane. Many additional simulations would need to be carried out to determine how well the numerical model matches the scaling laws for a granular collapse, relating the initial aspect ratio of the column to the run-out distance and the height of the final deposit. The three-dimensional computational results of a granular collapse show similar behaviour to that in the two-dimensional cases.

After the hard- and soft-sphere models were evaluated without the presence of a fluid phase, a fluid was introduced to evaluate the motion of the solids due to interactions with both the fluid and other solids. To evaluate the hydrodynamic forces exerted on a solid by the fluid, a triangular wedge was simulated falling into calm water. The vertical hydrodynamic force time history calculated on the wedge matched closely to an approximate analytical solution, laboratory experiments, and other computational results. The effects of buoyancy were examined by simulating solids with different densities falling into calm water. The computational results agree well with Archimedes' principle. To evaluate the combined effect of hydrodynamic forces and contact forces on multiple solids, nine three-dimensional solids with six degrees of freedom were driven through a stepped-channel by the forces from a stream of water. While this simulation cannot be easily compared to analytical solutions, the motion of the solids in the channel was believable and the computational results showed that the new developments can model complicated free-surface flows containing multiple solids.

The computational results showing freely moving solid objects are generally encouraging; however, additional rigorous validation of the new developments is recommended. This is especially true for the soft-sphere discrete element model. Considering the end goal to model river ice flows and the time constraints of a master's thesis, several of the results at this stage were examined qualitatively. These results (chapter 6), however, are promising and they could be applied to many interesting engineering problems including debris flows, rockfalls into lakes or rivers, and floating breakwaters, to name a few.

A few simple numerical simulations of ice jam dynamics problems were carried out. The hard-sphere model was used to simulate the stability of a floating block approaching a stationary cover. Since the stability depends on the block's shape, the hard-sphere model is more suited than the soft-sphere model for this application. The soft-sphere model was used to simulate the accumulation of ice upstream of an obstruction composed of narrowly spaced piers. In addition to the flow conditions and the pier spacing, the accumulation of ice depends on the frictional forces exerted between ice fragments in contact with other ice fragments and with the channel walls. Furthermore, it was desired to calculate the force exerted on the piers by the ice fragments. These characteristics make the soft-sphere model more appropriate for this application. Therefore, both the hard- and soft-sphere models have applicability for river ice applications.

The test cases were chosen where dynamic pressures in the free-surface flow might

play an important role. These features cannot be captured using more conventional depth averaged methods such as the shallow water equations. The computational results are promising when compared to approximate analytical solutions and laboratory data on floating block stability. They do, however, show some stark differences with laboratory data measuring dynamic pressures on the underside of a partially submerged block. It was hoped to simulate jam initiation upstream of narrowly spaced piers. While the resulting simulation did not show jam initiation causing a complete stationary jam, it did exhibit several key characteristics common to the early stages of jam initiation. For example, the bank resistance slowed the solids near the walls first, and then caused subsequent layers of solids farther from the wall to be decelerated by glancing collisions. Also, the slower moving surface layer resisted the flow underneath it, which caused the water level to rise. Finally, several solids located near the leading edge of the surface layer submerged and increased its thickness and internal strength. A different set of simulation parameters could have resulted in observing a full stationary jam. The forces exerted by the ice floes and the water were calculated on each pier. Since there was no unified stationary group of ice floes pushing on the piers for extended periods of time, the contact forces calculated on the piers consisted more of short collisions as many of the ice floes made their way past these piers.

The computational results presented in chapter 7 show that SPH has the potential to model certain river ice dynamics problems. The methods used in this thesis are suited to small-scale river ice processes where the dynamic effects may not be captured in traditional depth averaged methods. These simple numerical simulations were largely exploratory efforts to see which river ice phenomena were suited for this numerical method. Consequently, this leaves considerable room for improvement and many future directions that could be taken.

Future directions

Dilated discs - Section 6.2.4 presents preliminary results of a DEM simulation where the solids are shaped as three-dimensional dilated circular discs. Since ice floes generally have high length to thickness ratios, this shape is much more realistic than using spheres. Further improvement is required to the collision detection scheme that was implemented. Without too much more work, a simulation such as the one presented in section 7.3 could model the ice with dilated circular discs rather than spheres.

GPU implementation – Prior to the new developments made as part of this thesis work, the existing SPH code had the capability of calculating on graphical processing units (GPUs). While the new developments work on parallel CPUs, they

have not been modified to enable the use of GPUs. GPU computing is a new field where computationally demanding processes in an application can be offloaded onto a GPU whose architecture permits it to do certain types of computations much faster than a CPU. This improvement would permit significantly faster computation times and make it feasible to simulate problems with larger computational domains.

Turbulence model – Many SPH models have evolved absent of turbulence closures. It is only until fairly recently that a decent amount of literature has surfaced presenting turbulence modelling in SPH (Violeau and Issa, 2007). The SPH model used to calculate the results in this thesis does not contain a turbulence model. Like the grand majority of natural flows, the flows considered in thesis are turbulent. With an increasing amount of research on turbulence modelling and SPH, it may be a natural future direction to develop a turbulence model.

Drag calculation - The boundary treatment presented in section 3.9 and used for the computational results in this thesis has been shown to be an accurate and effective way to calculate hydrodynamic forces on a solid boundary such as a jet on a flat plate or a wedge entering calm water. The force calculation includes both dynamic and hydrostatic pressures and can treat unsteady flow and considers effects such as added mass. The treatment, however, does not consider the drag on a solid boundary due to viscous effects. Since the adopted mathematical model is the Euler equations for an inviscid fluid, it is not surprising that drag is not implicitly accounted for. One way to remediate this shortcoming, is to implement a wall function where the surface elements on the boundary are no longer considered exactly at the surface of the solid, but instead they are assumed to be a small distance away from the surface in the log-layer. Different wall treatments implemented in SPH are described in Issa (2004) and Ferrand et al. (2012).

Hybrid model - Most river ice models use depth-averaged methods, which require a much lower computational demand than solving the fully three-dimensional flow field. Making these simplifying assumptions enables the simulation of much larger computational domains. Depth-averaged methods, however, cannot capture some of the smaller scale dynamics that occur in certain areas along a river. Several SPH hybrid methods have been developed to model large areas without prohibitively long computation times. Most of the computational domain uses a model such as the shallow water equations or Boussinesq approximation and specific areas of interest use SPH solving the Euler equations or the Navier-Stokes equations (Narayanaswamy et al., 2010; Hilton and Cleary, 2012). This type of hybrid model may prove useful in river ice flow applications.

References

- Anderson, J. and Wendt, J. (1995). *Computational fluid dynamics*. McGraw-Hill.
- Ashton, G. (1974). Froude criterion for ice-block stability. *Journal of Glaciology*, 3(68):974.
- Babic, M., Shen, H., and Bjedov, G. (1990). Discrete element simulations of river ice transport. In *IAHR 10th International Symposium on Ice*, Espoo, Finland.
- Balmforth, N. and Kerswell, R. (2005). Granular collapse in two dimensions. *Journal of Fluid Mechanics*, 538(1):399–428.
- Baraff, D. (2001). Physically based modeling: Rigid body simulation. *SIGGRAPH Course Notes, ACM SIGGRAPH*.
- Barker, G. (1994). Computer simulations of granular materials. In Mehta, A., editor, *Granular Matter: an interdisciplinary approach*. Springer.
- Batchelor, G. (1967). *An introduction to fluid dynamics*. Cambridge University Press.
- Batchelor, G. (1974). Transport properties of two-phase materials with random structure. *Annual Review of Fluid Mechanics*, 6(1):227–255.
- Beltaos, S. (1983). River ice jams - theory, case studies, and applications. *Journal of Hydraulic Engineering*, 109(10):1338–1359.
- Beltaos, S. (1993). Numerical computation of river ice jams. *Canadian Journal of Civil Engineering*, 20(1):88–99.
- Beltaos, S. (1995). *River ice jams*. Water Resources Publication.
- Beltaos, S. (2007). River ice breakup processes: recent advances and future directions. *Canadian Journal of Civil Engineering*, 34(6):703–716.
- Beltaos, S. (2008). Progress in the study and management of river ice jams. *Cold Regions Science and Technology*, 51(1):2–19.
- Beltaos, S. and Krishnappan, B. (1982). Surges from ice jam releases: a case study. *Canadian Journal of Civil Engineering*, 9(2):276–284.
- Ben Moussa, B. and Vila, J. (2000). Convergence of SPH method for scalar nonlinear conservation laws. *SIAM Journal on Numerical Analysis*, pages 863–887.
- Benz, W. (1990). Smooth particle hydrodynamics - a review. In Buchler, J. R., editor, *Numerical Modelling of Nonlinear Stellar Pulsations: Problems and Prospects*, pages 269–288, Les Arcs, France. Kluwer Academic Publ.

- Benz, W., Slattery, W. L., and Cameron, A. G. W. (1986). The origin of the moon and the single-impact hypothesis 1. *Icarus*, 66(3):515–535.
- Bicanic, N. (2004). Discrete element methods. In Stein, E., de Borst, R., and Hughes, T., editors, *Encyclopedia of computational mechanics*. Wiley.
- Bonet, J. and Lok, T. (1999). Variational and momentum preservation aspects of smooth particle hydrodynamic formulations. *Computer Methods in Applied Mechanics and Engineering*, 180(1):97–115.
- Campbell, C. (1990). Rapid granular flows. *Annual Review of Fluid Mechanics*, 22(1):57–90.
- Capone, T., Panizzo, A., Cecioni, C., and Dalrymple, R. (2007). Accuracy and stability of numerical schemes in SPH. In *2nd International SPHERIC Workshop*, Madrid, Spain.
- Carson, R., Beltaos, S., Groeneveld, J., Healy, D., She, Y., Malenchak, J., Morris, M., Saucet, J.-P., Kolarski, T., and Shen, H. T. (2011). Comparative testing of numerical models of river ice jams. *Canadian Journal of Civil Engineering*, 38(6):669–678.
- Cleary, P., Prakash, M., Ha, J., and Stokes, N. (2007). Smooth particle hydrodynamics: status and future potential. *Progress in Computational Fluid Dynamics, an International Journal*, 7(2):70–90.
- Colagrossi, A. and Landrini, M. (2003). Numerical simulation of interfacial flows by smoothed particle hydrodynamics. *Journal of Computational Physics*, 191(2):448–475.
- Coutermarsh, B. and McGilvary, W. (1993). Static analysis of floating ice block stability. *Journal of Hydraulic Research*, 31(2):147–160.
- Cummins, S. J. and Rudman, M. (1999). An SPH projection method. *Journal of Computational Physics*, 152(2):584–607.
- Cundall, P. and Strack, O. (1979). A discrete numerical model for granular assemblies. *Geotechnique*, 29(1):47–65.
- Dalrymple, R. and Rogers, B. (2006). Numerical modeling of water waves with the SPH method. *Coastal engineering*, 53(2):141–147.
- Daly, S. and Axelson, K. (1990). Stability of floating and submerged blocks. *Journal of Hydraulic Research*, 28(6):737–752.
- Daly, S. and Hopkins, M. (2001). Estimating forces on an ice control structure using dem. In *Proceedings, 11th Workshop on River Ice. River ice processes within a changing environment*, pages 14–16.
- Dam, E., Koch, M., and Lillholm, M. (1998). Quaternions, interpolation and animation. Technical report, Department of Computer Science, University of Copenhagen.

- Dobrovolskaya, Z. (1969). On some problems of similarity flow of fluid with a free surface. *Journal of Fluid Mechanics*, 36(04):805–829.
- Donea, J., Huerta, A., and Ponthot, J. (2004). Arbitrary lagrangian-eulerian methods. *Encyclopedia of computational mechanics*.
- Dow Ambtman, K., Hicks, F., and Steffler, P. (2011a). Experimental investigation of the pressure distribution beneath a floating ice block. *Journal of Hydraulic Engineering*, 137(4):399–411.
- Dow Ambtman, K., Steffler, P., and Hicks, F. (2011b). Analysis of the stability of floating ice blocks. *Journal of Hydraulic Engineering*, 137(4):412–422.
- Dubois, F. (2001). Partial riemann problem, boundary conditions, and gas dynamics. In Tourrette, L. and Halpern, L., editors, *Absorbing Boundaries and Layers, Domain Decomposition Methods: Applications to Large Scale Computers*. Nova Science Pub Incorporated.
- Ettema, R. (1990). Jam initiation in unobstructed channels - laboratory observations. *Journal of Hydraulic Research*, 28(6):673–684.
- Fang, J., Parriaux, A., Rentschler, M., and Ancey, C. (2009). Improved SPH methods for simulating free surface flows of viscous fluids. *Applied Numerical Mathematics*, 59(2):251–271.
- Ferrand, M., Laurence, D., Rogers, B., Violeau, D., and Kassiotis, C. (2012). Unified semi-analytical wall boundary conditions for inviscid, laminar or turbulent flows in the meshless SPH method. *International Journal for numerical methods in fluids*.
- Ferrari, A. (2010). SPH simulation of free surface flow over a sharp-crested weir. *Advances in Water Resources*, 33(3):270–276. Ferrari, Angela.
- Flato, G. and Gerard, R. (1986). Calculation of ice jam profiles. In *4th Workshop on River Ice*, pages Paper C–3, Montreal, Canada.
- Gingold, R. and Monaghan, J. (1977). Smoothed particle hydrodynamics-theory and application to non-spherical stars. *Monthly Notices of the Royal Astronomical Society*, 181:375–389.
- Gingold, R. A. and Monaghan, J. J. (1978). Binary fission in damped rotating polytropes. *Monthly Notices of the Royal Astronomical Society*, 184(2):481–499.
- Godunov, S. (1959). A difference method for numerical calculation of discontinuous solutions of the equations of hydrodynamics. *Matematicheskii Sbornik*, 89(3):271–306.
- Goldhirsch, I. (2003). Rapid granular flows. *Annual Review of Fluid Mechanics*, 35(1):267–293.

- Guilcher, P., Ducrozet, G., Alessandrini, B., and Ferrant, P. (2007). Water wave propagation using SPH models. In *2nd International SPHERIC Workshop*, Madrid, Spain.
- Gutfraind, R. and Savage, S. B. (1997). Smoothed particle hydrodynamics for the simulation of broken-ice fields: Mohr-coulomb-type rheology and frictional boundary conditions. *Journal of Computational Physics*, 134(2):203–215.
- Gutfraind, R. and Savage, S. B. (1998). Flow of fractured ice through wedge-shaped channels: smoothed particle hydrodynamics and discrete-element simulations. *Mechanics of Materials*, 29(1):1–17.
- Henderson, F. and Gerard, R. (1981). Flood waves caused by ice jam formation and failure. In *In Proceedings of the IAHR Symposium on Ice*, volume 1, pages 277–287, Québec City, Que.
- Hernquist, L. and Katz, N. (1989). Treesph - a unification of SPH with the hierarchical tree method. *The Astrophysical Journal Supplement Series*, 70:419–446.
- Hibler, W. (1979). A dynamic thermodynamic sea ice model. *Journal of Physical Oceanography*, 9:815–846.
- Hilton, J. and Cleary, P. (2012). A multiscale method for geophysical flow events. *International Journal for Multiscale Computational Engineering*, 10(4):375–390.
- Hopkins, M. and Daly, S. (2003). Recent advances in discrete element modeling of river ice. In *Proc., 12th Workshop on the Hydraulics of Ice Covered Rivers*. Canadian Geophysical Union in Calgary Alberta, Canada.
- Hopkins, M., Daly, S., and Lever, J. (1996). Three-dimensional simulation of river ice jams. In *International Specialty Conference on Cold Regions Engineering*, Fairbanks, AK.
- Hopkins, M., Hibler III, W., and Flato, G. (1991). On the numerical simulation of the sea ice ridging process. *Journal of geophysical research*, 96(C3):4809–4820.
- Hopkins, M. and Tuhkuri, J. (1999). Compression of floating ice fields. *Journal of geophysical research*, 104(C7):15815–15,825.
- Hopkins, M. and Tuthill, A. (2002). Ice boom simulations and experiments. *Journal of cold regions engineering*, 16(3):138–155.
- Hu, X. and Adams, N. (2007). An incompressible multi-phase SPH method. *Journal of Computational Physics*, 227(1):264–278.
- Issa, N. (2004). *Numerical assessment of the SPH gridless method for incompressible flows and its extension to turbulent flow*. PhD thesis, Institute of Science and Technology, University of Manchester.

- Jasek, M. (2003). Ice jam release and break-up front propagation. In *Proc. 12th Workshop on the Hydraulics of Ice Covered Rivers*, pages 348–368. CGU HS Committee on River Ice Processes and the Environment Edmonton, AB, Canada.
- Kennedy, R. (1958). Forces involved in pulpwood holding grounds - i. tranverse holding grounds with piers. *The Engineering Journal, Engineering Institute of Canada*, 41:58–68.
- Lajeunesse, E., Mangeney-Castelnau, A., and Vilotte, J. (2004). Spreading of a granular mass on a horizontal plane. *Physics of Fluids*, 16(7):2371–2381.
- Larrieu, E., Staron, L., and Hinch, E. (2006). Raining into shallow water as a description of the collapse of a column of grains. *Journal of Fluid Mechanics*, 554:259–270.
- Larsen, P. (1975). Notes on the stability of floating ice blocks. In *Proceedings of the IAHR third international symposium on ice problems. Hanover, NH, IAHR*, pages 305–313.
- Leboeuf, F. and Marongiu, J. C. (2011). Application of SPH methods to conservative equations. In Magoules, F., editor, *Computational fluid dynamics*. Chapman and Hall.
- Lee, B. H., Park, J. C., Kim, M. H., Jung, S. J., Ryu, M. C., and Kim, Y. S. (2010). Numerical simulation of impact loads using a particle method. *Ocean Engineering*, 37(2-3):164–173.
- LeVeque, R. (1992). *Numerical methods for conservation laws*. Birkhauser-Verlag.
- Libersky, L. D. and Petschek, A. (1991). Smoothed particle hydrodynamics with strength of materials. In Trease, H., Fritts, M., and Crowley, W., editors, *Advances in the Free-Lagrange method, proceedings of the Next Free-Lagrange Conference*, volume 395, pages 248–257. Springer Verlag.
- Liu, G. and Liu, M. (2003). *Smoothed particle hydrodynamics: a meshfree particle method*. World Scientific Publishing Company Incorporated.
- Liu, L., Li, H., and Shen, H. (2006). A two-dimensional comprehensive river ice model. In *Proceedings of the 18th IAHR Symposium on River Ice, Sapporo, Japan*.
- Liu, M. and Liu, G. (2010). Smoothed particle hydrodynamics (SPH): an overview and recent developments. *Archives of computational methods in engineering*, 17(1):25–76.
- Lopez, D., Marivela, R., and Garrote, L. (2010). Smoothed particle hydrodynamics model applied to hydraulic structures: A hydraulic jump test case. *Journal of Hydraulic Research*, 48(1 Extra Issue):142–158.
- Loset, S. (1994). Discrete element modelling of a broken ice field–part i: model development. *Cold Regions Science and Technology*, 22(4):339–347.

- Lube, G., Huppert, H., Sparks, R., and Freundt, A. (2005). Collapses of two-dimensional granular columns. *Physical Review E*, 72(4):041301.
- Lube, G., Huppert, H., Sparks, R., and Hallworth, M. (2004). Axisymmetric collapses of granular columns. *Journal of Fluid Mechanics*, 508(1):175–199.
- Lucy, L. B. (1977). Numerical approach to testing of fission hypothesis. *The Astronomical Journal*, 82(12):1013–1024.
- Luding, S. (1998). Collisions and contacts between two particles. In Herrmann, H., Hovi, J., and Luding, S., editors, *Physics of dry granular media*. Kluwer academic publishers.
- Macia, F., Colagrossi, A., Antuono, M., and Souto-Iglesias, A. (2011). Benefits of using a wendland kernel for free-surface flows. In *6th International SPHERIC workshop*, pages 30–37, Hamburg, Germany.
- Marcotte, N. (1984). Anchor ice in lachine rapids, results of observations and analysis. In *Proceedings of the IAHR International Symposium on Ice*, volume 1, pages 151–159, Hamburg, Germany.
- Marongiu, J. C. (2007). *Méthode numérique lagragienne pour la simulation d'écoulements à surface libre - Applications aux turbines Pelton*. PhD thesis, École Centrale de Lyon.
- Marongiu, J. C., Leboeuf, F., Caro, J., and Parkinson, E. (2010). Free surface flows simulations in pelton turbines using an hybrid SPH-ALE method. *Journal of Hydraulic Research*, 48(1 Extra Issue):40–49.
- Masella, J., Faille, I., and Gallouet, T. (1999). On an approximate godunov scheme. *International Journal of Computational Fluid Dynamics*, 12:133–149.
- Monaghan, J. (1992). Smoothed particle hydrodynamics. *Annu. Rev. Astron. Astrophys.*, 30:543–74.
- Monaghan, J. (1994). Simulating free surface flows with SPH. *Journal of Computational Physics*, 110:399–406.
- Monaghan, J. (2000). SPH without a tensile instability. *Journal of Computational Physics*, 159(2):290–311.
- Monaghan, J. (2005). Smoothed particle hydrodynamics. *Reports on Progress in Physics*, 68:1703.
- Monaghan, J. (2012). Smoothed particle hydrodynamics and its diverse applications. *Annual Review of Fluid Mechanics*, 44:323–346.
- Monaghan, J., Cas, R., Kos, A., and Hallworth, M. (1999). Gravity currents descending a ramp in a stratified tank. *Journal of Fluid Mechanics*, 379(1):39–69.

- Monaghan, J. and Gingold, R. (1983). Shock simulation by the particle method SPH. *Journal of Computational Physics*, 52(2):374–389.
- Monaghan, J. J., Kos, A., and Issa, N. (2003). Fluid motion generated by impact. *Journal of Waterway Port Coastal and Ocean Engineering*, 129(6):250–259.
- Morris, J. P., Fox, P. J., and Zhu, Y. (1997). Modeling low reynolds number incompressible flows using SPH. *Journal of Computational Physics*, 136(1):214–226.
- Narayanaswamy, M., Crespo, A. J. C., Gomez-Gesteira, M., and Dalrymple, R. A. (2010). SPHysics-FUNWAVE hybrid model for coastal wave propagation. *Journal of Hydraulic Research*, 48(1 Extra Issue):85–93.
- Ng, T. and Lin, X. (1995). Short communication contact detection algorithms for three dimensional ellipsoids in discrete element modelling. *International Journal for Numerical and Analytical Methods in Geomechanics*, 19:653–659.
- Nolin, S., Roubtsova, V., Morse, B., and Quach, T. (2009). Smoothed particle hydrodynamics hybrid model of ice-jam formation and release. *Canadian Journal of Civil Engineering*, 36(7):1133–1143.
- Oger, G., Doring, M., Alessandrini, B., and Ferrant, P. (2006). Two-dimensional SPH simulations of wedge water entries. *Journal of Computational Physics*, 213(2):803–822.
- Oger, G., Doring, M., Alessandrini, B., and Ferrant, P. (2007). An improved SPH method: Towards higher order convergence. *Journal of Computational Physics*, 225(2):1472–1492.
- O’Sullivan, C. (2011). *Particulate discrete element modelling: a geomechanics perspective*. Taylor and Francis.
- Pariset, E. and Hausser, R. (1961). Formation and evolution of ice covers on rivers. *Transactions, Engineering Institute of Canada*, 5(1):41–49.
- Pariset, E., Hausser, R., and Gagnon, A. (1966). Formation of ice covers and ice jams in rivers. *Journal of the Hydraulics Division*, 92(6):1–24.
- Randles, P. W. and Libersky, L. D. (1996). Smoothed particle hydrodynamics: Some recent improvements and applications. *Computer Methods in Applied Mechanics and Engineering*, 139(1-4):375–408.
- Robinson, M. (2009). *Turbulence and Viscous Mixing using Smoothed Particle Hydrodynamics*. PhD thesis, Monash University.
- Rogers, B. D., Dalrymple, R. A., and Stansby, P. K. (2010). Simulation of caisson breakwater movement using 2-d SPH. *Journal of Hydraulic Research*, 48(1 Extra Issue):135–141.

- Savage, S. (1984). The mechanics of rapid granular flows. *Advances in applied mechanics*, 24:289–366.
- Sayed, M. (1981). *Theoretical and Experimental studies of the flow of cohesionless granular materials*. PhD thesis, McGill University.
- Sayed, M. and Morse, B. (1999). Numerical simulation of ice clearing and jam initiation in navigation channels. In *River Ice Management with a Changing Climate: Dealing with Extreme Events, Proceedings of the 10th Workshop on River Ice, Winnipeg, Man*, pages 8–11.
- Schafer, J., Dippel, S., and Wolf, D. (1996). Force schemes in simulations of granular materials. *Journal de physique I*, 6(1):5–20.
- Schoenberg, I. (1946). Contributions to the problem of approximation of equidistant data by analytic functions. *Quart. Appl. Math.*, 4(2):45–99.
- Shao, S., Ji, C., Graham, D., Reeve, D., James, P., and Chadwick, A. (2006). Simulation of wave overtopping by an incompressible SPH model. *Coastal engineering*, 53(9):723–735.
- Shao, S. and Lo, E. (2003). Incompressible SPH method for simulating newtonian and non-newtonian flows with a free surface. *Advances in Water Resources*, 26(7):787–800.
- Shen, H. (2002). Development of a comprehensive river ice simulation system. In *Proceedings of the 16th international symposium on ice*, pages 142–148.
- Shen, H., Chen, Y., Wake, A., and Crissman, R. (1993). Lagrangian discrete parcel simulation of river ice dynamics. *International Journal of Offshore and Polar Engineering*, 3(4).
- Shen, H. T. (2010). Mathematical modeling of river ice processes. *Cold Regions Science and Technology*, 62(1):3–13.
- Shen, H. T., Lu, S., and Crissman, R. D. (1997). Numerical simulation of ice transport over the lake erie niagara river ice boom. *Cold Regions Science and Technology*, 26(1):17–33.
- Shen, H. T., Shen, H., and Tsai, S. M. (1990). Dynamic transport of river ice. *Journal of Hydraulic Research*, 28(6):659–671.
- Shen, H. T., Su, J. S., and Liu, L. W. (2000). SPH simulation of river ice dynamics. *Journal of Computational Physics*, 165(2):752–770.
- Springel, V. (2010). Smoothed particle hydrodynamics in astrophysics. *Annual Review of Astronomy and Astrophysics*, 48:391–430.
- Staron, L. and Hinch, E. (2005). Study of the collapse of granular columns using two-dimensional discrete-grain simulation. *Journal of Fluid Mechanics*, 545(1):1–27.

- Stockstill, R. L., Daly, S. F., and Hopkins, M. A. (2009). Modeling floating objects at river structures. *Journal of Hydraulic Engineering*, 135(5):403–414.
- Sun, S. and Shen, H. (2012). Simulation of pancake ice load on a circular cylinder in a wave and current field. *Cold Regions Science and Technology*.
- Swegle, J., Hicks, D., and Attaway, S. (1995). Smoothed particle hydrodynamics stability analysis. *Journal of Computational Physics*, 116(1):123–134.
- Tartakovsky, A., Pan, W., and Monaghan, J. J. (2012). SPH non-newtonian model for ice sheet and ice shelf dynamics. In *7 th International SPHERIC Workshop*, pages 23–30, Prato, Italy.
- Ting, J., Khwaja, M., Meachum, L., and Rowell, J. (1993). An ellipse-based discrete element model for granular materials. *International Journal for Numerical and Analytical Methods in Geomechanics*, 17(9):603–623.
- Toro, E. (1999). *Riemann solvers and numerical methods for fluid dynamics: a practical introduction*. Springer Verlag.
- Tsai, S. M., Shen, H., and Shen, H. (1988). Dynamic transport of river ice and jam initiation, report no. 88-2. Technical report, Department of Civil and Environmental Engineering, Clarkson University.
- Uzuner, M. and Kennedy, J. (1972). Stability of floating ice blocks. *Journal of the Hydraulics Division*, 98(12):2117–2133.
- Uzuner, M. and Kennedy, J. (1976). Theoretical model of river ice jams. *Journal of the Hydraulics Division*, 102(9):1365–1383.
- Van der Hoef, M., Ye, M., van Sint Annaland, M., Andrews, A., Sundaresan, S., and Kuipers, J. (2006). Multiscale modeling of gas-fluidized beds. *Advances in chemical engineering*, 31:65–149.
- Vila, J. P. (1999). On particle weighted methods and smooth particle hydrodynamics. *Mathematical Models and Methods in Applied Sciences*, 9(2):161–209.
- Violeau, D. (2012). *Fluid Mechanics and the SPH method*. Oxford University Press.
- Violeau, D., Buvat, C., Abed-Meraiem, K., and de Nanteuil, E. (2007a). Numerical modelling of boom and oil spill with SPH. *Coastal Engineering*, 54(12):895–913.
- Violeau, D. and Issa, R. (2007). Numerical modelling of complex turbulent free-surface flows with the SPH method: an overview. *International journal for numerical methods in fluids*, 53(2):277–304.
- Violeau, D., Issa, R., Benhamadouche, S., Saleh, K., Chorda, J., and Maubourguet, M. (2007b). Modelling a fish passage with SPH and eulerian codes: the influence of turbulent closure. In *3rd SPHERIC international workshop, Lausanne*.

- Wagner, H. (1932). Impact and slide occurrence on the surface of liquids. *Zeitschrift Fur Angewandte Mathematik Und Mechanik*, 12:193–215.
- Wake, A. and Rumer Jr, R. (1983). Great lakes ice dynamics simulation. *Journal of Waterway, Port, Coastal, and Ocean Engineering*, 109(1):86–102.
- Walton, O. (1993). Numerical simulation of inelastic, frictional particle-particle interactions. In Roco, M., editor, *Particulate two-phase flow*, pages 884–911. Oxford: Butterworth- Heinemann.
- Wei, G. (2006). Three-dimensional collision modeling for rigid bodies and its coupling with fluid flow computation. Technical report, Flow Science, Inc.
- Wong, J., Beltaos, S., and Krishnappan, B. (1985). Laboratory tests on surges created by ice jam releases. *Canadian Journal of Civil Engineering*, 12(4):930–933.
- Zenit, R. (2005). Computer simulations of the collapse of a granular column. *Physics of Fluids*, 17:031703.
- Zhao, R., Faltinsen, O., and Aarsnes, J. (1997). Water entry of arbitrary two-dimensional sections with and without flow separation. In *21st Symposium on Naval Hydrodynamics*.